TRANSIENTS IN POLYMER ELECTROLYTE MEMBRANE (PEM) FUEL CELLS

Atul Verma

Dissertation submitted to the faculty of the Virginia Polytechnic Institute and State University
in partial fulfillment of the requirements for the degree of

Doctor of Philosophy
In
Mechanical Engineering

Ranga Pitchumani, Chair
Scott W. Case
Michael W. Ellis
Roop L. Mahajan
Danesh K. Tafti

September 24, 2015
Blacksburg, VA, 24061

Keywords: Polymer Electrolyte Fuel Cells, Water Content, Steady State Time, Membrane Hydration, Operating Conditions, Design Windows, Mechanical Behavior; Equivalent Plastic Strain, Load Change; Voltage Reversal, Anode Dryout, Degradation, Dynamic Fractal Model, Deposition, Time Scales, Electrochemical Reactions, Moisture Transport, Reactant Transport

Transients in Polymer Electrolyte Membrane (PEM) Fuel Cells

Atul Verma

Abstract

The need for energy efficient, clean and quiet, energy conversion devices for mobile and stationary applications has presented proton exchange membrane (PEM) fuel cells as a potential energy source. The use of PEM fuel cells for automotive and other transient applications, where there are rapid changes in load, presents a need for better understanding of transient behavior. In particular at low humidity operations; one of the factors critical to the performance and durability of fuel cell systems is water transport in various fuel cell layers, including water absorption in membrane. An essential aspect to optimization of transient behavior of fuel cells is a fundamental understanding of response of fuel cell system to dynamic changes in load and operating parameters. This forms the first objective of the dissertation. An insight in to the time scales associated with various transport phenomena will be discussed in detail. In the second component on the study, the effects of membrane properties on the dynamic behavior of the fuel cells are analyzed with focus on membrane dry-out for low humidity operations. The mechanical behavior of the membrane is directly related to the changes in humidity levels in membrane and is explored as a part third objective of the dissertation. Numerical studies addressing this objective will be presented. Finally, porous media undergoing physical deposition (or erosion) are common in many applications, including electrochemical systems such as fuel cells (for example, electrodes, catalyst layers, etc.) and batteries. The transport properties of these porous media are a function of the deposition and the change in the porous structures with time. A dynamic fractal model is introduced to describe such structures undergoing deposition and, in turn, to evaluate the changes in their physical properties as a function of the deposition.

Acknowledgements

First and foremost, I would like to express the deepest appreciation to my advisor, Dr. Ranga Pitchumani, for presenting me with an opportunity to pursue research in this exciting field. I am extremely thankful for his patient guidance and constant encouragement and necessary force throughout my PhD program. His zest for solving a problem fully, with both basic and applied scientific approaches has been a source of inspiration to me. I would also like to thank my advisory committee, Drs. Roop Mahajan, Danesh Tafti, Scott Case, and Mike Ellis for their recommendation, assistance and guidance.

The express my deepest gratitude to my family for their continuous love and support. I am highly indebted to my mother and sister who tolerated my absence from home in difficult times. My lab mates, and friends are a source of enjoyment and fulfillment, and I cherish their companionship.

Table of Contents

List of Figures

List of Tables

Chapter 1: Introduction

This dissertation explores fundamental understanding of transients of PEM fuel cells, specifically the performance and mechanical behavior (durability) at low humidity conditions. At first we explain the functioning of a PEM fuel cell in brief followed by a description of challenges to be addressed in subsequent chapters.

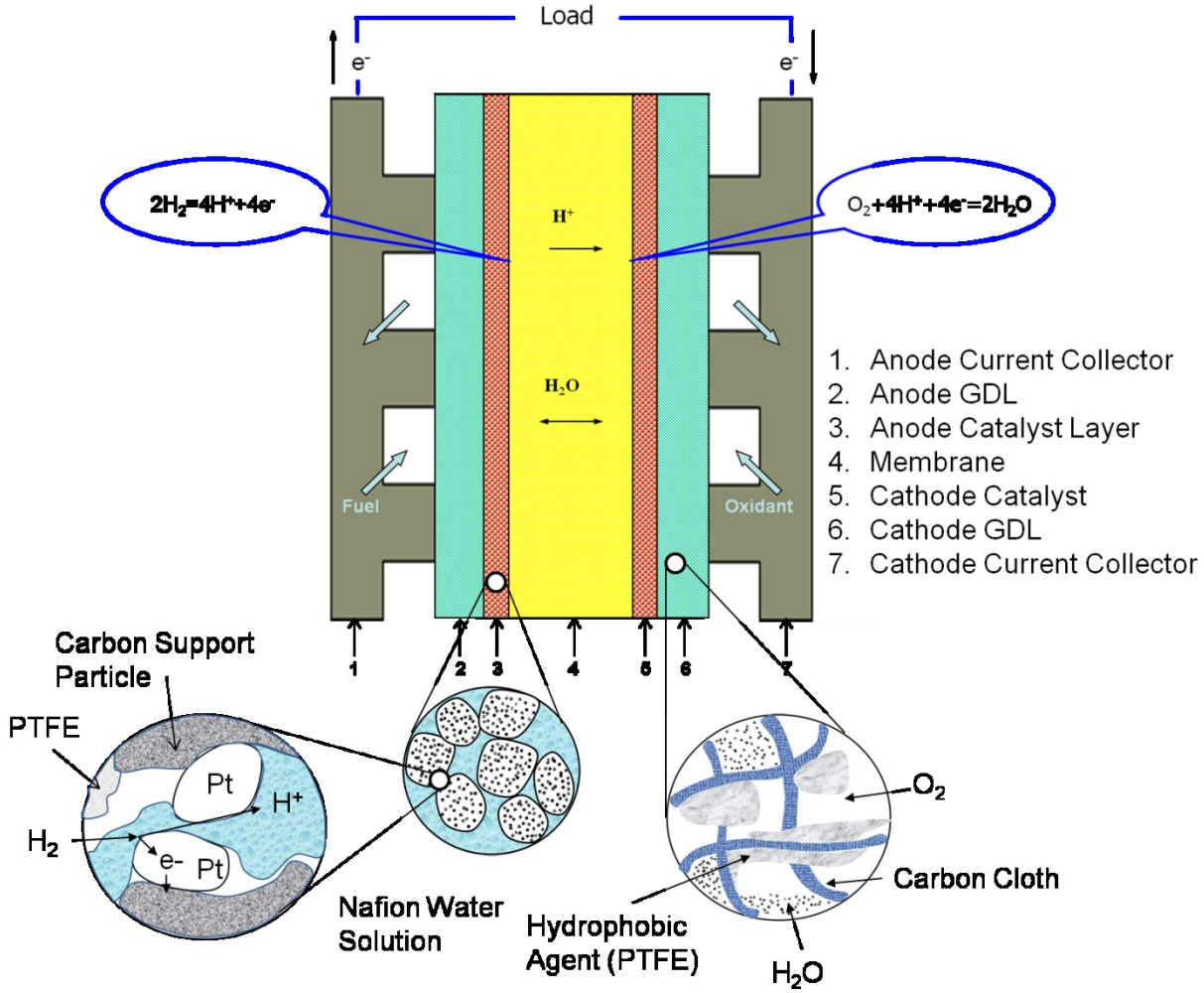

Figure 1: Cross-sectional schematic of PEM Fuel Cell

A PEM fuel cell is composed of membrane electrode assembly (MEA), covered by porous gas diffusion layer (GDL) on either side, followed by gas channels which are grooved in serpentine or interdigitated way in to the bipolar plates. Humidified hydrogen (H_2) and oxygen (O_2) or air is transported, through anode and cathode flow channels and diffusion layers respectively, to react at catalyst layers. A membrane, normally made of Nafion (DuPont),

separates the reactant gases and conducts proton. Fuel cell performance is critically related to the membrane hydration as it affects the proton conductivity through membrane, with higher water content (number of water molecules per sulfonic acid group) in the membrane leading to higher conductivity. Too much water can flood electrodes, blocking the reacting sites to the reactant gases, whereas electro-osmotic drag or low humidity operation can cause membrane dryout. Hence water management is critical to fuel cell performance. Under low- humidity operations, suitable for automotive applications, electro-osmotic drag, back-water diffusion and rate of water supply or removal through humidified reactants interact in complex way over different time scales to affect the transient behavior of PEM fuel cells.

Due to major improvements in catalyst loading and membrane technology, PEM fuel cells have seen increased usage in various applications. A further reduction in cost can be achieved through better design, improved performance, and improved durability of the fuel cells. This objective has generated lot of interest for research in control and optimization of transport and electrochemical processes of fuel cells. While most of the research has been focused on steady-state operation, the use of PEM fuel cells for applications with rapid changes in load (e.g. automotive), presents a need for better understanding of transient behavior. The first part, Chapter 2, presents an insight in to the transient operation of PEM fuel cells focusing on the time scales associated with various transport phenomena. A detailed, model-based parametric study is carried out to analyze the effects of operating conditions on the time taken for a single cell system to reach steady state. Based on the studies, design windows are presented that limit the time taken to reach steady state to a desired value. Optimum parameter combinations that minimize the transient time are also identified from the studies. In addition, Chapter 3, the effects of changes in operating parameters on the power density are presented and are optimized with an objective to match the power requirements for US06 drive cycle. The intent is to explore the operation of fuel cells, if they were to run dry that is with minimal auxiliary systems required to humidify the feed streams which might be different from mode of current operation in various applications.

In the second part, Chapter 4, numerical simulations for a single channel PEM fuel cell undergoing changes in load, were carried out by subjecting the unit cell to step change in current were carried out with the goal of understanding the effects of membrane properties on the dynamic behavior. The complex interaction between cell voltage response and water

transport dynamics for various membrane properties is explored in detail, where the performance is critically related to the water content of the membrane. Detailed computational fluid dynamics (CFD) simulations are carried out to show that step increase in current density leads to anode dryout due to electro-osmotic drag, and to investigate the dependence of transient behavior on the variations in membrane properties. The results show that water uptake by the membrane is a crucial factor in determining the occurrence of anode dryout and hence voltage reversal, and can be avoided by improvement in design of membranes studied. In addition the effects of interfacial mass transfer on the fuel cell transients are also presented.

One of the major barriers for polymer electrolyte membrane (PEM) fuel cells to be commercially viable for stationary and transportation applications is the durability of membranes undergoing chemical and mechanical degradation over the period of operation. Toward understanding the effects of operating parameters on membrane durability, the third part (Chapters 5 and 6) of the research presents numerical simulations for a single channel PEM fuel cell undergoing changes in load, by subjecting a unit cell to step changes in voltage. The objective is to elucidate the mechanical response of membrane, which is subjected to hygral (water) loading and unloading cycles at constant temperature. Detailed three-dimensional (3D) computational fluid dynamics (CFD) simulations are conducted, taking in to account the complex interactions of water transport dynamics and load changes, to accurately capture the water content in the membrane with changes in cell voltage. The water content obtained through CFD simulations is, in turn, used to carry out a two-dimensional (2D) finite element (FE) analysis to predict the mechanical response of the membrane undergoing cyclic change in water content, as the operating voltage is cycled. The effects of cyclic changes in cell potential on the stresses induced, amount of plastic strain and its localization are analyzed for various inlet cathode humidity values for two sections along the length of the fuel cell.

The porous layers in fuel cell over the time period of operation is subjected to changes owing to deposition (fouling) and erosion in certain cases. The above processes lead to change in porous structure and needs to be accounted for in the modeling. In this part of work we develop and present a dynamic fractal model to describe the changes in porous structure as a function of saturation. The model is then used to predict the changes in diffusivity for different levels of saturation. *A review on the current state of research and the relevance to the challenges explored is presented in the corresponding chapters.*

Chapter 2: Effects of Operating Parameters on the Transient Response of Proton Exchange Membrane Fuel cells Subject to Load Changes

This chapter presents an insight into the transient operation of PEM fuel cells focusing on the time scales associated with various transport phenomena. A detailed model-based parametric study is conducted to analyze the effects of operating conditions on the time taken by the single cell system to reach steady state. Based on the studies, design windows are presented that limit the time taken to reach steady state to a desired value. Optimum parameter combinations that minimize the transient time are also identified from the studies. In addition the effects of changes in operating parameters on the power density are presented and are optimized with an objective to match the power requirements for US06 drive cycle.

2.1 Introduction

Under low-humidity operations, suitable for automotive applications, electro-osmotic drag, back-water diffusion and rate of water supply or removal through humidified reactants interact in complex ways to affect the transient behavior of PEM fuel cells presenting different time scales. Operating conditions play an important role in determining the membrane water content and thus the time taken for a system to reach steady state for given load changes. For rapid changes, the time taken to reach steady state can be minimized or can be limited to a certain desirable value by designing operating windows.

Several experimental and numerical studies have been carried out in the literature to understand the performance and water management in PEM fuel cells [3-13]. The previous studies mainly dealt with steady state operation. Due to the transient operation of fuel cells in various applications it is critical to study the dynamic behavior. Transient behavior of fuel cells has been studied by several researchers. Amphlett et al. [14] developed a lumped-parameter based thermal model to predict the transient response. Their analytical model was based on unsteady thermal model with steady-state electrochemical process. Pathapati et al. [15] and Xie et al. [16] developed simplified system level models for their transient study. Ceraolo [17] used a simplified one dimensional model to study the dynamic behavior, considering only the cathode side. These models were simplified and lacked detailed representation of complex interactions during transient operations. A detailed two-dimensional computational fluid dynamics (CFD) model by Um et al. [4] studied briefly the transient response for fully hydrated

membrane, thus capturing the transients of gas transport. A more complete model was developed by Wang et al. [18,19], extending the model used in Refs. [4,6,7] to include the effects of water accumulation and electrochemical double layer discharge. The transient model explored the dynamic behavior for step change in humidity and voltage, emphasizing the different time scales characteristic to transport and electrochemical process. Transient 3D simulations were conducted by Shimpalee et al. [20]. The results showed the occurrence of overshoot in current density for a given change in the electrical load. Zou et al. [21] numerically examined the effect of channel width fraction, porosity of the gas diffusion layer, pressure drop and the surface over-potential of the catalyst layer on the dynamic performance by modeling only the cathode side of fuel cell. Peng et al. [22] used 3D single-phase and non-isothermal numerical model to investigate the effect of stoichiometric flow rates on the overshoot and undershoot of the current density. Qu et al. [23] examined the effects of air stoichiometry on the dynamic behavior and suggested ways to limit undershoot. Shah et al. [24] proposed a one-dimensional transient non-isothermal model to investigate fuel cell transients. Dokkar et al. [25] used a single-phase 3D model to analyze the effects of pressure on oxygen concentration and water removal. Cho et al. [26] focused on the effects of micro-porous GDL architectures on the transient response of PEM fuel cells. Gomez et al. [27] examined the effect of anode and cathode inlet conditions on the stack performance using a transient two-phase model. A comprehensive review of recent developments in multi-scale modeling techniques with focus on transport phenomena, transient response behavior and cold start process can be found in the paper by Song et al. [28]. Although the primary focus of the current article is underline the transients for dry operating conditions where the flow is mostly single phase a comprehensive review of modeling detail for two phase flows and the flow behavior in GDL's can be found in Refs. [29-34].

This chapter presents a model based study of transient behavior of PEM fuel cells, over different operating parameters for dry feed given specified load changes, with the objective of elucidating the effects of operating parameters on fuel cell transients, water content in membrane and determining operating conditions to limit the fuel cell transients to a desired value. Numerical models reported in the literature [18,19] and used in our recent study [36] to elucidate the effect of membrane properties on transients, are used to study the effects of pressure, relative humidity and stoichiometric flow rates on the anode and cathode sides on the water content in the membrane and time taken to reach steady state for step change in voltages.

While the work by Wang and Wang [18] elucidated the membrane hydration/ dehydration behavior for a step change in inlet humidity values at cathode and thus the time scales associated with the process, the effects of operating conditions on the hydration and dehydration process for specified load changes, encountered in practical applications, and their optimization has not been reported in earlier studies and forms the primary focus of the present work. Design windows on operating parameters are constructed to limit the transients to a desired value and the optimum values are identified within the design windows. The primary contribution of the article is not on new numerical modeling, but instead on the use of available models to obtain design insights into the transient behavior of PEM fuel cells.

2.2 Mathematical Model

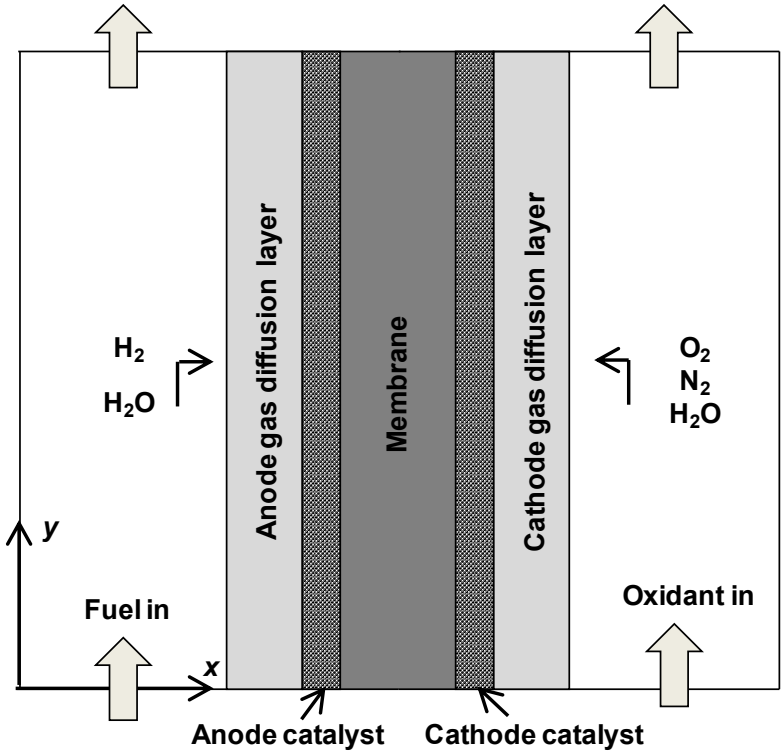

Figure 2.1: Schematic illustration of a PEM fuel cell

Figure 1 shows a schematic of a two-dimensional section of a PEM fuel cell. Gas channels, gas diffusion layers and catalyst layers on the anode and cathode side separated by a selectively permeable membrane forms seven different regions for this study. A comprehensive two-dimensional, single phase, transient, isothermal model based on studies reported in the literature [1,5,7,18,19,35] is used to simulate the fuel cell dynamics. The model takes into consideration important transient processes such as gas transport, water accumulation and

electrochemical double layer discharge. The plane formed by axes across the membrane and along the channel for a single channel forms the computational domain for this study.

The dynamics of fuel cell behavior is governed by the conservation equations of continuity, momentum and species, are as follows [5, 18]:

$$\nabla.\vec{u} = 0 \tag{1}$$

$$\frac{1}{\varepsilon}\left[\frac{\partial \vec{u}}{\partial t} + \frac{1}{\varepsilon}\nabla.(\vec{u}\vec{u})\right] = -\nabla.\left(\frac{p}{\rho}\right) + \nabla.\tau + S_u \tag{2}$$

$$\varepsilon\frac{\partial C_k}{\partial t} + \nabla.(\vec{u}C_k) = \nabla.\left(D_k^{eff}\nabla C_k\right) + S_k \tag{3}$$

where $\vec{u}$ is the superficial velocity vector or volume averaged velocity, ε, the porosity of the porous media, is unity in gas channels, and the source term S_u incorporates the effect of porous media on flow and is expressed in Table 1. A constant density is assumed with no mass source terms, following the assumptions justified in Ref. [18]. Further, C_k represents the molar concentration of species k namely H_2, O_2 and H_2O, and the effective porosity D_k^{eff} is given by [36]:

$$D_k^{eff} = \varepsilon_{eff}^{1.5} D_k \tag{4}$$

in which, D_k, the diffusivity of each species, can be expressed as a function of temperature T and pressure p by the relationship [18]:

$$D_k = D_{k,ref}\left(\frac{T}{353}\right)^{1.5}\left(\frac{1}{p}\right) \tag{5}$$

Eq. (3) is used to describe water transport in the MEA by expressing ε as:

$$\varepsilon = \varepsilon_g + \varepsilon_m\frac{dC_w^m}{dC_w} = \varepsilon_g + \varepsilon_m\frac{\rho_m}{EW}\frac{RT}{p^{sat}}\frac{d\lambda}{da} \tag{6}$$

where ρ_m is the density of the dry membrane, subscripts g and m represents gas and membrane phase, R is the gas constant and EW is the equivalent weight of the dry membrane, taken to be 1.1 kg/ mol. The membrane water content, λ, can be calculated from [37]:

$$\lambda = \begin{cases} 0.043 + 17.81a - 39.85a^2 + 36.0\,a^3 & 0 \le a \le 1 \\ 14 + 1.4(a-1) & 1 \le a \le 3 \\ 16.8 & 3 < a \end{cases} \tag{7}$$

with the water activity, a, and the saturation pressure for water, p^{sat}, expressed as:

$$a = \frac{C_w RT}{p^{sat}} \tag{8}$$

$$\begin{aligned}\log_{10}p^{sat} = {} & -2.1794 + 0.022953(T - 273.15) - 9.1837\times10^{-5}(T-273.15)^2 \\ & +1.4454\times10^{-7}(T-273.15)^3\end{aligned} \tag{9}$$

Coupled with the governing equations, Eqs. (1)–(3), the charge transport equation governs the voltage and current density of the fuel cell and is given by:

$$\nabla.\left(\sigma_i^{eff}\nabla\phi_i\right)+S_i=0;\quad i=s,m \tag{10}$$

where subscripts s and m represent the solid and membrane phase respectively, $\phi_i$is the i-phase potential, σ_i^{eff} represents effective charge conductivity for i-th phase. Since the time constant for electrochemical double layer discharging is order of micro- to milli-seconds, the transient term in Eq. (10) may be neglected for the present study. This treatment leads to instantaneous change in current density given a change in ϕ_s. The EDL (usually of nm thickness) is not modeled separately but is a part of the MEA, which is accounted for in the continuum modeling. As mentioned previously, the mathematical model in this study is based on the work of Wang and Wang [18], in which they clearly discuss the above assumption. The source term S_i is function of transfer current density (j) in catalyst layers and is expressed in Table 1. The current generation in catalyst layers is governed by Butler-Volmer equation, which when simplified can be expressed as:

$$j_a=j_a^{ref}\left(\frac{C_{H_2}}{C_{H_2}^{ref}}\right)\left(\frac{\alpha_a+\alpha_c}{RT}F\eta\right) \tag{11}$$

and

$$j_c=j_c^{ref}\left(\frac{C_{O_2}}{C_{O_2}^{ref}}\right)exp\left(\frac{\alpha_cF\eta}{RT}\right) \tag{12}$$

In the above equations subscripts a and c denote anode and cathode, respectively, j^{ref} is the reference volumetric exchange current density, α is the transfer coefficient, C_{H_2} and $C_{O_2}$are the molar concentration of H_2 and O_2, respectively, F is the Faraday constant, and η is the surface over-potential given by:

$$\eta=\phi_s-\phi_m-V_{ref} \tag{13}$$

where V_{ref} is 0 at the anode side and is equal to the open circuit voltage, V_{OCV}, at the cathode side, is given in terms of temperature T as:

$$V_{OCV}=1.23-0.9\times10^{-3}(T-298) \tag{14}$$

The diffusivity of water in the membrane is determined using the following relationship [38]:

$$D_w^m=\begin{cases}3.1\times10^{-5}\lambda\left(e^{0.28\lambda}-1\right)e^{-\frac{2346}{T}} & 0\le\lambda\le3\\ 4.17\times10^{-8}\lambda(1+161e^{-\lambda})e^{-\frac{2346}{T}} & \lambda>3\end{cases} \tag{15}$$

The ionic conductivity of the membrane σ_m is given by [39]:

$$\sigma_m=(0.005139\lambda-0.00326)exp\left[1286\left(\frac{1}{303}-\frac{1}{T}\right)\right] \tag{16}$$

Equations (1) to (4) form a complete set of governing equations with nine unknowns: $\vec{u}$ (three components), p, C_{H_2}, C_{O_2}, C_{H_2O}, ϕ_s, ϕ_m. The governing equations are subject to appropriate boundary and interface conditions and are discussed in the next section.

The inlet velocities at the gas channel inlets are expressed by the respective stoichiometric flow ratios, i.e. ζ_a and ζ_c defined at a reference current density, I_{ref}, as:

$$\zeta_a = \frac{C_{H_2}\rho_a v_{in,a} A_a}{\frac{I_{ref}A}{2F}} \tag{17}$$

and

$$\zeta_c = \frac{C_{O_2}\rho_c v_{in,c} A_c}{\frac{I_{ref}A}{4F}} \tag{18}$$

where A_a and A_c are the flow areas of the anode and cathode gas channels respectively. The molar concentrations at flow inlets are determined by the inlet pressure and humidity according to the ideal gas laws. At the flow outlet boundaries, fully-developed or no-flux boundary conditions are applied such that $\frac{\partial \vec{u}}{\partial n} = \frac{\partial C_k}{\partial n} = \frac{\partial \phi_m}{\partial n} = \frac{\partial \phi_s}{\partial n} = 0$, and at the walls of the domain, $\vec{u} = \frac{\partial C_k}{\partial n} = \frac{\partial p}{\partial n} = \frac{\partial \phi_m}{\partial n} = 0$. At the GDL and catalyst layer interfaces: $\sigma_m \frac{\partial \phi_m}{\partial n} = 0$. The steady state field reached by starting at zero serves as the initial condition for the transient simulations.

The governing equations and the associated boundary conditions are solved using a control volume based commercial fluid dynamics (CFD) package, ANSYS Fluent®, employing the Pressure-Implicit with Splitting of Operators (PISO) algorithm. The governing equations 1, 2, 3 and 10, and the corresponding source terms are implemented through user-defined functions and user-defined scalars (species and phase potentials). A systematic mesh size convergence study was conducted to determine the discretization for which the difference in the results was less than 0.5% with further reduction in mesh size. An 80 (across the cell) × 40 (along the channel) grid was found to be optimum in terms of accuracy and computational time, with the solution, for a particular time step, converging as the residuals reduce to 10^{-6} for all the equations. A step load change is performed at $t = 0$ by specifying the change in cell potential as boundary condition. The simulation proceeds from the specified steady state point, $t = 0$, to a new steady state point, $t = t_{SS}$, determined by the change in current density with time, $I = 0.995\ I_{SS}$. The geometrical, physical and electrochemical parameters used in this study are listed in Table 2. Numerical simulations were carried out to analyze the effects of anode and cathode pressure, anode and cathode stoichiometric flow ratio, and relative humidity at anode and cathode inlet, on the time taken to reach steady state for step changes in voltage. The ranges of

values for the operating conditions used in this study are listed in Table 3. The results of the simulations are discussed in the next section.

2.3 Results and Discussion

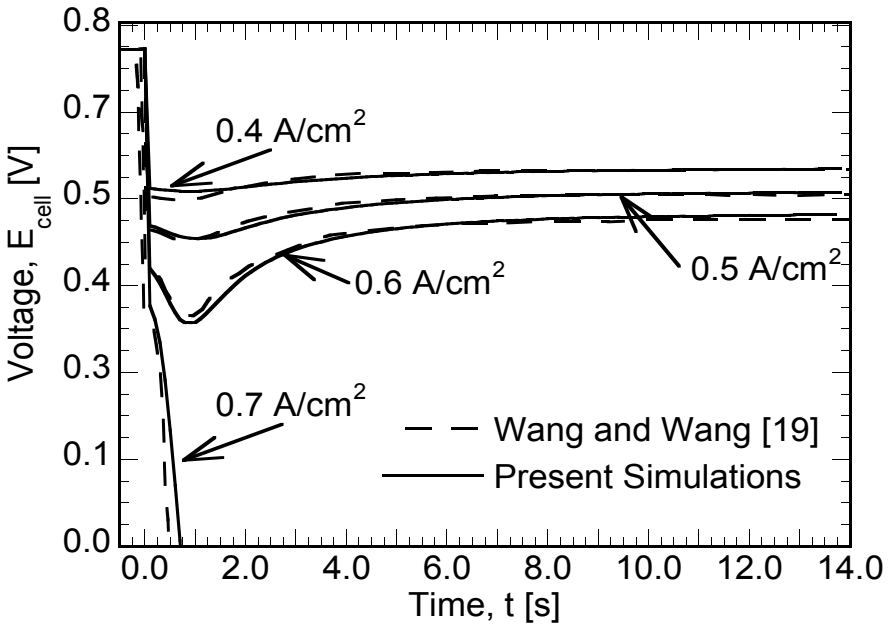

Figure 2.2: Verification of the numerical PEM fuel cell model with numerical data from Ref. [19] for step change in current density from I = 0.1 to 0.4, 0.5, 0.6, 0.7 A/cm^2. The results of the model in this study are represented by solid lines, while those from Ref. [19] are shown as dashed lines.

The numerical model discussed in Section 2 was first validated with the work of Wang and Wang [19], as presented in Fig. 2. The model used by Wang and Wang in Ref. [19] is 3D whereas the current model is 2D, neglecting the rib channel effects. The reference exchange current densities for anode were fitted so as to closely match the observed behavior in Ref. [19]. The values for the parameters used in the current model are stated in Table 2. The results of the model in this study are represented by solid lines, while those from Ref. [19] are shown as dashed lines. Figure 2 shows the cell voltage variation with current density for step change in current density from I = 0.1 to 0.4, 0.5, 0.6, 0.7 A/ cm^2. It can be seen that the cell voltage drops instantaneously owing to the time-scale associated with the electrochemical double layer discharge, on the order of micro- to milli-seconds. In addition, at low-humidity operating conditions, the voltage response is seen in Fig. 2 to exhibit an undershoot, with the degree of undershoot increasing as the magnitude of current change is increased. For I = 0.7 A/ cm^2, Fig. 2

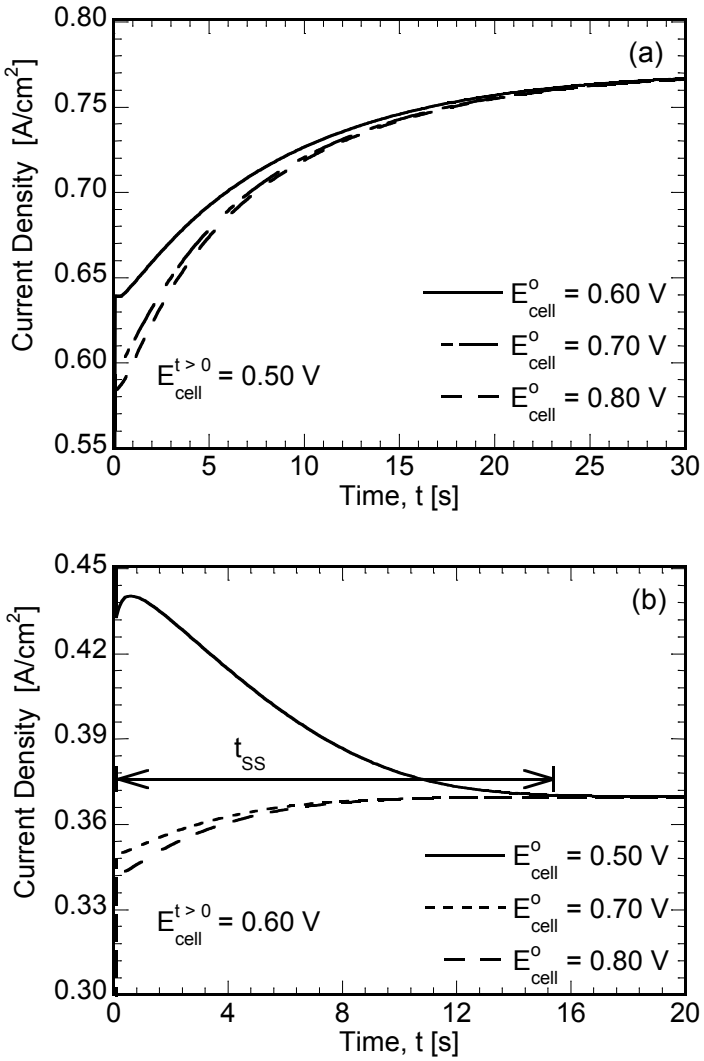

Figure 2.3: Dynamic response of average current density for step change in voltage to $E^{t>0}_{cell}$ (a) 0.50 V and (b) 0.60 V.

shows that the voltage drops to zero, indicating a voltage reversal. The undershoot in the voltage response can be attributed to the jump in water electro-osmotic drag, which increases proportionally to the step change in the current density. This causes the anode to dryout and, in turn, increases the membrane resistance, leading to further drop in the voltage to a minimum. As the membrane at anode is rehydrated, the membrane resistance decreases, leading to increase in voltage and achieving steady state. The time scale associated with the back-diffusion of water dictates the time taken for the voltage response to improve, and is on the order of 0.7 s for the parametric combination considered. The Fig. 2 shows close agreement between the voltage response obtained for the present simulations and those reported in Ref. [14].

To elucidate the fuel cell dynamics for step changes in voltage, numerical simulations were conducted, with the values of the operating conditions fixed to the base values in Table 3, as presented in Fig. 3. It should be noted that the reference current density at the cathode was modified to match the experimental values of current density in Ref. [5] and the results presented in further discussions are based on the new value of reference current density of 100 A/ m^3 for the cathode while other parameters are fixed to that specified in Table 2. Figure 3(a) shows the dynamic response of the average current density for a step change in voltage to $E_{cell}^{t>0}$ = 0.50 V from initial cell voltages, E_{cell}^{0} = 0.60, 0.70 and 0.80 V, with a dry cathode (RH_c = 0%). Owing to the difference in membrane hydration, the initial jump is higher for step change from 0.60 V, as compared to step change from 0.70 and 0.80 V. As the water produced at the cathode catalyst layer further hydrates the membrane, improving the cell performance, the current density increases, reaching steady state at around 30 s, as seen in Fig. 3(a). Operating under dry inlet condition at cathode, the water generated at cathode catalyst layer is readily removed through the gas channel resulting in a longer time to hydrate the membrane for changes from higher cell voltages to 0.50 V. The time taken to reach steady state is longest for change from 0.80 V.

Figure 3(b) shows the dynamic response of the average current density for step change in voltage from 0.5, 0.7 and 0.8 V to 0.6 V. The steady state current densities for 0.70 and 0.80 V are 0.16 and 0.05 A/ cm^2, respectively. It can be seen in Fig. 3(b) that for step change in voltage from 0.5 to 0.6 V, the current density shows an initial instantaneous drop followed by an overshoot and a decrease in current density till steady state is reached. The overshoot observed in Fig. 3(b) can be attributed to the lower oxygen concentration at the reaction sites, while operating at 0.50 V. As the oxygen is replenished at the catalyst layer, it leads to an increase in current density causing the overshoot. With a decrease in water production rate, the membrane dehydrates further, leading to decrease in the current density till a steady state is reached, as seen in Fig. 3(b). The time taken to reach the steady state is defined as t_{SS} for the discussion in this article and represents the time taken for the current density of the fuel cell system to reach 99.9% of the steady state value numerically. Similar to the observation for step change in voltage from 0.70 and 0.80 V to 0.50 V (Fig 3(a)), it can be seen in Fig. 3(b) that the initial jump in the current density is slightly higher for the change from 0.7 V compared to that from 0.8 V, owing to the difference in water content in the membrane. The operation at drier conditions (RH_c = 0%) favors water removal from the membrane, implying faster dehydration, whereas hydration of

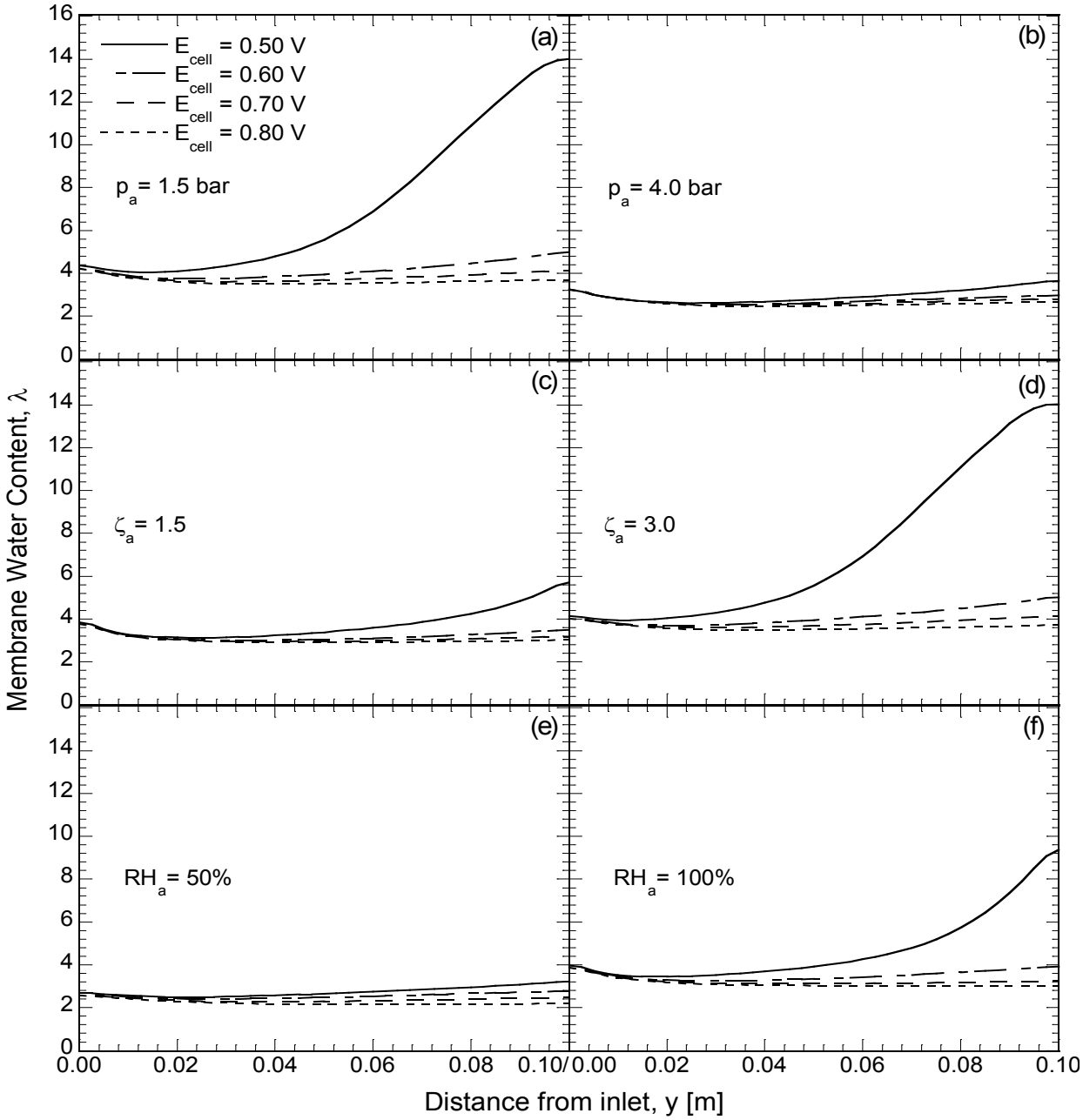

Figure 2.4: Membrane water content, λ, along the membrane centerline for steady state conditions for (a) p_a = 1.5 bar (b) p_a = 4.0 bar (c) ζ_a = 1.5, (d) ζ_a = 3.0 (e) RH_a = 50% and (f) RH_a = 100%.

the membrane is impeded by the loss of water generated at catalyst layer to the dry flow, implying shorter t_{SS} for change from 0.50 to 0.60 V (Fig. 3(b)) in comparison to that observed for change to 0.50 V from 0.60 V (Fig. 3(a)). In general, it is seen in Fig. 3 that following the change in voltage, the current density drops instantaneously owing to the response time associated with the electrochemical double layer discharge. The overshoots and undershoots observed are

related to the diffusion of the species, whereas in most of the cases the transient behavior is governed by the transients of water transport, in particular relating the hydration or dehydration of membrane. The effects of anode and cathode pressure, anode and cathode stoichiometric flow ratio, and relative humidity at anode and cathode inlet, on the time taken to reach steady state, t_{SS}, for step changes in voltage are examined in the following discussion.

Figures 4(a) and (b) show the water content along the membrane centerline, for p_a = 1.5 bar (Fig. 4(a)) and 4.0 bar (Fig. 4(b)), respectively, for various cell voltages. It can be seen from Fig. 4(a) that there is a significant increase in the water content along the membrane length for 0.50 V compared to that observed for other higher voltages, > 0.60 V. It is also noted from Fig. 4(a) that there is relatively small difference in water content values for 0.60, 0.70 and 0.80 V compared to that for 0.50 V. This is can be attributed to the differences in the current density and the removal rate of water generated at the cathode catalyst layer though the dry cathode feed. A comparison of Figs. 4(a) and 4(b) also shows that there is significant reduction in water content values with increase in pressure, for 0.50 V. For a specified stoichiometric flow ratio, increase in anode pressure leads to decrease in inlet velocity, implying decreased water supply rate to anode catalyst layer and, in turn, reduced membrane water content and low current densities.

Figures 4(c) and (d) depict the effects of anode stoichiometry (ζ_a) on the variations in the membrane water content, λ, along the membrane centerline for ζ_a = 1.5 (Fig. 4(c)) and ζ_a = 3.0 (Fig. 4(d)). A change in the anode stoichiometric flow ratio is accomplished by increasing the mass flow rate at anode, while the other operating conditions are fixed at the base values listed in Table 3. For a constant pressure, change in stoichiometry is realized by changing the inlet velocities at the inlets. An increase in the anode stoichiometry leads to an increase in the rate at which hydrogen and water are supplied in the anode channel. for E_{cell} = 0.50 V, it can be seen that there is significant increase in the membrane hydration along the length of the fuel cell, whereas the change in water content of the membrane is relatively small for E_{cell} = 0.60 V, 0.70 V and 0.80 V. The effects of relative humidity at anode, RH_a, are discussed in Fig. 4(e) and (f). Fully humidified and dry inlet corresponds to 100% and 0% RH, respectively. Figures 4(e) and (f) show the membrane water content values along the membrane centerline for RH_a = 50% (Fig. 4(e)) and RH_a = 100% (Fig. 4(f)). There is a significant reduction in water content value for RH_a = 50% (Fig. 4(e)), compared to when operating at a fully humidified anode feed RH_a = 100% (Fig. 4(f)). This can be attributed to decrease in water supply rate to anode layers at lower

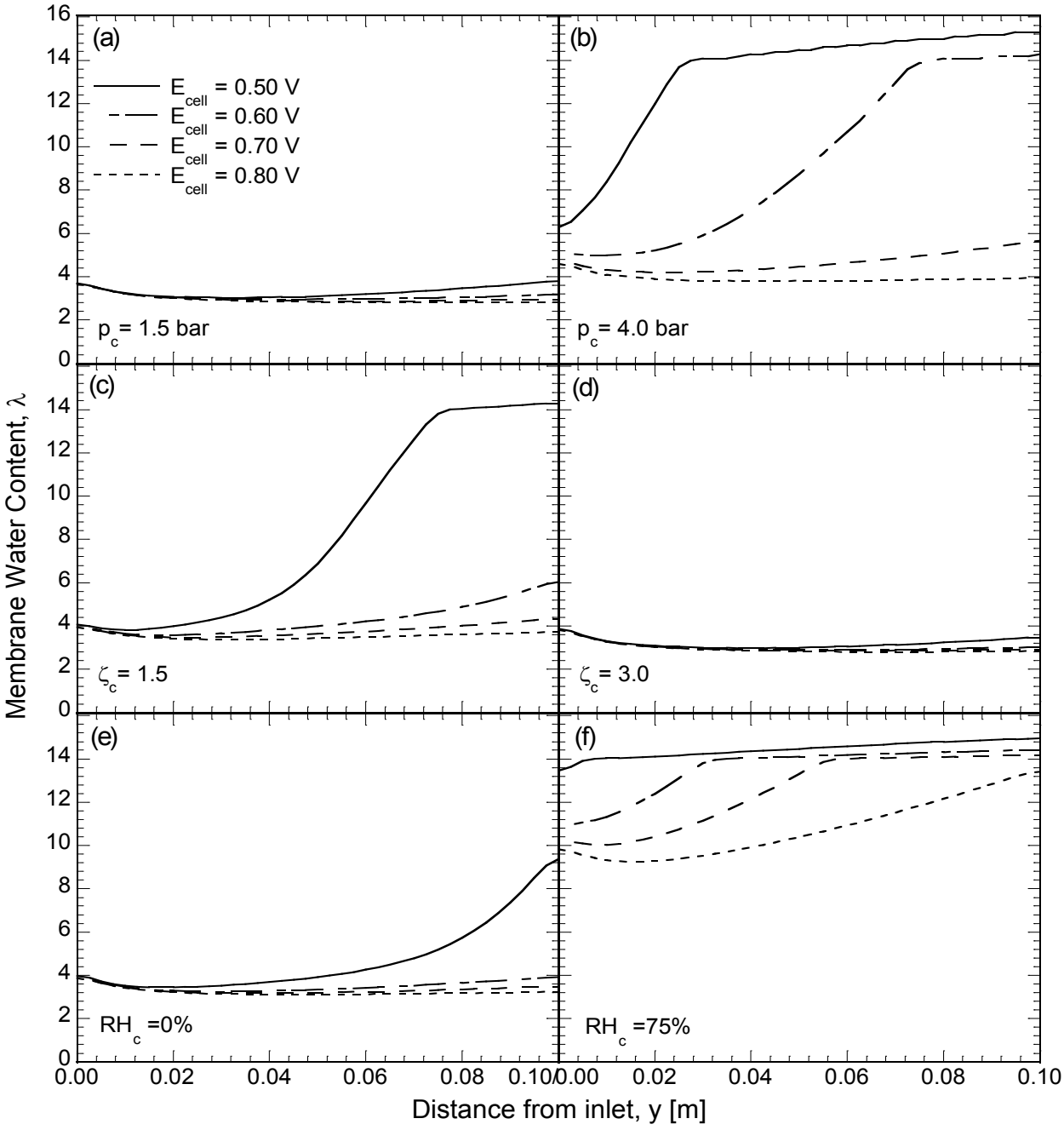

Figure 2.5: Membrane water content, λ, along the membrane centerline for steady state conditions for (a) p_c = 1.5 bar (b) p_c = 4.0 bar (c) ζ_c = 1.5, (d) ζ_c = 3.0 (e) RH_c = 0% and (f) RH_c = 75%.

inlet humidity leading to increase in the membrane resistance, hence lower current density and water content values.

Figure 5(a)–(f) presents the effects of the operating parameters at the cathode on the membrane water content along the membrane centerline. Figure 5(b) shows a significant

increase in the membrane water content along the length compared to that observed for p_c = 1.5 bar (Fig. 5(a)). It can be seen from Fig. 5(b) that the membrane gets fully saturated at the near end region for E_{cell} = 0.60 V and is saturated, for y > 0.02 m, for E_{cell} = 0.50 V. Increase in pressure leads to higher gas density and hence higher concentration of reactants per unit volume. For a specified cathode stoichiometric flow ratio, increase in cathode pressure also leads to reduced velocity at cathode inlet (Eq. 15), affecting the rate at which the water generated at catalyst layer is transported out by bulk gas channel flow. Thus, an increase oxygen concentration, implying higher reaction rate at cathode catalyst layers, along with the decrease in the rate at which water is transported out of the cathode leads to an increase in the membrane water content, for increase in cathode pressure.

Figures 5(c) and (d) present the effects of cathode stoichiometric flow ratio, ζ_c, on the water content along the membrane centerline, for ζ_c = 1.5 (Fig. 5(c)) and ζ_c = 3.0 (Fig. 5(d)). Increase in stoichiometric flow ratio, is specified as an increase in cathode mass flow rate and, in turn, an increase in cathode inlet velocity. There is a significant drop in the water content values for 0.50 V when cathode stoichiometry increases from 1.5 to 3.0, as seen from Figs. 5(c) and (d). Change in stoichiometric flow ratio affects the rate at which water generated at the cathode catalyst layer is removed by bulk mass flow in the gas channel. Increase in the cathode inlet velocity would increase the effective water removal rate through cathode feed, thus affecting the membrane hydration, which otherwise would retain higher water due to lower removal rate. Increase in ζ_c also leads to an increase in the rate of supply of oxygen to the cathode catalyst layers.

Figures 5(e) and 5(f) show the membrane water along the membrane centerline for RH_c = 0% (Fig. 5(e)) and RH_c = 75% (Fig. 5(f)). There is a significant increase in the membrane water content values both at inlet and along the channel with the increase in RH_c, owing to the cumulative effect of humidified feed and high current density, as seen from Figs. 5(e) and (f). It can be seen from Fig. 5(f) that membrane is almost saturated all along the length for E_{cell} = 0.50 V, whereas for E_{cell} = 0.60 V the membrane is saturated for y > 0.025 m. It can be noted from Fig. 5 that relatively higher cathode pressure and RH at cathode inlet leads to saturation of membrane and can further lead to a two phase flow in the fuel cell system, which may be considered in a future study. Figure 6 shows the variation of steady state time, t_{SS}, for step changes in voltage, as a function of anode pressure, p_a (Fig. 6(a)), anode stoichiometric ratio, ζ_a

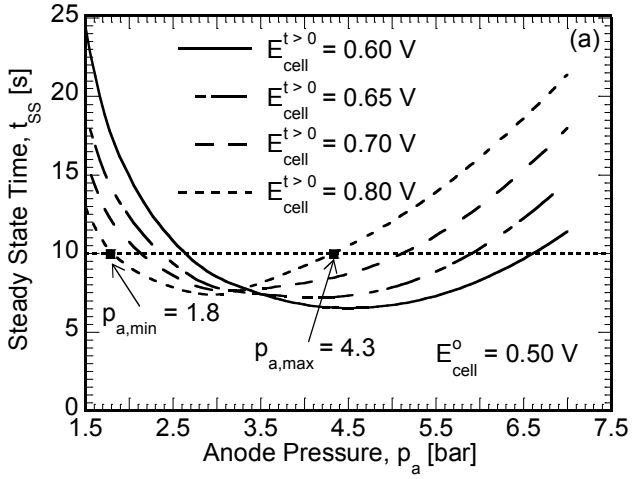

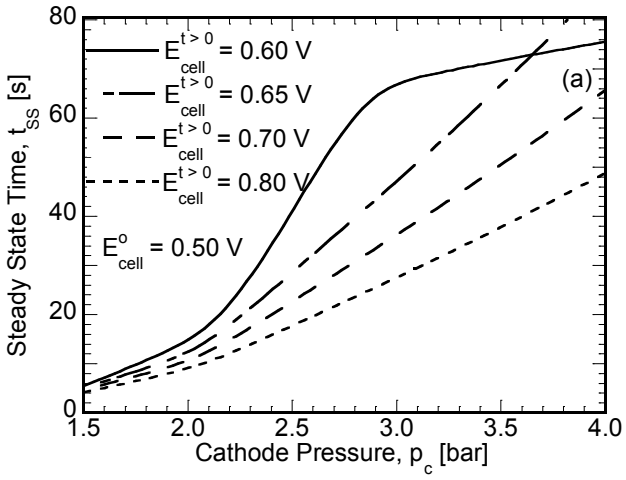

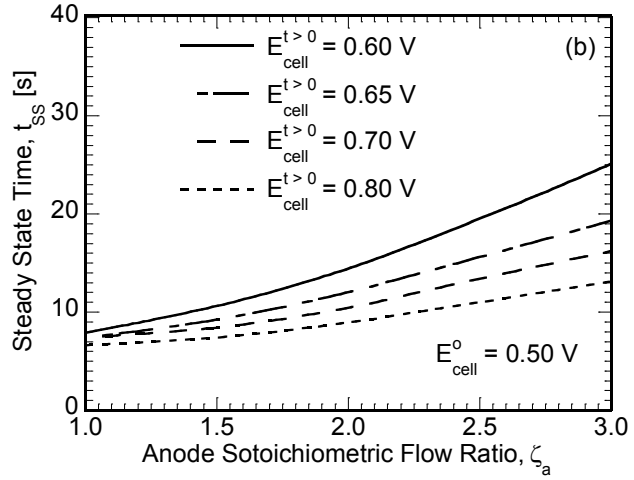

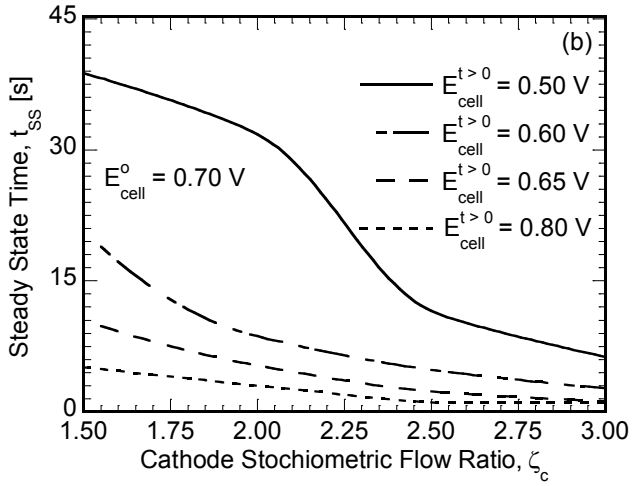

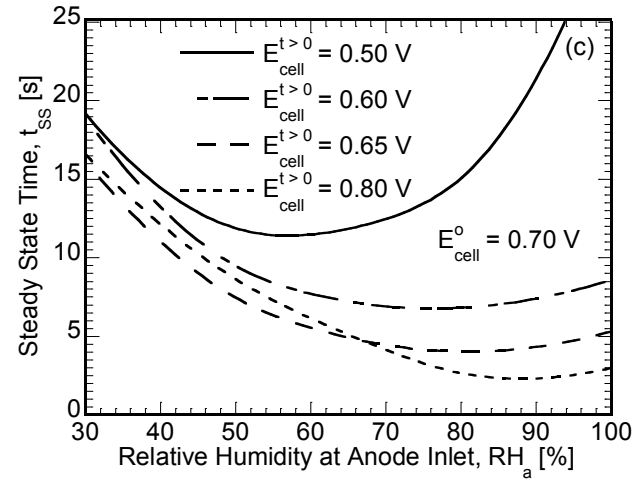

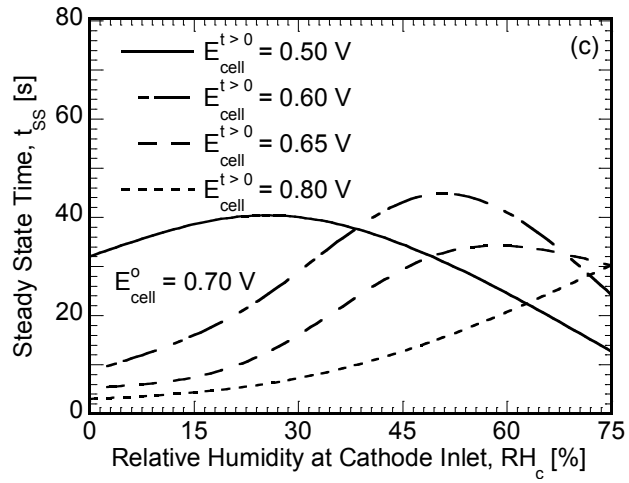

Figure 2.6: Variations in steady state time t_{SS}, as a function of (a) Anode pressure p_a, (b) Anode stoichiometric flow ratio ζ_a and (c) Anode humidity RH_a, for step change in voltage from 0.50 V, 0.50 V and 0.70 V, respectively.

Figure 2.7: Variations in steady state time t_{SS}, as a function of (a) Cathode pressure p_c, (b) Cathode stoichiometric flow ratio ζ_c and (c) Cathode humidity RH_c, for step change in voltage from 0.50 V, 0.70 V and 0.70 V, respectively.

(Fig. 6(b)) and relative humidity at anode inlet, RH_a (Fig. 6(c)). In each case, other than the parameter being studied, all operating conditions were fixed at the base values as in Table 3.

Figure 6(a) presents the variations in t_{SS} for step change in voltage from 0.50 V to $E_{cell}^{t>0}$ = 0.60, 0.65, 0.70 and 0.80 V, and shows that the variations are non-monotonic. It is noted that, for step change in voltage, the time taken to reach steady state at first decreases, reaching minimum for a certain anode pressure, and then increases as the pressure is increased further. The initial decrease in t_{SS} can be attributed to the decrease in water content values with the increase in p_a (Fig. 4(a) and (b)). Further increase in anode pressure is accompanied with decrease in the rate at which water is transported out of the fuel cell system through anode gas channel leading to an increase in t_{SS} for increase in anode pressure, as seen in Fig. 6(a). The anode pressure that minimizes the time to reach steady state decreases as the step change magnitude, $E_{cell}^{t>0} - E_{cell}^{0}$, increases from 0.1 V to 0.3 V. It can further be seen from Fig. 6(a) that for p_a < 3 bars, the voltage increase from 0.50 V to 0.60 V takes the longest to reach steady state. As established earlier, water generation hinders the dehydration process, but with decreasing water production rate, beyond a certain anode pressure, it no longer has significant effect on the dehydration process and the time taken is instead governed by the absolute difference in water content values. Hence for the higher anode pressure, p_a > 3.5 bars, it takes longer for the system to reach steady state for change in voltage from 0.50 V to 0.80 V than it takes for the change to 0.60 V.

Figure 6(b) shows the variations in t_{SS} as a function of anode stoichiometric flow ratio, ζ_a, for E_{cell}^{o} = 0.50. In contrast to the observation in Fig. 6(a), it can be seen from Fig. 6(b) that there is monotonic increase in the time taken to reach steady state with the increase in ζ_a, for a step change in voltage from 0.50 V to higher cell voltages. For the changes in voltage from E_{cell}^{o} = 0.50 V to higher values, the membrane undergoes dehydration, with the difference in water content being minimized for the lower anode stoichiometric flow ratios. The increase in t_{SS} with ζ_a can be attributed to the increase in difference in water content values, as the anode stoichiometry is increased (Figs. 4(c) and (d)). It can be seen from Fig. 6(b) that for a given ζ_a, t_{SS} is maximum for change in voltage to 0.60 V and minimum for change to 0.80 V. This behavior can be attributed to the fact that the current generation hinders the dehydration process, resulting in longer time for the fuel cell system to reach steady state for change to 0.60 V in comparison to that observed for 0.70 or 0.80 V. Figure 6(c) presents the variation in t_{SS}, as a function of RH_a for E_{cell}^{o} = 0.70 V and shows that the variations are non-monotonic. It can be seen from Fig. 6(c) that t_{SS} at first decreases with the increase in RH_a, reaching a minimum

followed by an increase in t_{SS} for further increase in RH_a. Unlike that observed in Figs. 6(a) and (b) it is noted from Fig. 6(c) that the membrane undergoes hydration for change to $E_{cell}^{t>0}$ = 0.50, 0.60 and 0.65 V, with the lower anode humidity conditions resembling the scenarios with high anode pressure. It can be seen from Fig.6(c) that it takes the cell longest for step change to 0.50 V. The anode inlet relative humidity that minimizes the time to reach steady state increases as the step change magnitude, $E_{cell}^{t>0} - E_{cell}^{0}$, increases from -0.2 V to 0.1 V. It is also noted from Fig. 6(c) that the t_{SS} falls below 5 s for RH_a > 70% for $E_{cell}^{t>0}$ = 0.80 V implying faster dehydration at higher humidification values compared to that observed for lower values of anode humidification.

While Figure 6 focused on the effects of operating parameters at the anode, Fig. 7 discusses the effects of operating parameters at the cathode namely, the cathode pressure, stoichiometry and relative humidity at inlet. Figure 7(a) shows the variation of t_{SS} as a function of cathode pressure, p_c, for step change in voltages while other operating conditions are fixed at the base values in Table 3. Figure 7(a) presents the variations for step change in voltage from E_{cell}^{o} = 0.50 V to $E_{cell}^{t>0}$= 0.60 V, 0.65 V, 0.70 V and 0.80 V. Owing to the significant increase in water content values (Fig. 5(b)) in comparison to that observed in Fig. 4, it can be seen from Fig. 7(a), that the time taken to reach steady state increases significantly. The value of t_{SS} increases with the increase in cathode pressure, owing to the increase in current density leading to increase in time taken for the dehydration of membrane, as seen in Fig. 7(a). Figure 7(b) presents the variation in t_{SS} as a function of ζ_c, while other operating conditions are fixed at base values in Table 3. The results correspond to step changes in voltage from E_{cell}^{o} = 0.70 V to $E_{cell}^{t>0}$ = 0.50, 0.60, 0.65 and 0.80 V. It can be seen that t_{SS} decreases with the increase in ζ_c for all the load changes owing to the decrease in difference in the membrane water content. With the increase in the cathode flow rate, the system dehydrates rapidly and, correspondingly, the time to reach steady state shows a monotonic decrease. It is also noted that for lower values of ζ_c, the time to reach steady state for hydration is much higher for a load change from 0.70 V to 0.50 V compared to that for other load changes. This behavior can be attributed to the larger difference in water content values for 0.50 and 0.70 V compared to that observed for other voltages.

Figure 7(c) presents the variation in t_{SS} as a function of relative humidity at cathode inlet, RH_c, while the other operating conditions are fixed at base values in Table 3. It can be seen from Fig. 7(c) that for the range of RH_c considered in this study, t_{SS} generally exhibits a non-monotonic variation with increase in cathode relative humidity (RH_c). The increase in t_{SS} can be

attributed to increase in current density, delaying the dehydration process. Also, since the feed is humidified, it is further difficult for the membrane to lose water, compared to when the feed is completely dry. The decrease in t_{SS} for $E_{cell}^{t>0}$ = 0.50, 0.60 and 0.65 V (Fig. 7(c)) at higher relative humidity can be attributed to the diminishing difference in water content values at higher RH_c (Figs. 5(e) and (f)). Also, the fact that the inlet front of the membrane, which responds quickly to voltage changes, shows the major difference in water content for higher RH_c values (Fig. 5(f)), contributes to the decrease in t_{SS} for $E_{cell}^{t>0}$ = 0.50, 0.60 and 0.65 V (Fig. 7(c)). It is also noted from Fig. 7(c) that for step change from E_{cell}^{0} = 0.70 V to $E_{cell}^{t>0}$ = 0.80 V, t_{SS} increases monotonically with increase in RH_c over the range studied. The non-monotonic trends in the variations for the other values of $E_{cell}^{t>0}$ in Fig. 7(c), suggest that a decrease in the time to reach steady state may be observed for RH_c > 75%, although it may not be of practical interest.

The variations in Figs. 6 and 7 may be used to identify upper and lower bounds on the operating parameters at the anode and the cathode for which the time to reach steady state is maintained within a specified value, for given load changes. For this study, the desired value is chosen to be 10 s as an example, i.e., t_{SS} < 10 s, implying that given an instantaneous load change, it does not take more than 10 s for the system to reach steady state. For example, Fig. 6(a) shows that for $E_{cell}^{t>0}$ = 0.80 V, t_{SS} < 10 s for anode pressures between $p_{a,min}$ = 1.8 bar and $p_{a,max}$ = 4.3 bar. It is also seen in Fig. 6(a) that this range increases as $E_{cell}^{t>0}$ decreases to 0.60 V. Similarly, the other variations in Figs. 6 and 7 define either lower bounds (Figs. 6(c) and 7(b)) or upper bounds (Figs. 6(b), 7(a) and 7(c)), based on this example of t_{SS} < 10 s. In these cases, the corresponding upper or lower bounds are taken to be the (upper or lower) ends of the ranges of the parameter considered. Based on the identified upper and lower bounds, design windows can be constructed for the operating conditions, as presented in Figs. 8 and 9 for the anode and cathode parameters, respectively.

Figures 8(a), (b) and (c) present the operating windows for the anode pressure, anode stoichiometric flow ratio and relative humidity at anode inlet, respectively, as a function of the change in the voltage, $\Delta E_{cell} = \left(E_{cell}^{t>0} - E_{cell}^{0}\right)$. Each figure is divided in four zones, with each zone representing the design window for different E_{cell}^{o} (0.8, 0.7, 0.6 and 0.5 V). It can be seen that, for step change from E_{cell}^{o} = 0.8 V to $E_{cell}^{t>0}$ = 0.5 V, ΔE_{cell} = –0.3 V, there exists no anode operating parameters, over the range studied, that result in t_{SS} < 10 s. It is also seen that for change to 0.5 V from E_{cell}^{o} = 0.7, the design window does not present any operable range for anode stoichiometry (Fig. 8(b)) and relative humidity (Fig. 8(c)). It is noted in Fig. 8(a) that the

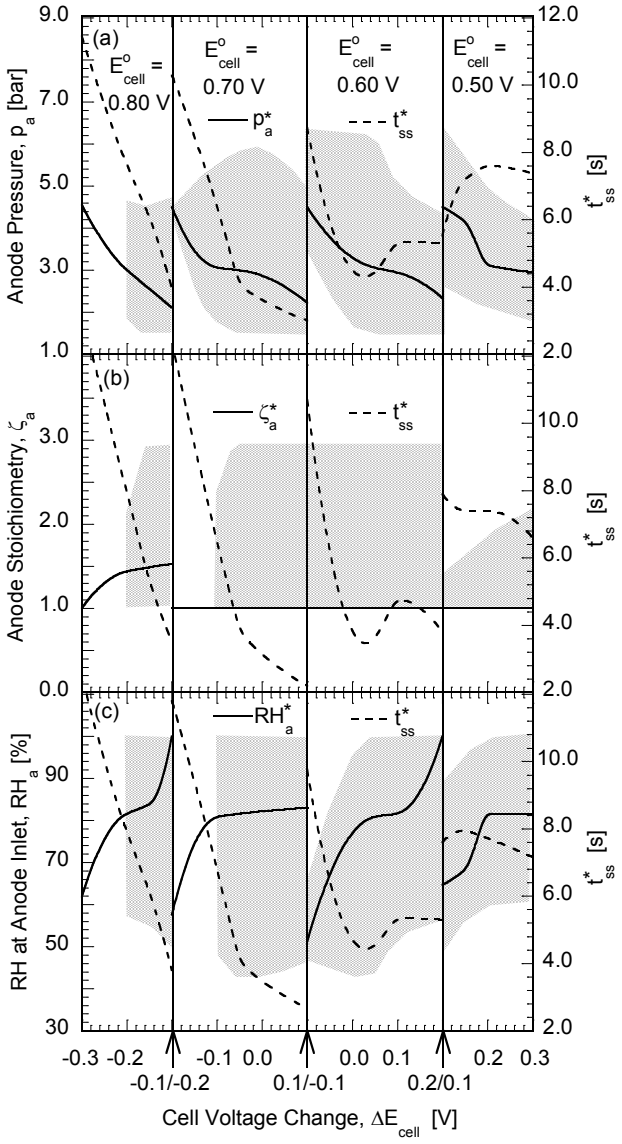

Figure 2.8: Operating window, such that t_{SS} < 10 s, for (a) anode pressure, p_a, (b) anode stoichiometric flow ratio, ζ_a, and (c) anode relative humidity RH_a, as a function of cell voltage change, ΔE_{cell}, with the variations in optimum time (t^*_{SS}) and operating parameters (a) p^*_a (b) ζ^*_a and (c) RH^*_a superimposed with dotted and solid lines, respectively.

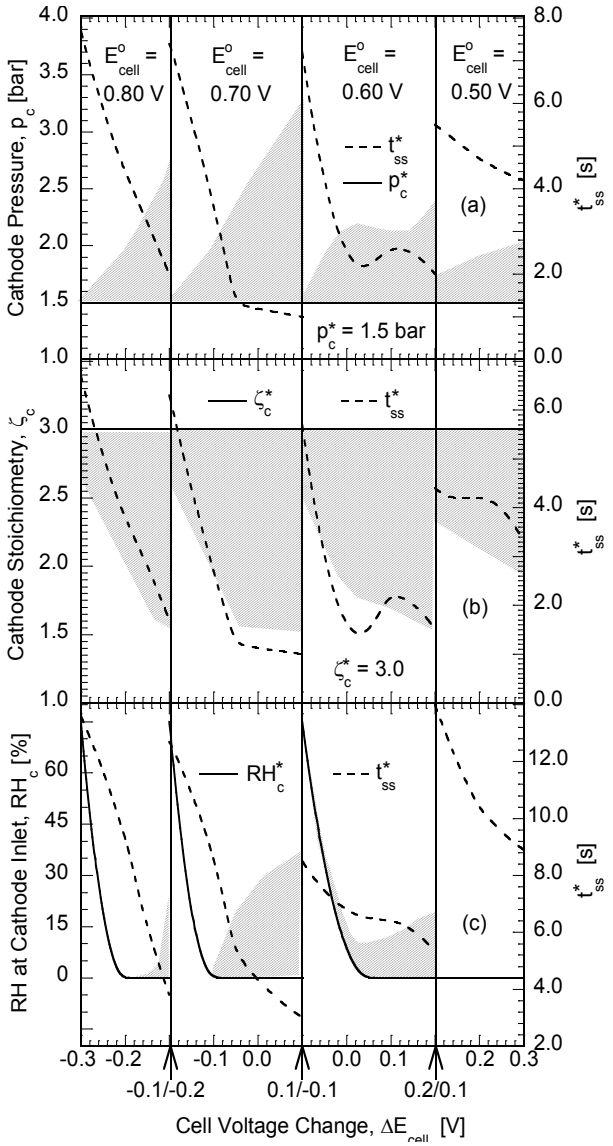

Figure 2.9: Operating window, such that t_{SS} < 10 s, for (a) cathode pressure, p_c, (b) cathode stoichiometric flow ratio, ζ_c, and (c) cathode relative humidity RH_c, as a function of cell voltage change, ΔE_{cell}, with the variations in optimum time (t^*_{SS}) superimposed with dotted lines.

upper and lower limit for E^o_{cell} = 0.6 and 0.5 V show monotonic decrease for step change to higher voltages ($\Delta E_{cell} > 0$), shifting the operating window towards lower pressure. In contrast, for E^o_{cell} = 0.70 V, the upper limit decreases, with increasing lower limit, narrowing the feasible region of operation for step change to lower voltages ($\Delta E_{cell} < 0$), whereas for step change to

higher voltage ($\Delta E_{cell} > 0$) lower limit remains fixed with decrease in upper limit, indicating that hydration time for membrane is minimized for higher anode pressure.

Figure 8(b) presents the design window for anode stoichiometric flow ratio, in which the lowest value used for the study forms the lower bound for the window, for all the cases, whereas the upper bound is either varying or fixed by the highest value used for study. It is noted that the change from 0.60 V to other loads does not take more than 10 s over the entire range of study, as seen in Fig. 8(b). In contrast to the observation for E^o_{cell} = 0.60 V in Fig. 8(b), for E^o_{cell} = 0.80, 0.70 and 0.50 V, the upper limit increases monotonically with increase in ΔE_{cell}, presenting wide range of operation for higher ΔE_{cell}. Figure 8(c) presents the operating window for relative humidity for anode inlet (RH_a). Recalling from discussion of Fig. 6(c), t_{SS} at first decreases with increase in RH_a, followed by increase in t_{SS} as RH_a is increased further, presenting a wide range for operation for which $t_{SS} \leq 10$ s. For E^o_{cell} = 0.50, the lower and upper limits show monotonic increase with increase in ΔE_{cell}, indicating that the response to a step change to relatively higher voltage is faster at the higher RH_a. Similar to the observation in Figs. 8(a) and 8(b), the design windows in Fig. 8(c) exhibit a wide range of operability for the change to higher voltages from a given initial voltage, such that $t_{SS} \leq 10$ s.

Design windows similar to those in Fig. 8 are constructed for the cathode operating parameters, as presented in Fig. 9. Figures 9(a), (b) and (c) show the operating windows for cathode pressure, stoichiometric flow ratio and relative humidity, respectively, such that $t_{SS} \leq$ 10 s. It can be seen from Fig. 9(a) that the lower limit for cathode pressure is fixed by the lower limit on the operating range in Table 3, that is p_c = 1.5 bar, and remains fixed for all the cases with changing ΔE_{cell}. This can be attributed to the monotonic behavior of t_{SS} as a function of cathode pressure (Fig. 7(a)). The upper limits show a monotonic increase with increase in ΔE_{cell}, for E^o_{cell} = 0.80 V, 0.70 and 0.50 V, whereas it is non-monotonic for 0.60 V. It can be seen from Fig. 9(a), that a wider operating range is obtained as ΔE_{cell} increases for all E^o_{cell}. The steady state time, t_{SS}, shows a monotonic decrease with the increase in cathode stoichiometric flow ratio (Fig. 7(b)), thus fixing the upper limit for operating window for ζ_c in Fig. 9(b) to 3.0, which is the upper limit of the range studied (Table 3). On the other hand, the lower bound of the design windows show a monotonic decrease for increase in ΔE_{cell}, resulting in a wider operating range for higher ΔE_{cell} in Fig. 9(b). Figure 9(c) shows the design windows on the cathode relative humidity, RH_c. Increase in cathode relative humidity results in significant increase in membrane water content for E^o_{cell} = 0.50 V, thus increasing t_{SS}. Hence, for E^o_{cell} = 0.50

V, there exists no window for which $t_{SS} \leq 10$ s; also, t_{SS} for step change to 0.50 V from 0.70 and 0.80 V is greater than 10 s, and is not seen in the operating window. With increasing membrane hydration, the steady state time for step change from 0.60 to 0.50 V falls below 10 s at around 75% RH_c and is thus represented as a narrow region for E^o_{cell} = 0.60 V in Figure 9(c).

In addition to identifying the design windows for operation, based on limiting the transient duration to a desired value, Figures 6 and 7 may also be used to identify the optimum values of the operating parameters—$p^*_a, \zeta^*_a, RH^*_a, p^*_c, \zeta^*_c$ and RH^*_c—for which the time to reach steady state is minimized, t^*_{SS}. In cases where the variation of t_{SS} is non-monotonic, the optimum value occurs in the middle of the range of the parameters (such as p^*_a in Fig. 6(a) and RH^*_a in Fig. 6(c)); for t_{SS} variations that are monotonically increasing, the optimum values occur at the lower end of the range, as in the case of ζ^*_a and p^*_c in Figs. 6(b) and 7(a), respectively; for the monotonically decreasing t_{SS} variation with the cathode stoichiometric ratio, the optimum value, ζ^*_c, occurs at the upper end of the range, as in Fig. 7(b). In the case of the cathode relative humidity, Fig. 7(c), the optimum relative humidity, RH^*_c, is at the lower end of the range, 0%, for $E^{t>0}_{cell} \geq 0.60$ V, and at the upper end of the range, 75%, for $E^{t>0}_{cell} = 0.50$ V.

The variation of the optimum values of the operating parameters with ΔE_{cell}, for the different E^o_{cell} values are superposed as the solid lines on the plots in Figs. 8 and 9. The corresponding minimum times to reach steady state, t^*_{SS}, are indicated by the dotted lines at different ΔE_{cell} values along each of the lines. From Fig. 8(a) it is evident that the optimum anode pressure decreases monotonically with ΔE_{cell} for all values of E^o_{cell} studied. The optimum anode pressure, p^*_a, lies between 2.0 to 4.5 bar for E^o_{cell} = 0.80, 0.70 and 0.60 V, whereas for E^o_{cell} = 0.50 V, it varies over a narrower range, 3.0 to 4.5 bar, indicating that it is easier to dehydrate membrane for lower membrane water content. It is also noted from Fig. 8(a) that for step change to lower voltages from E^o_{cell} = 0.80 V, the optimum time (t^*_{SS}) decreases monotonically with increase in ΔE_{cell}, emphasizing the dominance of membrane water transport in the transient process for step change to lower voltages. For E^o_{cell} = 0.50 V, the optimum time first increases with ΔE_{cell}, reaching a maxima at ΔE_{cell} = 0.2 V and then decreases for ΔE_{cell} = 0.3 V. The increase in t^*_{SS} with ΔE_{cell} can be attributed to the fact that the minima for $\Delta E_{cell} \leq 0.2$ V occurs at relatively higher anode pressure, implying that the dehydration time is proportional to the absolute difference in water content values, whereas the minima for ΔE_{cell} = 0.3 V occurs at relatively lower anode pressure. The observed curves and window are a result of smoothening

of the data for upper and lower limits, thus the above window for a voltage change of 0 V. Ideally, a discontinuous behavior is to be observed as no data exist in the near 0 V change.

Figure 8(b) presents the variation of optimum anode stoichiometry, ζ_a^*, as a function of ΔE_{cell} superposed on to the design window. It can be seen that for the step load changes considered, ζ_a^* = 1.0, except for change in cell voltage from 0.80 V to 0.60, 0.65 and 0.70 V, for which the ζ_a^* = 1.44, 1.49 and 1.53, respectively. For E_{cell}^o = 0.80, 0.70 and 0.50 V, the optimum time, t_{SS}^*, decreases monotonically with increase in the ΔE_{cell}, whereas t_{SS}^* for E_{cell}^o = 0.60 shows a non-monotonic behavior, as seen in the values mentioned in Fig. 8(b). It is noted that, in general, the optimum occurs when water content is low, reducing the dominance of membrane water transport on transient process.

Figure 8(c) presents the superposed variations of the optimum anode inlet relative humidity (RH_a^*) and the corresponding time (t_{SS}^*) with ΔE_{cell} for different E_{cell}^o. It can be seen that, for E_{cell}^o = 0.80 V, RH_a^* increases with the increase in ΔE_{cell}, whereas the optimum time shows a monotonic decrease with increase in ΔE_{cell}. The observed variation shows an inverse trend with respect to that for the anode pressure, in that high anode pressure operation resembles low humidity conditions. It can be seen that the optimum time for ΔE_{cell} = –0.3 V occurs at relatively low humidity (RH_a^* ~ 60%), ensuring low membrane water content for faster humidification, whereas for change to 0.70 V, the fastest response is observed for RH_a^* = 100%. Similarly, for E_{cell}^o = 0.50 V, the optimum time occurs for low humidity operation, for which dehydration is rapid and membrane water content is low. It is noted here that RH_a^* varies from 60–100% for E_{cell}^o = 0.80 V and 0.70 V, whereas for E_{cell}^o = 0.50 V, RH_a^* varies from 60–80%, with E_{cell}^o = 0.60 V showing the widest range for RH_a^* from 50% to 100%. It is also seen that for E_{cell}^o = 0.5 V, t_{SS}^* varies over the range of 7–8 s, whereas other E_{cell}^o values are associated with a wider variation for t_{SS}^*.

Figure 9(a) shows that p_c^* = 1.5 bar is the optimum cathode pressure that minimizes the time to reach steady state, for all values of E_{cell}^o and ΔE_{cell}. For a fixed stoichiometric flow ratio, there is increase in the molar concentration of oxygen accompanied by decrease in inlet flow velocity, for increase in cathode pressure. This leads to reduction in the rate at which water generated at cathode catalyst layer is removed through bulk flow in cathode gas channel. Hence the minimum for t_{SS} occurs at lower cathode pressures (Fig. 7(a)), which in this case is p_c^* = 1.5 bar. For E_{cell}^o = 0.80, 0.70 and 0.50 V, the optimum time, t_{SS}^*, decreases monotonically with increase in the voltage change value, whereas for E_{cell}^o = 0.60 V, t_{SS}^* shows a non-monotonic behavior. It is

also seen that the t_{SS}^{*} ranges from 1 to 8 s, indicating the reduced dominance of membrane water transport process for low cathode pressures.

Figure 9(b) shows that due to the monotonic decrease of t_{SS} with ζ_c, seen in Fig. 7(b), the optimum stoichiometric ratio that minimizes the time to reach steady state is at the upper end of the range of ζ_c studied, i.e., ζ_c^{*} = 3.0. At ζ_c = 3.0, the water content difference is minimized for the range studied, reducing the time associated with membrane water uptake or dehydration. The corresponding values of t_{SS}^{*}, indicated in Fig. 9(b) as a function of ΔE_{cell}, demonstrate a similarity to the trend observed for the anode stoichiometric flow ratio (Fig. 8(b)). However, the values of t_{SS}^{*} range between 1 to 7 s in Fig. 9(b), in comparison to the higher values in Fig. 8(b), indicating that the transients at the higher ζ_c are faster than those observed for the lower ζ_a.

Figure 9(c) presents the variations in RH_c^{*} and the corresponding optimum times, t_{SS}^{*}, as a function of ΔE_{cell}, superposed on the design windows. The optimum relative humidity at cathode inlet (RH_c^{*}) is 0%, except for changes to 0.50 V from higher voltages (E_{cell}^{o} = 0.80, 0.70 and 0.60 V), for which RH_c^{*} is 75%, as seen in Fig. 9(c). This behavior can be attributed to the increased membrane hydration and high current density for humidified feed at cathode (RH_c > 0%), leading to faster hydration of the membrane in comparison to that observed for lower RH_c, whereas transients for other changes are much quicker at RH_c = 0%. It can be seen that t_{SS}^{*} decreases monotonically with increase in ΔE_{cell}, for all the cell voltages, E_{cell}^{o}, studied.

From Figs. 8 and 9, it can be seen that operating at higher cathode stoichiometric flow rate leads to least transient time for all the combination of E_{cell}^{o} and ΔE_{cell} studied. It is noted that the least transient time occurs for cathode stoichiometric flow ratio of 3.0, ζ_c^{*} = 3.0, with other operating parameters fixed to base value in Table 3. The optimum values for parameters leading to least transient time are p_a^{*} = 2 bar, p_c^{*} = 2 bar, ζ_a^{*} = 2.0, ζ_c^{*} = 3.0, RH_a^{*} = 100% and RH_c^{*} = 0%. The increase in flow rate at cathode side leads to minimization of difference in water content values accompanied with rapid dehydration for change from lower to higher voltages, thus presenting the observed minimum.

The power density can be directly obtained based on the results of current study and is related to the cell voltage. The design windows are presented as a function of load change, expressed in terms of the voltage change in the study, but can just as easily be expressed in terms of the change in the power. Correspondingly, the design windows can be easily converted in to windows based on power change, although the design window would be the same as that presented for the specified design objectives considered. An analysis of efficiency

would require consideration of a stack and systems required to maintain the flow conditions such as pressure, flow rate, humidity, which may be treated in a future work. The power density corresponding to the optimum curves in Figs 8 and 9 is presented in Table 4 for E_{cell}^{o} = 0.50 V and 0.70 V. The power density for a given load change ΔE_{cell} from E_{cell}^{o} are denoted by P_d^{SS} and P_d^o in Table 4, respectively. It can be seen from Table 4. that P_d^o decreases with the increase in anode pressure whereas for increase in RH_a the power density shows an increase. Although the variation of power density for other operating parameters is not visible from Table 4, it is to be noted that with the increase in operating values for anode stoichiometry, cathode pressure and cathode relative humidity, power density increases whereas the power density decreases for increase in cathode stoichiometry.

It was seen from Fig. 3–9 that the fuel cell transients, and the time taken to reach steady state, are a strong function of water transport process, which in turn in is strongly correlated to the operating conditions. Undershoots and overshoots in the current are observed for the step change in voltage owing to the different time scales associated with the transport process. The results presented in this article offer insight into the effects of various operating conditions on the dynamic behavior of the fuel cell system for specified load changes. The effects of load changes on the mechanical behavior of membrane are also significant, as presented in Ref. [40,41]. Future work could include a two-phase model to account for higher values of cathode relative humidity, which was not the focus of current study. The effects of membrane properties can be studied to provide better insight into controlling the transient behavior. Also, an optimization of the fuel cell parameters as shown in Ref. [42] can be conducted with the transient model, in contrast to the traditional use to steady state models. The current framework is computationally expensive and could be simplified using network models to enhance the computational speed, to be used in control and optimization algorithms. The current study is limited to co-flow operations only. The effects of counter-flow operation could be analyzed as it would significantly affect the water distribution and thus the transient behavior. These aspects will be examined in a future study.

2.4 Nomenclature

a water activity or effective catalyst area per unit volume [m^2/m^3]

A superficial electrode area [m^2]

C_k molar concentration of species k [mol/ m^3]

D mass diffusivity of species[m^2/ s]

E_{cell} cell potential or voltage [V]

EW equivalent weight of dry membrane [kg/ mol]

F Faraday Constant [96,487 C/ equivalent]

I current density [A/ m^2]

j transfer current [A/ m^3]

K permeability [m^2]

n_d electro-osmotic drag coefficient [H_2O/ H^+]

p pressure [bar]

R gas constant [8.314 J/ mol K]

RH relative humidity [%]

S source term in transport equations

t time [s]

T temperature [K]

$\vec{u}$ velocity vector

Greek letters

α transfer coefficient

ε porosity

η surface overpotential [V]

λ membrane water content

μ viscosity [kg/ m s]

ζ stoichiometric flow ratio

ρ density [kg/ m^3]

σ electronic conductivity [S/ m]

τ shear stress [N/ m^2]; time constant; tortuosity

ϕ phase potential [V]

Superscripts and subscripts

a anode

c cathode

$cell$	single fuel cell
e	electrolyte
eff	effective value
g	gas phase
in	inlet
k	species
m	membrane phase
o	t = 0 s, initial state
ref	reference value
s	electronic phase
sat	saturated value
SS	steady state
t	time > 0 s
w	water

References

[1] Wang CY. Fundamental Models for Fuel Cell Engineering, Chem Rev 2004; 104(10): 4727–4766.

[2] Perry ML, Fuller TF, A Historical Perspective of Fuel Cell Technology in the 20th Century, J. Electrochem Soc, 2002; 149(7),S59–S67.

[3] Bernardi, DM., & Verbrugge, MW, A Mathematical Model of the Solid-Polymer Electrolyte Fuel Cell. *Journal of the Electrochemical Society* 1992; 139(9): 2477-2491.

[4] Um S, Wang CY, Chen K S, Computational fluid dynamics modeling of proton exchange membrane fuel cells. *Journal of the Electrochemical society* 2000; 147(12): 4485-4493.

[5] Zhang Y, Pitchumani R, Numerical studies on an air-breathing proton exchange membrane (PEM) fuel cell. *International Journal of Heat and Mass Transfer* 2007, 50(23), 4698-4712.

[6] Meng H, Wang, CY, Electron transport in PEFCs, *Journal of the Electrochemical Society* 2004; 151(3): A358-A367.

[7] Um S, Wang CY, Three-dimensional analysis of transport and electrochemical reactions in polymer electrolyte fuel cells; *Journal of Power Sources* 2004; 125(1): 40-51.

[8] Mawardi A, Yang F, Pitchumani R, Optimization of the operating parameters of a proton exchange membrane fuel cell for maximum power density. *Journal of Fuel Cell Science and Technology* 2005; 2(2): 121-135.

[9] Van Nguyen T, Knobbe MW, A liquid water management strategy for PEM fuel cell stacks. *Journal of Power Sources* 2003; 114(1): 70-79.

[10] Sinha, PK, Wang CY, Beuscher U, Transport phenomena in elevated temperature PEM fuel cells. *Journal of The Electrochemical Society* 2007; 154(1): B106-B116.

[11] Choi KH, Peck DH, Kim CS, Shin DR, Lee TH, Water transport in polymer membranes for PEMFC. *Journal of Power Sources* 2000; 86(1): 197-201.

[12] Janssen GJM, A phenomenological model of water transport in a proton exchange membrane fuel cell. *Journal of the Electrochemical Society* 2001; 148(12), A1313-A1323.

[13] Williams MV, Kunz HR, Fenton JM, Operation of Nafion® based PEM fuel cells with no external humidification: influence of operating conditions and gas diffusion layers. *Journal of Power Sources* 2004; 135(1): 122-134.

[14] Amphlett JC, Mann RF, Peppley BA, Roberge PR, Rodrigues A, A model predicting transient responses of proton exchange membrane fuel cells. *Journal of Power Sources* 1996; 61(1): 183-188.

[15] Pathapati PR, Xue X, Tang J, A new dynamic model for predicting transient phenomena in a PEM fuel cell system. *Renewable energy* 2005; 30(1): 1-22.

[16] Ceraolo M, Miulli C, Pozio A, Modelling static and dynamic behaviour of proton exchange membrane fuel cells on the basis of electro-chemical description. *Journal of power sources* 2003; 113(1): 131-144.

[17] Xue X, Tang J, Smirnova A, England R, Sammes N, System level lumped-parameter dynamic modeling of PEM fuel cell. *Journal of Power Sources* 2004; 133(2): 188-204.

[18] Wang Y, Wang CY, Transient analysis of polymer electrolyte fuel cells, *Electrochimica Acta* 2005, 50(6): 1307-1315.

[19] Wang Y, Wang CY, Dynamics of polymer electrolyte fuel cells undergoing load changes. *Electrochimica Acta* 2006, 51(19): 3924-3933.

[20] Shimpalee S, Spuckler D, Van Zee JW, Prediction of transient response for a 25-cm^2 PEM fuel cell. *Journal of power sources* 2007, 167(1): 130-138.

[21] Zou J, Peng XF, Yan WM, Dynamic analysis of gas transport in cathode side of PEM fuel cell with interdigitated flow field. *Journal of power sources* 2006; 159(1): 514-523.

[22] Peng J, Shin JY, Song TW, Transient response of high temperature PEM fuel cell. *Journal of Power Sources* 2008; 179(1): 220-231.

[23] Qu S, Li X, Ke C, Shao ZG, Yi B, Experimental and modeling study on water dynamic transport of the proton exchange membrane fuel cell under transient air flow and load change. *Journal of Power Sources*, 195(19), 6629-6636.

[24] Shah AA, Kim GS, Sui PC, Harvey D, Transient non-isothermal model of a polymer electrolyte fuel cell. *Journal of Power Sources* 2007, 163(2), 793-806.

[25] Dokkar B, Settou NE, Imine O, Saifi N, Negrou B, Nemouchi Z, Simulation of species transport and water management in PEM fuel cells. *International journal of hydrogen energy* 2011, 36(6), 4220-4227.

[26] Cho J, Oh H, Park J, Min K, Lee E, Jyoung JY, Effect of the micro porous layer design on the dynamic performance of a proton exchange membrane fuel cell. *International Journal of Hydrogen Energy* 2014, 39(1), 459-468.

[27] Gomez A, Raj A, Sasmito AP, Shamim T, Effect of operating parameters on the transient performance of a polymer electrolyte membrane fuel cell stack with a dead-end anode. *Applied Energy* 2014.

[28] Song GH, Meng H, Numerical modeling and simulation of PEM fuel cells: Progress and perspective. *Acta Mechanica Sinica* 2013; 29(3): 318-334.

[29] Wang Y, Chen KS, Cho SC, PEM Fuel Cells: Thermal and Water Management Fundamentals, Sustainable Energy 2013, Momentum Press.

[30] Wang Y, Wang CY, Two-phase transients of polymer electrolyte fuel cells, *Journal of The Electrochemical Society* 2007; 154(7): B636-B643.

[31] Wang Y, Chen KS, Elucidating two-phase transport in a polymer electrolyte fuel cell, Part 1: characterizing flow regimes with a dimensionless group, *Chemical Engineering Science* 2011; 66: 3557-3567.

[32] Hu M, Gu A, Wang M, Zhu X, Yu L, Three dimensional, two phase flow mathematical model for PEM fuel cell: Part I. Model development. *Energy Conversion and Management* 2004; 45(11): 1861-1882.

[33] Wang Y, Basu S, Wang CY, Modeling Two-Phase Flow in PEM Fuel Cell Channels, Journal of Power Sources 2008; 179**:** 603-617.

[34] Promislow K, Chang P, Haas H, Wetton B, Two-phase unit cell model for slow transients in polymer electrolyte membrane fuel cells, *Journal of The Electrochemical Society* 2008; 155(7): A494-A504.

[35] Verma A, and Pitchumani R, Influence of Membrane Properties on the Transient Behavior of Polymer Electrolyte Fuel Cells, *Journal of Power Sources* 2014; 268: 733-743.

[36] Bird R B, Stewart WE, Lightfoot EN, *Transport phenomena* 2007. John Wiley & Sons.

[37] Springer TE, Zawodzinski TA, Gottesfeld S, Polymer electrolyte fuel cell model. *Journal of the Electrochemical Society* 1991; 138(8): 2334-2342.

[38] Zawodzinski TA, Springer TE, Uribe F, Gottesfeld S, Characterization of polymer electrolytes for fuel cell applications. *Solid state ionics* 1993; *60*(1): 199-211.

[39] Slade S, Campbell SA, Ralph TR, Walsh FC, Ionic conductivity of an extruded Nafion 1100 EW series of membranes, *Journal of The Electrochemical Society* 2002, *149*(12), A1556-A1564.

[40] Verma A, Pitchumani R, Investigation of Mechanical Behavior of Membrane in Polymer Electrolyte Fuel Cells Subject to Dynamic Load Changes, *Journal of Fuel Cell Science and Technology* 2014; *11*(3): 031009.

[41] Verma A, Pitchumani R, Influence of Transient Operating Parameters on the Mechanical Behavior of Fuel Cells, *Journal of Power Sources* 2014, In Review

[42] Verma A, Pitchumani R, Analysis and Optimization of Transient Response of Polymer Electrolyte Membrane Fuel Cells, *Journal of Fuel Cell Science and Technology* 2014; Accepted for publication.

Table 2.1: Source terms in the governing equations

Domain	S_V	S_i	S_s, S_m
Gas channels	0	0	0
Diffusion layers	$-\frac{\mu}{K_{GDL}}\vec{u}$	0	0
Catalyst layers	$-\frac{\mu}{K_{GDL}}\vec{u}$	Anode	Anode
		$-\frac{j_a}{2F}$ $(i = H_2)$	$S_s = -j_a < 0$
		0 $(i = O_2)$	$S_m = +j_a < 0$
		$-\nabla.\left(\frac{n_d i_e}{F}\right)$ $(i = H_2O)$	
		Cathode	Cathode
		0 $(i = H_2)$	$S_s = +j_c > 0$
		$-\frac{j_c}{4F}$ $(i = O_2)$	$S_m = -j_c < 0$
		$\frac{j_c}{2F} - \nabla.\left(\frac{n_d i_e}{F}\right)$ $(i = H_2O)$	
Membrane	$-\frac{\mu}{K_{GDL}}\vec{u}$	0	0

Table 2.2: Geometrical and physical parameters used in the numerical simulations [5,18]

Parameter [units]	Symbol	Value
Gas channel depth [mm]		1.0
Diffusion layer thickness [mm]		0.3
Catalyst layer thickness [mm]		0.01
Membrane (N112) thickness [mm]		0.051
Fuel cell/ Gas channel length [mm]		100.0
Temperature [K]	T	353
Permeability of diffusion layer [m^2]	K_{GDL}	10^{-12}
Permeability of catalyst layer [m^2]	K_{CL}	10^{-15}
Gas diffusion layer porosity	ε_{GDL}	0.6
Catalyst layer porosity	ε_{CL}	0.4
Volume fraction membrane in catalyst layer	ε_m	0.26
Anode reference exchange current density [A/ m^3]	$j_{a,ref}$	5.00×10^{8}
Cathode reference exchange current density [A/ m^3]	$j_{c,ref}$	500
H_2 diffusivity membrane [m^2/ s]	$D_{H_2,mem}$	2.59×10^{-10}
H_2 diffusivity in gas [m^2/ s]	$D_{H_2,ref}$	1.1×10^{-4}
O_2 diffusivity in membrane [m^2/ s]	$D_{O_2,mem}$	8.328×10^{-10}
O_2 diffusivity in gas [m^2/ s]	$D_{O_2,ref}$	3.2348×10^{-5}
H_2O diffusivity in gas [m^2/ s]	$D_{H_2O,ref}$	7.35×10^{-5}

Table 2.3: Base values and ranges considered in the parametric studies

Parameter	Base Value	Range Studied
T [K]	353	constant
p_a [bar]	2.0	$1.5 \le p_a \le 7.0$
ζ_a	2.0	$1.0 \le \zeta_a \le 3.0$
RH_a [%]	100	$50 \le RH_a \le 100$
p_c [bar]	2.0	$1.5 \le p_c \le 4.0$
ζ_c	2.0	$1.5 \le \zeta_c \le 3.0$
RH_c [%]	0%	$0 \le RH_c \le 75$

Table 2.4: Power density corresponding to the voltage change and optimum parameters in Figs. 8 and 9

Parameter	E^o_{cell} [V]	ΔE_{cell} [V]	Optimum Parameter Value	P^o_d [W/cm^2]	P^{SS}_d [W/cm^2]	E^o_{cell} [V]	ΔE_{cell} [V]	Optimum Parameter Value	P^o_d [W/cm^2]	P^{SS}_d [W/cm^2]
Anode Pressure [bar]	0.50 V	0.10	4.5	0.247	0.170	0.70	-0.20	4.5	0.090	0.247
		0.15	4.2	0.255	0.133		-0.10	3.1	0.101	0.191
		0.20	3.1	0.295	0.101		-0.05	3.0	0.101	0.146
		0.30	2.9	0.305	0.035		0.10	2.2	0.106	0.035
Anode Stoichio-metry	0.50 V	0.10	1.0	0.279	0.186	0.70	-0.20	1.0	0.098	0.279
		0.15	1.0	0.279	0.141		-0.10	1.0	0.098	0.186
		0.20	1.0	0.279	0.098		-0.05	1.0	0.098	0.141
		0.30	1.0	0.279	0.035		0.10	1.0	0.098	0.035
RH at Anode Inlet [%]	0.50 V	0.10	64.6	0.277	0.183	0.70	-0.20	57.6	0.091	0.255
		0.15	68.2	0.283	0.142		-0.10	80.9	0.102	0.198
		0.20	81.6	0.319	0.102		-0.05	81.6	0.102	0.149
		0.30	81.6	0.319	0.034		0.10	83.0	0.104	0.362
Cathode Pressure [bar]	0.50 V	0.10	1.5	0.293	0.196	0.70	-0.20	1.5	0.106	0.293
		0.15	1.5	0.293	0.153		-0.10	1.5	0.106	0.196
		0.20	1.5	0.293	0.106		-0.05	1.5	0.106	0.153
		0.30	1.5	0.293	0.038		0.10	1.5	0.106	0.038
Cathode Stoichio-metry	0.50 V	0.10	3.0	0.287	0.198	0.70	-0.20	3.0	0.102	0.287
		0.15	3.0	0.287	0.147		-0.10	3.0	0.102	0.198
		0.20	3.0	0.287	0.102		-0.05	3.0	0.102	0.147
		0.30	3.0	0.287	0.035		0.10	3.0	0.102	0.035
RH at Cathode Inlet [%]	0.50 V	0.10	0.0	0.383	0.225	0.70	-0.20	75.0	0.211	0.799
		0.15	0.0	0.383	0.163		-0.10	0.0	0.110	0.225
		0.20	0.0	0.383	0.110		-0.05	0.0	0.110	0.163
		0.30	0.0	0.383	0.034		0.10	0.0	0.110	0.034

Chapter 3: Analysis and Optimization of Transient Response of Polymer Electrolyte Fuel Cells

This chapter focuses on elucidating the transient response of a PEM fuel cell for specified changes in operating parameters namely voltage, pressure and stoichiometry at the cathode and the anode. Transient numerical simulations are carried out for a single-channel PEM fuel cell to illustrate the response of power as the operating parameters are subjected to specified changes. These parameters are also optimized with an objective to match the power requirements of a automotive drive cycle over a certain period of time.

3.1 Introduction

Owing to different time scales of transport mechanisms in the transient process, change in operating conditions present a complex interaction between dynamic behavior and transport process. The operating parameters affect the rate at which reactants are supplied to catalyst layer thus determining the performance. Also operating conditions affect the amount of water stored in membrane which in turns affects the performance of fuel cell. Transient operation of fuel cells requires the operating parameters to be controlled dynamically to meet the power requirements subject to change in loads. Understanding the transient behavior and effect of dynamically changing operating parameters is of paramount importance for PEM fuel cells to be successfully deployed for mobile applications [1-5].

Several researchers have studied the effect of operating parameters on PEM fuel cell behavior numerically and experimentally. Wang et al. [6] experimentally investigated the effect of various operating parameters on polarization curve highlighting the interrelationship between observed behavior and transport mechanisms. Zhang et al. [7] performed numerical studies to investigate the effects of porosity, permeability, thickness of GDL and stoichiometric flow ratio on steady-state performance of fuel cell and optimized the parameters for higher interface potential. Mawardi et al. [8,9] used a one-dimensional model to optimize operating parameters with the objective to maximize power density subject to constraints and study the effects of parameter uncertainty on the performance variability. Yan et al. [10] concentrated on the steady-state performance and transient response in both single fuel cell and stack configurations for varying loading cycles and range of operating conditions. Zhang et al. [11]

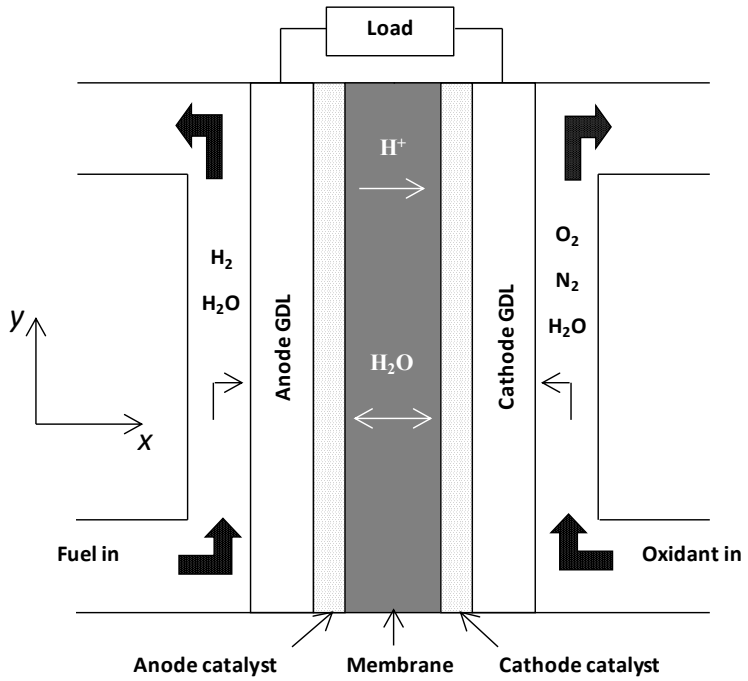

Figure 3.1: Schematic of PEM fuel cell

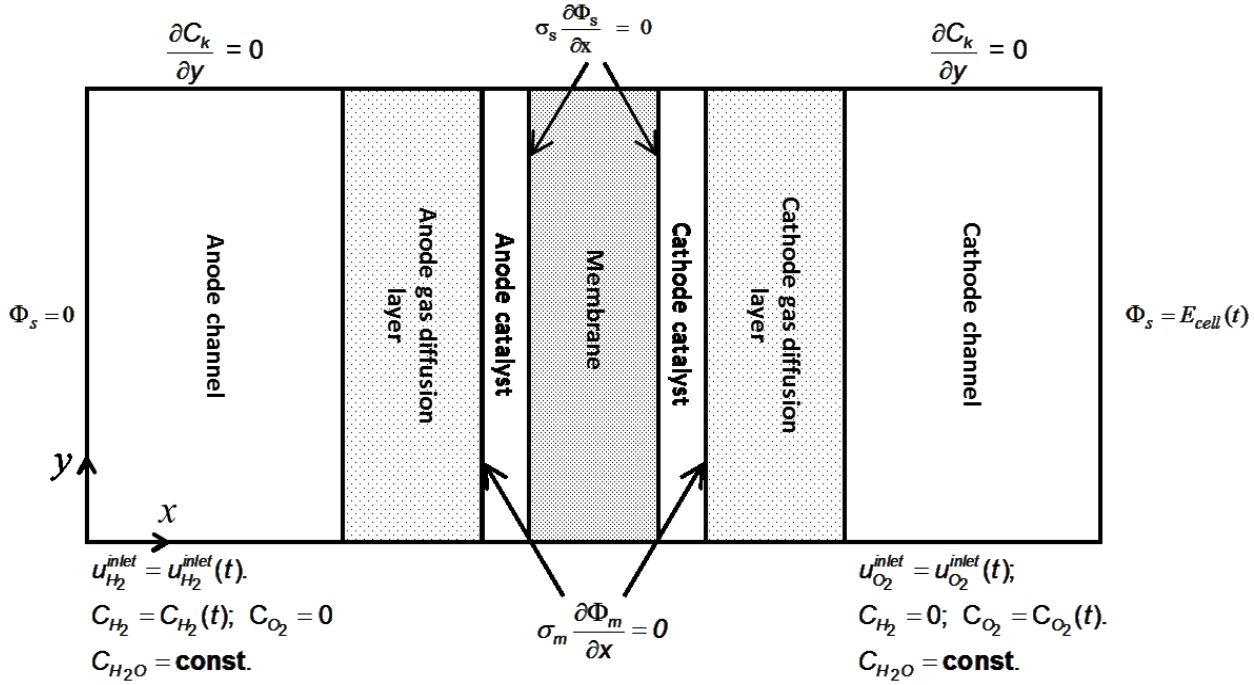

Figure 3.2: Schematic of model domain and associated boundary conditions.

numerically studied the effects of operating parameters on the variation of local current density and developed design windows maximizing current density. An operation-relevant one dimensional model was developed Hung et al. [12] developed to elucidate the effects of

operating parameters on cell performance. Design and modeling parameters were obtained via regression of experimental data and validated for changing operating parameters. Amirinejad et al. [13] experimentally investigated the variations in cell performance by using dry and humidified hydrogen and oxygen for various operating conditions. Previous numerical studies used simplified steady state models and lacked detail representation of complex interactions during transient operations. The model by Um et al. [14] assumed constant water content and investigated the transient response of fuel cell, emphasizing the effects of reactant diffusion. Wang and Wang [4,5], extending the model used in Ref. [14] to include the effects of water accumulation and electrochemical double layer discharge. The transient model explored the dynamic behavior for step change in humidity, voltage and current, emphasizing the different time scales characteristic to transport and electrochemical process. Yuan et al. [15] used a three-dimensional computational fluid dynamics (CFD) model to study the effects of operating parameters on the fuel cell performance indicating that the best performance occurs at moderate air relative humidity while the hydrogen is fully humidified. In our previous work [16] the effects of membrane properties on transient behavior was studied for dry operating conditions focusing on water transport.

In the present study, computational fluid dynamics simulations are carried out using the model developed in Ref. [4] to study the effect of cyclic changes in operating parameters on the power density of a single channel PEM fuel cell. The fuel cell system is subjected to cyclic variations in the operating parameters, to elucidate the transient response of the system power density. Optimum operating parameters are then determined with the objective of matching the power requirements of the US06 drive cycle [14]. The article is organized as follows: the two dimensional transient model for PEM fuel cell is described in the next section, followed by results and discussion of parametric *study* and optimization of the operating parameters.

3.2 Mathematical Model

The mathematical used in the study is similar to that described in Section 2.2 and has been omitted for brevity.

3.2.1 Periodic variations in operating parameters

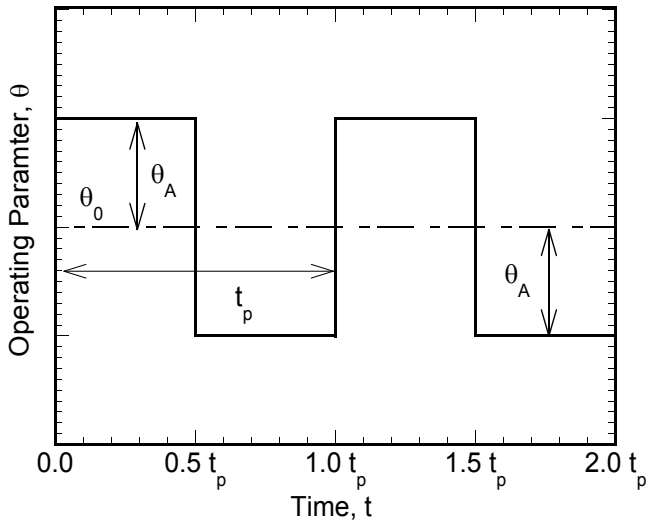

Figure 3.3: Profile of cyclic variation in operating parameter as a function of time.

The single channel fuel cell system as depicted in Sec. 2.1 is subject to periodic variations in operating parameters namely cell voltage (E_{cell}), anode and cathode pressure (p_a and p_c, respectively) and anode and cathode stoichiometry (ζ_a and ζ_c, respectively). The fuel cell system is subject to periodic variations as described below:

$$\theta(t) = \begin{cases} \theta_0 - \theta_A & 0 \le \frac{t}{nt_p} < \frac{1}{2} \\ \theta_0 + \theta_A & \frac{1}{2} \le \frac{t}{nt_p} < 1 \end{cases} \quad n = 1, 2, 3 \ldots\ldots N \tag{12}$$

where θ represents the parameters, namely E_{cell}, p_a, p_c, ζ_a and ζ_c, $\theta(t)$ represents the instantaneous value of θ at any given time t, θ_0 is the mean and θ_A is the amplitude of variation and are tabulated in Table 2, and, t_p is the time period of variation.

3.2.2 Numerical Solution Procedure

The governing equations along with the boundary conditions subject to the periodic variations were solved using a control volume based commercial fluid dynamics (CFD) package, Fluent®, with the pressure-implicit with splitting of operators (PISO) algorithm. The specific governing equations and the corresponding source terms were implemented through user-defined functions and user-defined scalars (species and phase potentials). An 80 (across the cell) × 40 (along the channel) grid was found to be optimum in terms of accuracy and computational time, with the solution, for a particular time step, converging as the residuals reduce to 10^{-6} for all the equations. The geometrical, physical and electrochemical parameters

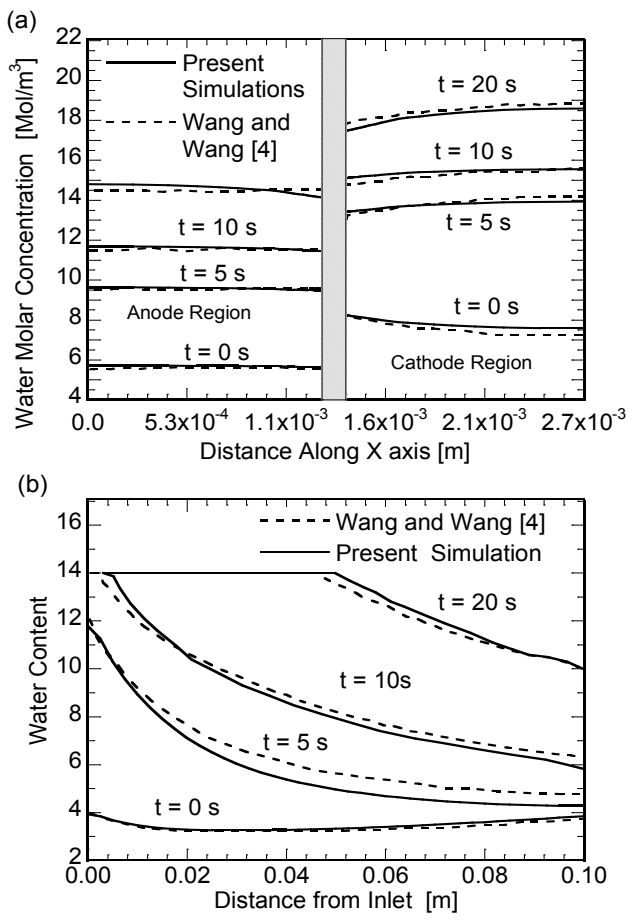

Figure 3.4: Validation of the numerical model with results from Wang and Wang [4]

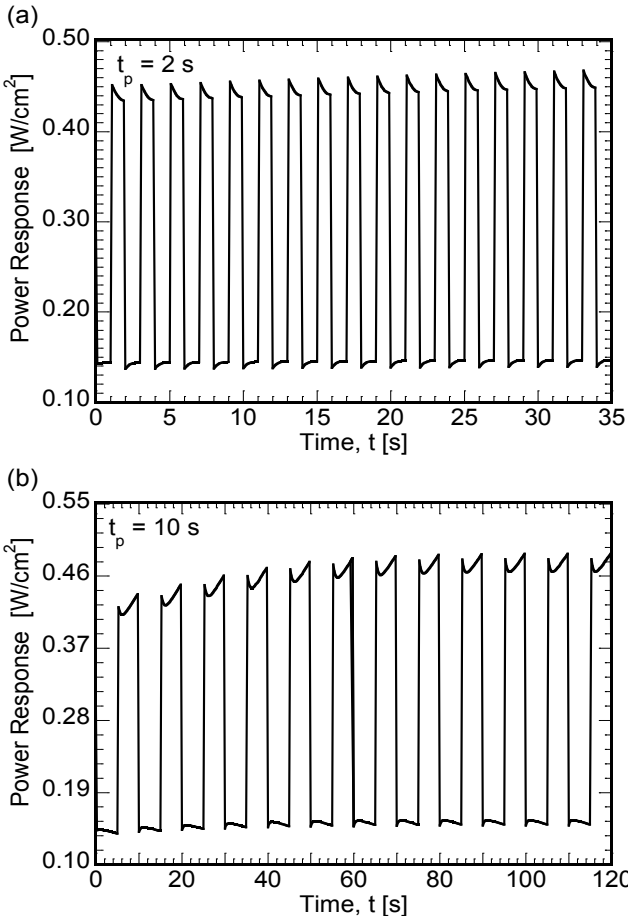

Figure 3.5: Variation in power density as a function of time, for cyclic variation in cell voltage for (a) t_p = 2 s and (b) t_p = 10 s

used in this study are listed in Table 3. A constant time step of 0.1 s is used for the simulations; with a run time of approximately 4 hours on an Intel® 3.33 GHz Xeon™ Processor. A load change is imposed at the initial time, t = 0, by specifying the cyclic change in the operating parameters, as a boundary condition. The operating parameters are subjected to cyclic variation, as illustrated schematically in Fig. 3 for any generic operating parameter, θ, and the cell power response is studied to elucidate the transient fuel cell behavior.

3.3 Results and Discussion

The numerical model discussed previously was validated with the work done by Wang and Wang [4], as presented in Fig. 4. The results of the present model are represented by solid lines, while those from Ref. [4] are shown as dashed lines. Figure 4(a) presents the evolution of water concentration profiles across the anode and cathode channel thickness with time, when the inlet

humidification at the cathode inlet (RH_c) changes from 0% to 100%, at a cell voltage of 0.65 V. Initially, at t = 0, the cathode gas channel is relatively dry and the concentration gradient is such that water generated at cathode catalyst layer due to oxidation-reduction reaction is removed through the gas channel. When humidity at the cathode inlet changes instantly to the fully humidified state, the concentration front changes, altering the concentration gradient, such that the membrane not only gets hydrated by the generated water but from the humidified gas channel. As the membrane gets hydrated, the current density increases due to increased proton conductivity of membrane, increasing the water production, further altering the water concentration profile. Also, the water concentration profile at anode side is altered by the back diffusion of water through membrane. Figure 4(b) shows the membrane water content variation along the length of the fuel cell at the mid section of the membrane (x = 1.3355×10^{-4} m), when cathode inlet relative humidity changes from 0% to 100% at 0.65 V. The water content reaches steady state first at inlet within 10 s, while it takes more than 20 s for the outlet to reach steady state. The results from the present model are seen to be in close agreement with those reported in Ref. [4], demonstrating the ability of the model to capture the transients accurately.

Figures 5(a) and (b) present the temporal variation in power density as the cell voltage is cyclically varied around 0.60 V with an amplitude of 0.10 V for time period, t_p, of 2 s and 10 s, respectively. A drop in the current density, leading to drop in power density is observed as the voltage changes from 0.60 to 0.70 V at t = 0 (Fig. 5(a)). The quick response to the change in voltage is attributed to the time scale associated with double-layer discharge, which is on the order of microseconds. Operation at lower voltage or high current density, causes the reactants, H_2 at the anode and O_2 at the cathode, to deplete locally. As a result, when the voltage is changed suddenly, it causes the power to drop first and then increase as the sites are replenished with diffusion of reactants from the feed streams. A step increase in voltage leads to lower power density and, in turn, reduced production of water, increasing the resistance for proton transport through membrane. Therefore, decrease in power is observed after a slight increase when the reactants are replenished and can be seen as small hump at first half time period ($t < 0.5t_p$) in Fig. 5(a). For t > 1 s, as the voltage drops to 0.50 V, it leads to increase in power density, which is followed by a drop as the reactants deplete locally and then further increase as the membrane is rehydrated by back-diffusion. Since the time scale associated with

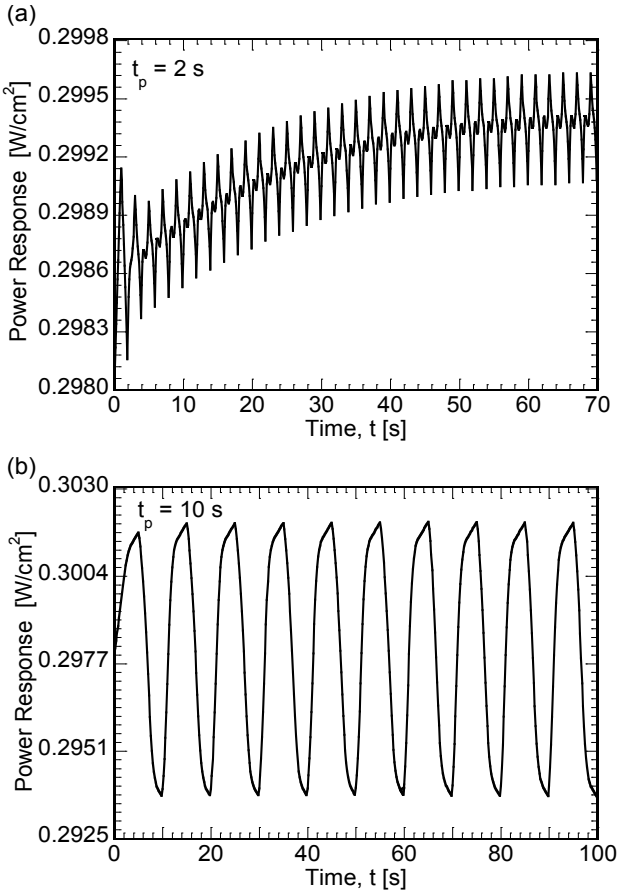

Figure 3.6: Variation in power density as a function of time, for cyclic variation in anode pressure for (a) t_p = 2 s and (b) t_p = 10 s.

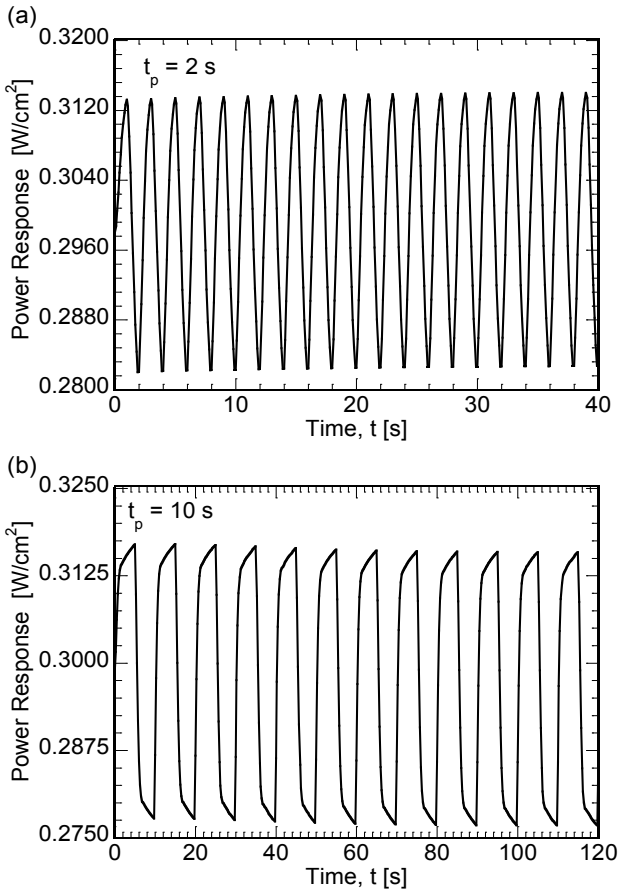

Figure 3.7: **Variation in power density as a function of time, for cyclic variation in cathode pressure for (a) t_p = 2 s and (b) t_p = 10 s.**

the hydration/ dehydration for the system to reach steady-state is on the order of order 10 s, which is much higher compared to the diffusion time scale, which is on the order of microseconds, the effects of hydration are not significant for the shorter time periods. On the other hand, in Fig. 5(b) where the time period for the variations is 10 s, the effect of hydration are more clearly visible and are depicted by the considerable increase in power after the initial dip for $5 < t < 10$ s and other similar intervals. It can be seen in Fig. 5(b) that after the sudden decrease in voltage from 0.60 to 0.50 V in all the cycles, $t > 0.5\ t_p$, the peak power density increases with the number of cycles, reaching a steady state at a later stage. It is also seen from Figs. 5(a) and (b) that the average power density for t_p = 2 and 10 s increases with the number of cycles reaching a steady state at different stages.

Figure 6 shows the response of power density for cyclic variations of anode pressure. The mean pressure is 4 bar and the amplitude of variation is 1 bar, thus cycling the anode pressure between 3 and 5 bar as per the square periodic profile shown in Fig. 3, with the other parameters fixed at their nominal values. The increase in anode pressure is numerically realized by increasing the effective H_2 concentration at the inlet boundary. Figure 6(a) shows that for t_p = 2 s, there is a jump in power density with increase in the anode pressure from 4 to 5 bar. This can be attributed to increase in the concentration of H_2 with increase in pressure, followed by the decrease in the current density for $t > 0.5t_p$, as the concentration decreases with decrease in pressure. It can be seen in Fig. 6(a) that for the first cycle, the jump in power density is higher compared to what is observed in the following cycles. This can be attributed to relatively higher local concentration of reactants, in this case H_2 at the anode and O_2 at cathode side, during the first half of first cycle; however, as the concentration cycles, the average decreases leading to a decrease in the jump. Also, there is an increasing trend in the average power with the cycles further reaching a steady state; this can be attributed to increasing water content with cycles, which is due to higher current density. Interestingly, this is not the case when the time period, t_p, is increased from 2 s to 10 s in Fig 6(b) where the change in average power density is relatively insignificant compared to that observed in Fig. 6(a). As more time is given for the fuel cell system to react to the step changes, the effect of changes in concentration is realized all through the length and thus, the system behavior is similar for consecutive cycles, with slight increase in average power density due to increase in the average hydration values over the cycles, owing to faster hydration and slower dehydration.

Figure 7 depicts the temporal variation in power density for cyclic variations (Fig. 3) of cathode pressure. The mean pressure is 4 bar and amplitude of variations is 1 bar, thus cycling cathode pressure between 3 and 5 bar, with other parameters fixed. The increase in cathode pressure is numerically realized by increasing the effective O_2 concentration at inlet boundary at cathode. It can be seen in Fig. 7(a) that even though the pressure jump is instantaneous, the power density changes gradually, as compared to that observed in Fig. 5(a) for voltage change. This can be attributed to the time scale associated with the transport of reactants, which is orders of magnitude higher than the time scale associated with double layer discharge. It is also noted that the variation in power density exhibits similar behavior around increasing mean for consecutive cycles, in contrast to the observed changes for anode pressure (Fig. 6(a)) where the

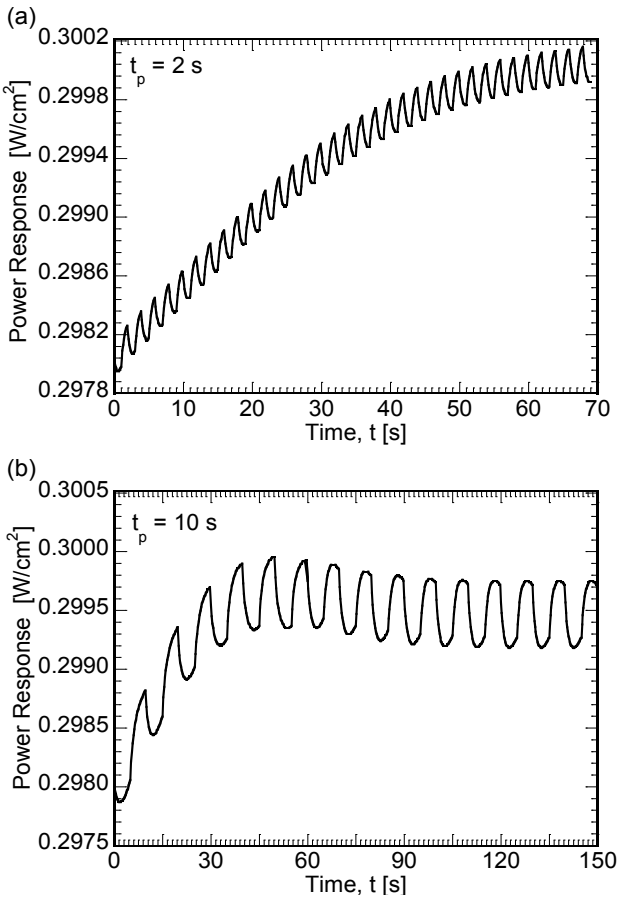

Figure 3.8: Variation in power density as a function of time, for cyclic variation in anode inlet velocity for (a) t_p = 2 s and (b) t_p = 10 s.

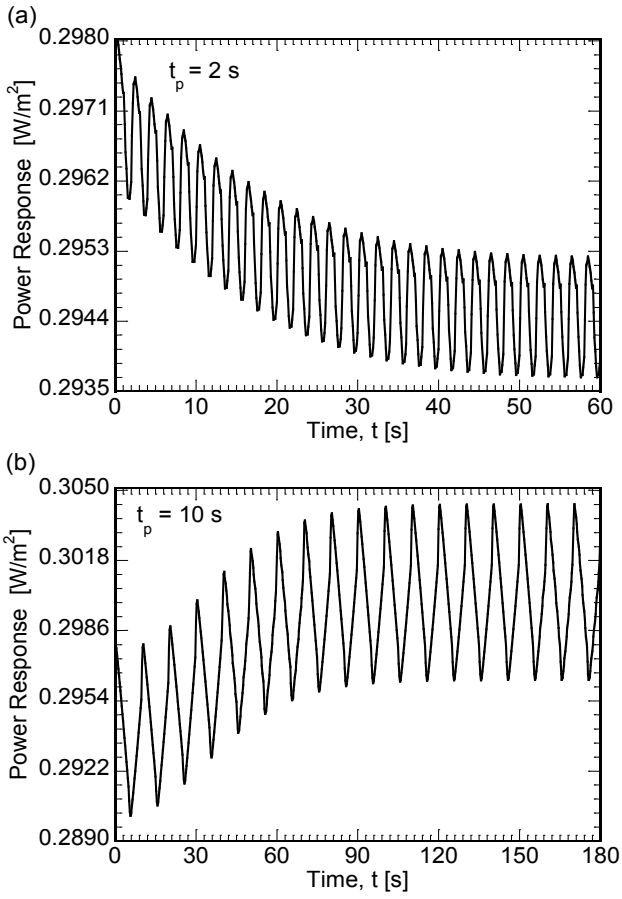

Figure 3.9: Variation in power density as a function of time, for cyclic variation in cathode inlet velocity for (a) t_p = 2 s and (b) t_p = 10 s.

peak for 1st cycle was seen to be relatively higher in comparison to the consecutive cycles. It is also noted that the average power density increases with the increase in the number of cycles as seen in Fig. 7(a). Unlike the observation in Fig. 7(a), for t_p = 10 s (in Fig. 7(b)) , a steeper change for power profile is observed at first, followed by gradual change, as seen in Fig. 7(b). This can be attributed to the dominant effect of species diffusion at first followed by the effects of water back diffusion. In comparison to that observed for Fig. 7(a) the average power density decreases with the number of cycles for t_p = 10 s as seen in Fig. 7(b).

Figure 8 shows the variation in power density for cyclic variations in anode stoichiometry. The anode pressure is fixed and the velocity is cycled leading to change in stoichiometry. The mean velocity is 0.1026 m/ s and amplitude of variations is 0.03078 m/ s, which is 20% of the mean value, thus cycling anode velocity between 0.07182 and 0.13338 m/ s, with the other

parameters fixed to mean values in Table 2. Figure 8(a) shows the variations for t_p = 2 s, it can be seen that the average power density increases with progressive cycles reaching a steady state for t > 60 s, although the velocity is cycled around fixed mean value. This can be primarily attributed to increase availability of H_2 and H_2O along the length of the fuel cell over cycles. In contrast to Fig. 6(a), increase in anode velocity leads to decrease in power density, which is recovered over time. This behavior can be attributed to the change in rate of water removal through anode. Fig. 8(b) shows the variation in power density for t_p = 10 s. It can be seen that the amplitude of power density variation is larger compared to that observed in Fig. 8(a) owing to the time available to the fuel cell system to react to changes in velocity. The power density shows an increasing trend with consecutive cycles for step decrease reaching a peak for 6^{th} cycle before reaching a steady state for t > 90 s.

Figure 9 depicts the variation in power density for cyclic variations in cathode flow rate. The value of cathode pressure is fixed and cathode inlet velocity is varied, cycling the cathode stoichiometry. The cathode inlet velocity is varied periodically between 0.16093 and 0.29887 m/ s, with 0.2299 m/ s as mean, while other parameters are fixed at a constant value and do not change with time. For t_p = 2 s, there is a lag in power response to changes in velocity, as seen in Fig. 9(a), and can be associated to the time scales of convective transport process. With the increase in cathode velocity, the rate at which water generated at cathode catalyst layer is transported out of the system also increases, leading to decrease in average water content and thus reduced power density. With the progressive cycles, the average water content reduces, leading to decrease in the average power density over the cycles. Figure 9(b) depicts the power density response for t_p = 10 s. Similar to that observed in Fig. 9(a), increase in velocity leads to decrease in the power density in Fig. 9(b). It is also noted that the average power density increases with consecutive cycles for t_p = 10 s (Fig. 9(b)) in contrast to decrease in average power density for t_p = 2 s (Fig. 9(a)). This behavior can be attributed to the fact that given more time for the effects of the changes in the cathode velocity to be realized there is an increase in membrane hydration over the cycles leading to increase in average power density reaching a steady state at a later stage.

3.4 Optimization

The results discussed before illustrate the effects of changes in operating parameters on transient fuel cell behavior. These parameters are further optimized, with an objective to match

power response of US06 drive cycle [14]. The goal of the optimization is to determine the optimum variation in operating parameters so as to closely track the power curve specified for US06 drive cycle [14] using only the fuel cell system as power source.

A model based optimization study is performed to elucidate the changes in operating parameters desired to supply the power for a specified time period of operation. The transient variation of operating parameters – cell voltage, anode and cathode operating pressures, and anode and cathode mass flow rates – forms the decision variables whose optimum values are sought in the problem such as to closely follow a given transient power profile. The decision variables are subjected to upper and lower bounds with no explicit constraints. The unconstrained optimization problem can be written mathematically as:

$$\underset{E_{cell},\, p_a,\, p_c,\, \dot{m}_a,\, \dot{m}_c}{\text{minimize}} \; (P_d - P_s) \cdot \zeta_{\mathrm{a}} \cdot \zeta_{\mathrm{c}}$$

where P_d is the desired power density variation with time, taken from Ref. [14], and P_s is the power obtained from numerical simulations, ζ_{a} and ζ_{c} are the stoichiometric ratio at anode and cathode side, respectively, p_a and p_c, represent the anode and cathode pressure, and $\dot{m}_a$, and $\dot{m}_c$ represent the mass flow rates at the anode and cathode side. The objective is to follow the desired power curve closely by minimizing the difference between simulated value and the desired power curve, at each time instant during the cycle while forcing the stoichiometry to be constrained for least fuel usage. The desired power profile is divided into smaller intervals ranging from 0.25 s to 2 s and optimized consecutively to satisfy the objective function. The decision variables $E_{cell}, p_a, p_c, \dot{m}_a$ and $\dot{m}_c$ are all functions of time, represented as piecewise linear variations over each of the smaller subintervals constituting the entire time considered. The optimized decision variables at the end of each smaller interval forms the initial point for the optimization in the following time subinterval.

The optimization problem is solved using the Nelder-Mead simplex method [15] combined with a simulated annealing technique to improve the effectiveness of the search [16,17]. The simplex search method is an algorithm that performs continuous search for selecting a new point during an optimization iteration, which guarantees objective function improvement. A simplex is defined as a convex hull of $N + 1$ vertices in an N-dimensional space, representing the N decision variables that govern the objective function evaluation. The vertices are ranked, from best to worst, based on the corresponding objective function evaluations and the best vertex is defined as the primary vertex. Since the primary vertex corresponds to a set of decision variables, which corresponds to the lowest objective function evaluation, the finding of a new

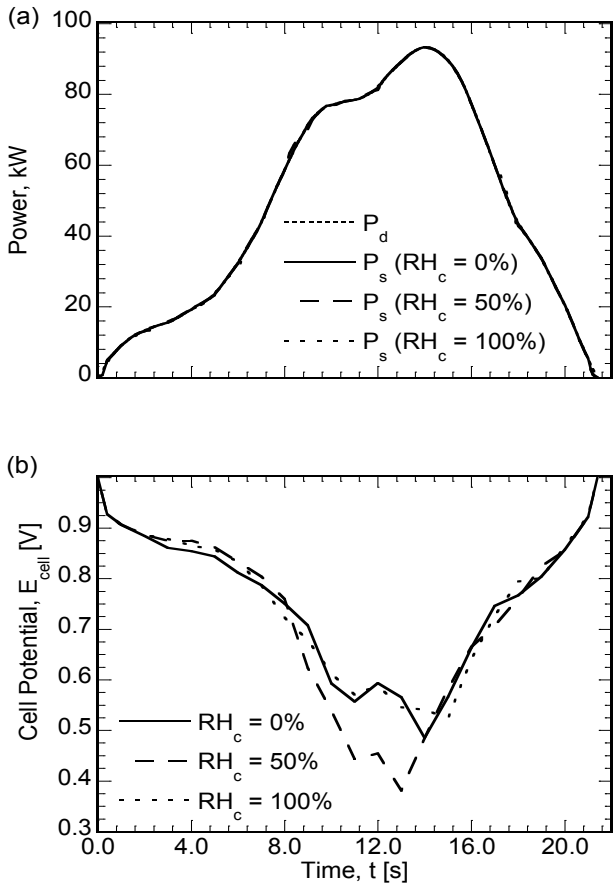

Figure 3.10: (a) Desired and simulated power curves for power curve C1, as a function of time and (b) optimized cell voltage for various cathode inlet humidity.

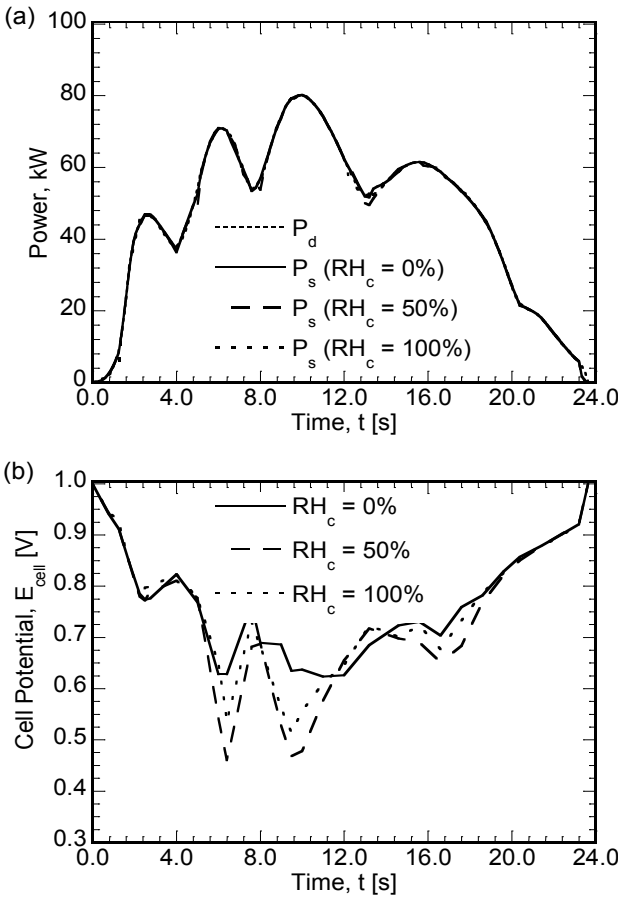

Figure 3.11: (a) Desired and simulated power curves for power curve C2, as a function of time and (b) optimized cell voltage for various cathode inlet humidity.

primary vertex constitutes an improvement to the objective function. The Nelder–Mead simplex method combined with simulated annealing is designed to solve non-linear unconstrained problems and is suitable for current problem. A one-dimensional form of the numerical model discussed previously is used for the optimization problem. This is achieved by considering a single cell along the length of the fuel cell. Three different power curves representing parts of US06 drive cycle [14] are used as objective curves to be tracked and are referenced by curve C1, C2 and C3.

Figure 10 present the results from the optimization studies for different values of cathode inlet relative humidity for tracking power curve C1. Figure 10(a) presents the desired power curve, P_d, shown as solid line, and simulated power curves in dashed styles for RH_c = 0%, 50% and 100%. It can be seen that the simulated power curves closely match the desired power curve

indicating that the current fuel cell setup satisfies the US06 drive cycle [14] power requirements. The drive cycle used here represents a fraction of the actual drive cycle, but presents significant characteristics of power variations. The power rises from 0 to maximum of 93 KW at around 14 s again reaching 0 at 21.4 s. The optimization was performed considering small intervals where the operating parameters varied linearly with time.

Figure 10(b) shows the temporal variation of optimized cell voltage corresponding to the simulated power curve in Fig. 10(a) for different relative humidity at cathode inlet. From Figs. 10(a) and (b), it can be observed that the cell voltage decreases as the power requirement increases from 0 to 14 s, and then increases as the power requirement decreases. On close observation, it can be found from Fig. 10(b) that the cell voltage reaches a minimum at different time instants for different RH_c values. This is attributed to the difference in the concentration of reactants at the cathode inlet and the water content values as a result of simultaneous variations in operating parameters. It is to be noted here that other operating parameters are also vary and are optimized to match the desired power curve in Fig. 10(b). The detailed variation of anode and cathode, pressure and mass flow rates are not shown due to indistinguishable patterns in the variations of the above parameters but the maximum value observed for the operating parameters and the corresponding time the maximum is observed is presented in Table 4. It was also noted from Figs 5–9 that variation in power density due to changes in voltage is significantly higher than that observed for changes in other operating parameters namely anode and cathode, pressure and stoichiometry. It can be seen from Table 4 that anode pressure assumes the maximum value of 3.36 and 3.86 bar for RH_c = 0% and 50 %, respectively, when the power reaches a maximum value at 13.0 s (Fig. 10(a)). Whereas for RH_c = 100% the maximum of 4.99 bar occurs at 16.0 s when the there is decrease power from the maximum power at t = 13.0 s. The maximum value of cathode pressure, p_c, for RH_c = 0%, 50% and 100 % are 4.51, 4.93 and 3.25 bar, respectively.

Similar to Fig. 10, Fig. 11 present the results from the optimization studies for different values of cathode inlet relative humidity for tracking power curve C2. It can be seen from Fig. 11(a) that the simulated power curves closely match the desired power curve indicating that the current fuel cell setup satisfies the US06 drive cycle [14] power requirements. The drive cycle

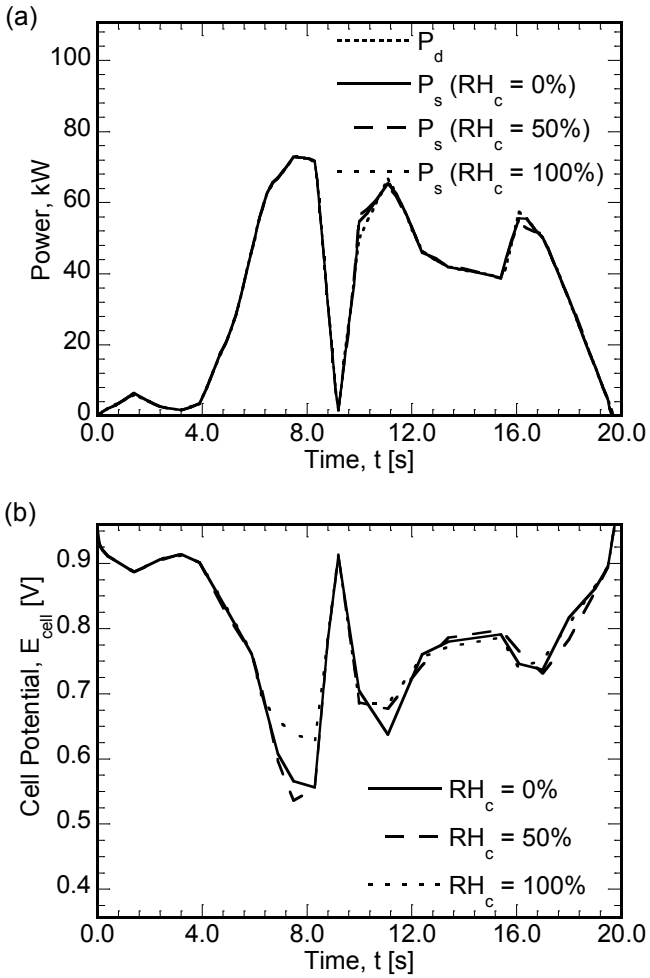

Figure 3.12: (a) Desired and simulated power curves for power curve C2, as a function of time and (b) optimized cell voltage for various cathode inlet humidity.

used here represents a fraction of the actual drive cycle, but presents significant characteristics of power variations. The power rises from 0 to maximum of 80 kW at around 12 s again reaching 0 at 23.6 s. Figure 11(a) shows distinct characteristics of a drive cycle with four peaks at different times. Figure 11(b) shows the temporal variation of optimized cell voltage corresponding to the simulated power curve in Fig. 11(a) for different relative humidity at cathode inlet. From Figs. 11(a) and (b), it can be observed that the cell voltage decreases as the power requirement increases from 0 to 14 s, and then increases as the power requirement decreases. The maximum value observed for the operating parameters and the corresponding time the maximum is observed is presented in Table 5. It can be seen from Table 4 that anode pressure assumes the maximum value of 4.16, 4.11 and 3.99 bar for RH_c = 0%, 50% and 100 %,

respectively, at t = 1.75 s. Similar is observed for cathode pressure with maximum value of 4.05, 4.07 and 4.34 bar for RH_c = 0%, 50% and 100 %, respectively, at t = 1.75 s.

Similar to Fig. 10 and 11, Fig. 12 present the results from the optimization studies for different values of cathode inlet relative humidity for tracking power curve C3. It can be seen from Fig. 12(a) that the simulated power curves closely match the desired power curve indicating that the current fuel cell setup satisfies the part of US06 drive cycle [14] power requirements. It can be seen that power curve almost drops to zero for t = 9.0, reaching a peak of around 64 kW around 10 s, further reaching 0 at 19.6 s. Figure 12(b) shows the temporal variation of optimized cell voltage corresponding to the simulated power curve in Fig. 12(a) for different relative humidity at cathode inlet. From Figs. 12(a) and (b), it can be observed that the cell voltage decreases as the power requirement increases from 0 to 14 s, and then increases as the power requirement decreases. For the sudden drop in power density around 9.0 s it is seen that the voltage increases sharply such as to match the reduction in power density required. The maximum value observed for the operating parameters and the corresponding time is presented in Table 6. It can be seen from Table 6 that maximum for anode and cathode pressure occurs for different times compared to that observed for curve C2. It is also noted that the cathode pressure, mass flow rate at anode and cathode are maximized at 17.0 s whereas the anode pressure is maximized at t = 18.0 s.

The results presented in this section offer insight into the effects of various operating parameters on the hydration transient operation of fuel cells and the correlation with power density. The detailed investigation indicates that power response is strongly correlated to time scale of different transport mechanisms. For longer response time, the effects of water transport are significant which otherwise is hidden for shorter time periods. Optimization studies reflect the transient variation in cell voltage with the maximum for anode and cathode pressure and mass flow rates for various values of humidity at cathode inlet in order to meet US06 drive cycle [14] power requirements. Future work could, parametric studies for other cyclic and non-cyclic variations in operating parameters using the present model. Also, optimization studies taking into consideration the time constant associated with feed and control system are worth exploring and more realistic. The numerical model can be used to develop network-based models, characteristically reducing the simulation time for optimization studies. The use of 2D and 3D models for simulation on parallel basis can offer further insights in to the optimization of the operating parameters.

3.5 Nomenclature

A	superficial electrode area [m^2]
C_k	molar concentration of species k [mol/ m^3)]
D	mass diffusivity of species [m^2/ s]
E_{cell}	cell potential or voltage [V]
EW	equivalent weight of dry membrane [kg/ mol]
F	Faraday Constant [96,487 C/ equivalent]
j	transfer current [A/ m^3]
K	permeability [m^2]
n_d	electro-osmotic drag coefficient [H_2O/ H^+]
p	pressure [bar]
RH	Universal gas constant [8.314 J/ mol K]
S	relative humidity
t	source term in transport equations
T	temperature [K]
$\vec{u}$	velocity vector

Greek letters

α	transfer coefficient
ε	porosity
η	surface overpotential [V]
λ	membrane water content
μ	viscosity [kg/ m s]
ρ	density [kg/ m^3]
σ	electronic conductivity [S/ m]
τ	shear stress [N/ m^2]; time constant; tortuosity
ϕ	phase potential [V]

Superscripts and subscripts

a	anode
c	cathode

$cell$	single fuel cell
d	desired value
e	electrolyte
eff	effective value
eq	equivalent
g	gas phase
in	inlet
k	species
m	membrane phase
o	t=0 s, initial state
ref	reference value
s	electronic phase, simulated values
sat	saturated value
SS	steady state
t	time > 0 s
w	water

References

[1] Wang, C.Y., 2004, “Fundamental Models for Fuel Cell Engineering," Chemical Reviews, 104, pp. 4727-4766.

[2] Perry, M.L., Fuller, T.F., 2002, “A Historical Perspective of Fuel Cell Technology in the 20th Century,” J. Electro-chemical So., 149 (7), pp. S59-67.

[3] Sørensen, B., 2012, “Fuel Cells: Optimism Gone – Hard Work Still There,” Int. Jo. of Hydrogen Energy, In Press. DOI- 10.1016/ j.bbr.2011.03.031.

[4] Wang, Y., Wang, C.Y., 2005, “Transient Analysis of Polymer Electrolyte Fuel Cells,” Electrochem. Acta, 50, pp. 1307-1315

[5] Wang, Y., Wang, C.Y., 2006, “Dynamics of Polymer Electrolyte Fuel Cells Undergoing Load Changes,” Electrochem. Acta, 51, pp. 3924-33.

[6] Wang, L., Husar, A., Zhou, T., Liu, H., 2003, “A Para-metric Study of PEM Fuel Cell Performances,” Int. Jo. of Hydrogen Energy, 28, pp. 1263-1272

[7] Zhang, Z., Wang, X., Zhang, X., Jia, L., 2008, “Optimizing the Performance of a Single Channel PEM Fuel Cell,” ASME Journal of Fuel Cell Science and Technology, 5, pp. 031007-(1-9).

[8] Mawardi, A., Yang, F., Pitchumani, R., 2005, "Optimization of the Operating Parameters of a Proton Exchange Membrane Fuel Cell for Maximum Power Density," ASME Journal of Fuel Cell Science and Technology, 2, pp. 121-135.

[9] Zhang, Y., Mawardi, A., Pitchumani, R., 2006, "Effects of Operating Parameters on the Uniformity of Current Density Distribution in Proton Exchange Membrane Fuel Cells," ASME Journal of Fuel Cell Science and Technology, 3(4), pp. 464-476.

[10] Um, S., Wang, C. Y., Chen, K.S., 2000, “Computational Fluid Dynamics Modeling of Proton Exchange Membrane Fuel Cells,” J. Electrochemical So., 147 (12), pp. 4485-93.

[11] Bird, R.B., Stewart, W.E., Lightfoot, 1960, E.N., Transport Phenomena, Wiley, New York.

[12] Springer, T.E., Zawodzinski, T.A., Gottesfeld, S., 1991, “Polymer Electrolyte Fuel Cell Model,” J. Electrochemical So., 138 (8), pp. 2334-42.

[13] Motupally, S., Becker, A.J., Weidner, J.W., 2000, “Diffusion of Water in Nafion 115 Membranes,” J. Electro-chemical So., 147 (9), pp. 3171-77.

[14] Markel, T., Zolot, M., Wipke, K.B., Pesaran, A.A, 2003, “Energy Storage System Requirements for Hybrid Fuel Cell Vehicles,” Advanced Automotive Battery Conference, Nice, France, June 10-13.

[15] Nelder, J. A., Mead, R., 1965, "A Simplex Method for Function Minimization," Comput. J. (UK), 7, pp. 308 – 313

[16] Mawardi, A., Pitchumani, R., 2003, "Optimal Temperature and Current Cycles for Curing of Composites using Internal Resistive Heating," ASME J. Heat Trans., 125, pp. 126–136.

[17] Press, W. H., Flannery, B. P., Teukolsky, S. A., Vettering, W. T., 1992, Numerical Recipes in FORTRAN, Cambridge University Press, New York, NY.

Table 3.1: Source terms in the governing equations

Domain	S_V	S_i	S_s, S_m
Gas channels	0	0	0
Diffusion layers	$-\frac{\mu}{K_{GDL}}\vec{u}$	0	0
Catalyst layers	$-\frac{\mu}{K_{GDL}}\vec{u}$	Anode	Anode
		$-\frac{j_a}{2F}$ $(i = H_2)$	$S_s = -j_a < 0$
		0 $(i = O_2)$	$S_m = +j_a < 0$
		$-\nabla.\left(\frac{n_d i_e}{F}\right)$ $(i = H_2O)$	
		Cathode	Cathode
		0 $(i = H_2)$	$S_s = +j_c > 0$
		$-\frac{j_c}{4F}$ $(i = O_2)$	$S_m = -j_c < 0$
		$\frac{j_c}{2F} - \nabla.\left(\frac{n_d i_e}{F}\right)$ $(i = H_2O)$	
Membrane	$-\frac{\mu}{K_{GDL}}\vec{u}$	0	0

Table 3.2. Mean and amplitude of the cyclic variation of parameters used in the numerical simulations

Parameter [units]	Mean (θ_0)	Amplitude (θ_A)
Cell Voltage E_{cell} [V]	0.65	0.1
Anode Pressure p_a [bar]	4	1
Cathode Pressure p_c [bar]	4	1
Anode Inlet Velocity u_a [m/ s]	0.1026	0.0308
Cathode Inlet Velocity u_c [m/ s]	0.2299	0.0458

Table 3.3. Geometrical and physical parameters used in the numerical simulations [4,5,9]

Parameter [units]	Symbol	Value
Gas channel depth [mm]		1.0
Diffusion layer thickness [mm]		0.3
Catalyst layer thickness [mm]		0.01
Membrane (N112) thickness [mm]		0.051
Fuel cell/ Gas channel length [mm]		100.0
Temperature [K]	T	353
Permeability of diffusion layer [m^2]	K_{GDL}	10^{-12}
Permeability of catalyst layer [m^2]	K_{CL}	10^{-15}
Gas diffusion layer porosity	ε_{GDL}	0.6
Catalyst layer porosity	ε_{CL}	0.4
Volume fraction membrane in catalyst layer	ε_m	0.26
Anode reference exchange current density [A/ m^3]	$j_{a,ref}$	5.00×10^8
Cathode reference exchange current density [A/ m^3]	$j_{c,ref}$	500
H_2 diffusivity membrane [m^2/ s]	$D_{H_2,mem}$	2.59×10^{-10}
H_2 diffusivity in gas [m^2/ s]	$D_{H_2,ref}$	1.1×10^{-4}
O_2 diffusivity in gas [m^2/ s]	$D_{O_2,ref}$	3.2348×10^{-5}
H_2O diffusivity in gas [m^2/ s]	$D_{H_2O,ref}$	7.35×10^{-5}

Table 3.4: Maximum values of operating parameters and the corresponding time for power curve in Fig. 10. (C1)

RH_c [%]	Anode Pressure p_a [bar]		Cathode Pressure p_c [bar]		Anode Mass Flow Rate, $\dot{m}_a$ [kg/ s]		Cathode Mass Flow Rate, $\dot{m}_c$ [kg/ s]	
	Max.	*t*	*Max.*	*t*	*Max.*	*t*	*Max.*	*t*
0	3.36	13.0	4.51	2.0	7.27×10^{-5}	20.0	5.20×10^{-4}	11.0
50	3.86	13.0	4.93	13.0	7.67×10^{-5}	19.0	6.13×10^{-4}	16.0
100	4.99	16.0	3.25	19.0	7.62×10^{-5}	5.0	5.30×10^{-4}	2.0

Table 3.5: Maximum values of operating parameters and the corresponding time for power curve in Fig. 11. (C2)

RH_c [%]	Anode Pressure, p_a [bar]		Cathode Pressure, p_c [bar]		Anode Mass Flow Rate, $\dot{m}_a$ [kg/ s]		Cathode Mass Flow Rate, $\dot{m}_c$ [kg/ s]	
	Max.	*t*	*Max.*	*t*	*Max.*	*t*	*Max.*	*t*
0	4.16	1.75	4.05	1.75	8.00×10^{-5}	14.6	3.90×10^{-4}	19.6
50	4.11	1.75	4.07	1.75	7.97×10^{-5}	12.0	6.24×10^{-4}	7.6
100	3.99	1.75	4.34	1.75	6.42×10^{-5}	11.0	4.27×10^{-4}	19.6

Table 3.6: Maximum values of operating parameters and the corresponding time for power curve in Fig. 12. (C3)

RH_c [%]	Anode Pressure, p_a [bar]		Cathode Pressure, p_c [bar]		Anode Mass Flow Rate, $\dot{m}_a$ [kg/ s]		Cathode Mass Flow Rate, $\dot{m}_c$ [kg/ s]	
	Max.	*t*	*Max.*	*t*	*Max.*	*t*	*Max.*	*t*
0	4.30	18.0	4.49	17.0	6.88×10^{-5}	17.0	1.29×10^{-4}	17.0
50	4.19	2.4	4.03	16.1	7.91×10^{-5}	18.0	1.72×10^{-4}	12.4
100	4.14	3.2	4.27	5.9	7.59×10^{-5}	8.8	5.40×10^{-4}	8.3

Chapter 4: Influence of Membrane Properties on the Transient Behavior of Polymer Electrolyte Fuel Cells

Toward understanding the effects of membrane properties on the dynamic behavior, this chapter presents numerical simulations for a single channel PEM fuel cell undergoing changes in load, by subjecting the unit cell to a step change in current. The complex interaction between cell voltage response and water transport dynamics for various membrane properties is explored in detail, where the performance is critically related to the water content of the membrane. Detailed computational fluid dynamics (CFD) simulations are carried out to show that step increase in current density leads to anode dryout due to electro-osmotic drag, and to investigate the dependence of transient behavior on the variations in membrane properties. The results show that water uptake by the membrane is a crucial factor in determining the occurrence of anode dryout and hence voltage reversal, and can be avoided by a graded membrane design.

4.1 Introduction

The performance of a fuel cell is critically related to the membrane hydration, as it affects the proton conductivity through membrane—a higher water content (number of water molecules per sulfonic acid group) in the membrane ensures higher conductivity. Under low-humidity operation, suitable for automotive applications, electro-osmotic drag, back-water diffusion and rate of water supply or removal through humidified reactants, each associated with different time scales, interact in complex ways to affect the transient behavior of PEM fuel cells. The step increase in current density causes the anode side of the membrane to quickly dryout owing to electro-osmotic drag whereas back-diffusion of water from cathode to anode takes longer to rehydrate the membrane. This can lead to temporary dryout and hence sharp voltage drop, owing to jump in membrane resistance. As the back-diffusion rehydrates the anode side, the voltage recovers, improving the performance. The above transient behavior is strongly dependent on the transport and physical properties of the membrane namely, the water diffusion coefficient, electro-osmotic drag coefficient, thickness and equivalent weight, and needs to be studied in detail. Understanding the transient behavior and effect of membrane

properties is of paramount importance for PEM fuel cells to be successfully deployed for mobile applications [1,2].

Several researchers have attempted to study the transient behavior of PEM fuel cells experimentally and numerically [3-14]. Hamelin et al. [3] studied the behavior and performance of a proton exchange membrane fuel cell stack for fast load commutations, observing that the system response was faster than 0.15 s. Kim et al. [4,5] investigated the effects effect of stoichiometry, reservoir and fuel dilution on the transient response of fuel cell, and elucidated the undershoot and overshoot characteristics for change in loads at fixed flow rate. Benziger et al. [6] studied the dynamic response of a stirred tank reactor (STR) PEM fuel cell for changes in load, emphasizing the role of membrane water uptake in ignition and extinguished state of the fuel cell. Yan et al. [7], in their experiments, investigated the steady state and dynamic performance of PEM fuel cells. The results showed cathode humidity, stoichiometric flow ratio and cell temperature as key parameters affecting the performance and being related to the water transport. The above studies point the importance of water transport and membrane hydration in the performance and transient response of fuel cells.

The transient response of fuel cells has been investigated numerically in several studies. The model by Um et al. [8] assumed constant water content and investigated the transient response of fuel cell, emphasizing the effects of reactant diffusion. Amphlett et al. [9] developed a lumped-parameter based thermal model to predict the transient response, while using steady-state electrochemical kinetics. Pathapati et al. [10] and Xie et al. [11] developed simplified system level models for their transient study. Ceraolo [12] used a simplified one-dimensional model to study the dynamic behavior, considering only the cathode side. These numerical studies used simplified models and lacked detail representation of complex interactions during transient operations. A more complete model was developed by Wang and Wang [13,14], extending the model used in Ref. [8] to include the effects of water accumulation and electrochemical double layer discharge. The transient model explored the dynamic behavior for step change in humidity, voltage and current, emphasizing the different time scales characteristic to transport and electrochemical process. To the authors' knowledge, Wang and Wang [14] were the first to simulate the effects of step changes in current load. The effects of two different membrane thicknesses on the dynamic behavior were studied in detail. It was

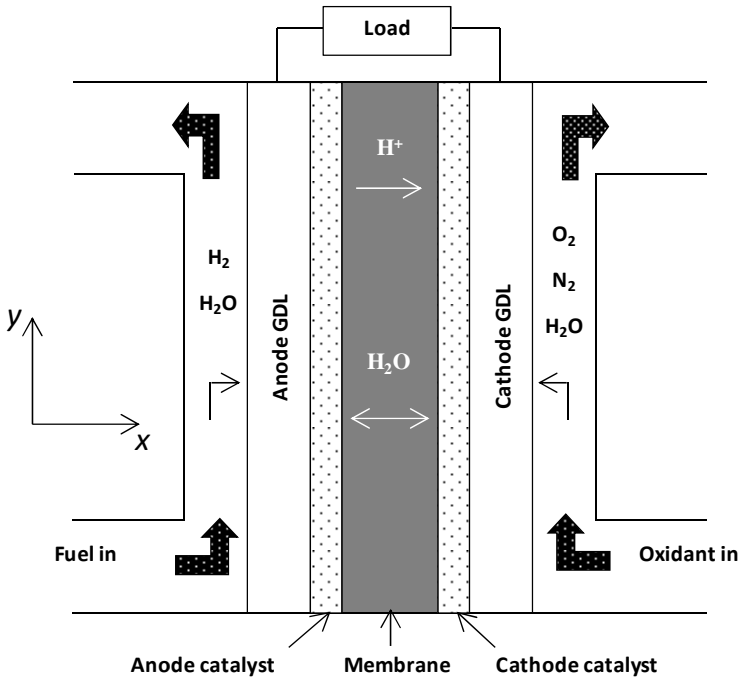

Figure 4.1: Schematic of PEM fuel cell

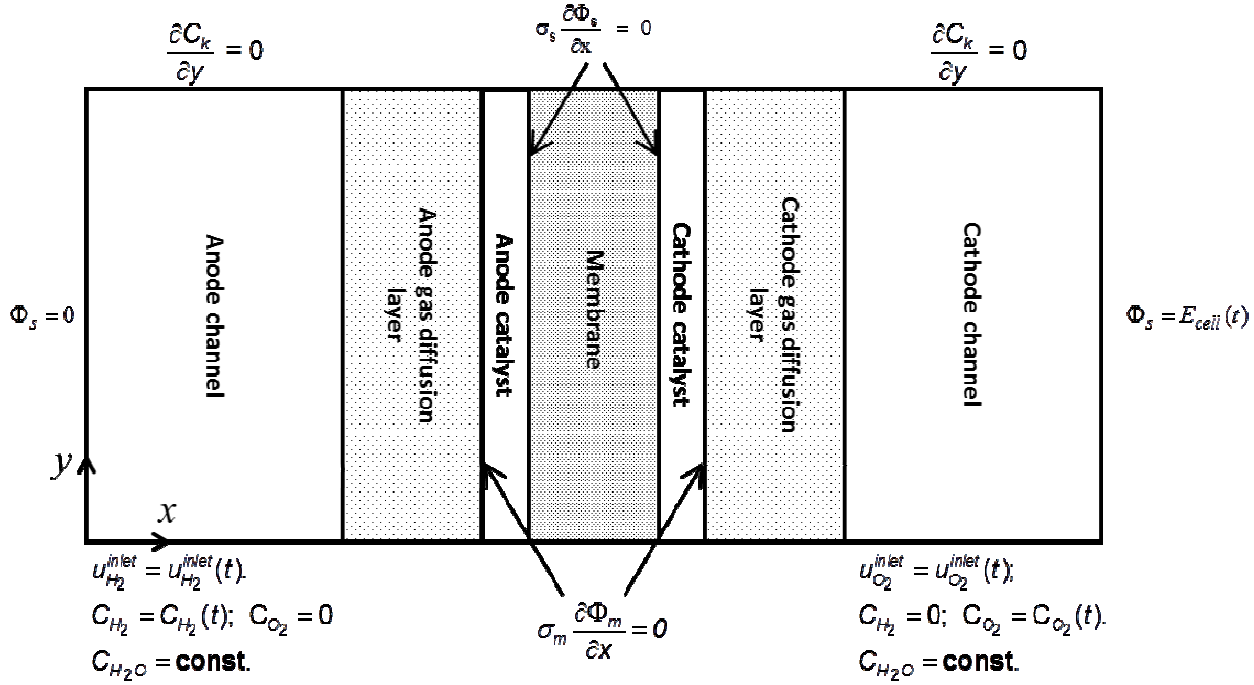

Figure 4.2: Schematic of model domain and associated boundary conditions.

pointed out in their study that the increase in current density leads to drying of anode leading to sudden drop in voltage.

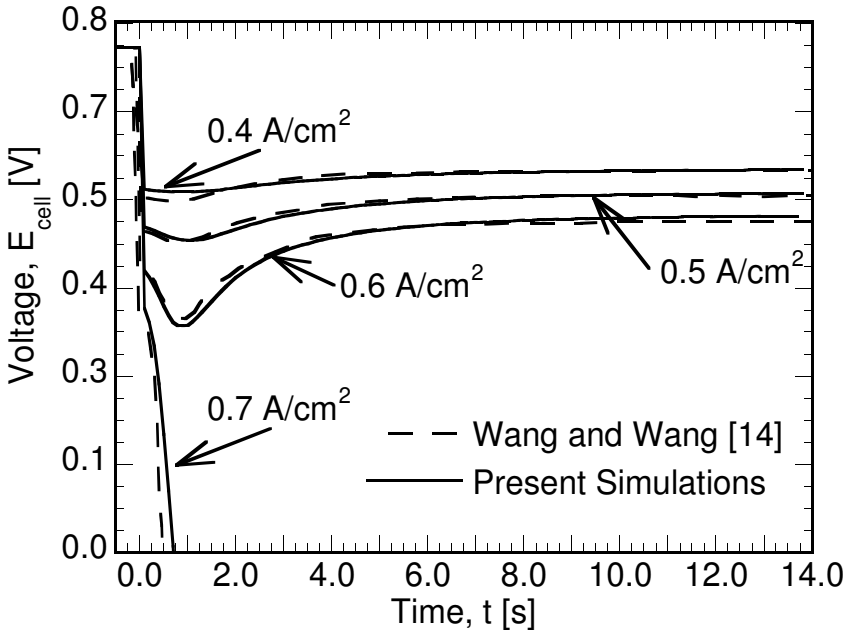

Figure 4.3: Cell voltage variation with current density for step change in current density from I = 0.1 to 0.4, 0.5, 0.6, 0.7 A/cm^2.

In the present study, computational fluid dynamics (CFD) simulations are carried out using the model developed in Ref. [14] to study the effect of step change in current density. Although the work by Wang and Wang [14] provides mathematically rigorous description of the governing physics, the transport properties vary extensively by orders of magnitude and their influence has not been addressed in detail in previous studies. Majsztrik [15] presented an elaborate compilation of the diffusivity values of water in Nafion and the experimental techniques used, with values spanning over three orders of magnitude, at a single temperature. Similarly, the variations in water uptake, electro-osmotic drag coefficient, ionic-conductivity of membrane have been presented in Refs. [16], [17] and [18], respectively. The variations in the physical and transport properties of GDL and membrane play an important role in determining the transient behavior of membrane and are addressed in detail in the present study. The mathematical model used as the basis of the study is presented in Section 2 and the results are reported and discussed in Section 3.

4.2 Mathematical Model

The mathematical model used in this chapter is similar to that described in section 2.2 and has been omitted for brevity.

4.3 Results and Discussion

The numerical model described in the previous section is first validated by comparing the cell voltage (E_{cell}) response with the numerical results reported by Wang and Wang [14]. Figure 3 shows the cell voltage variation with current density for step change in current density from I = 0.1 to 0.4, 0.5, 0.6, 0.7 A cm^{-2}, where the solid lines represent the results from present simulations, and the results from Ref. [14] are indicated by dashed lines. It can be seen that the cell voltage drops instantaneously owing to the time-scale associated with the electrochemical double layer discharge, on the order of micro-to-milli-seconds. In addition, at low-humidity operating conditions, the voltage response is seen in Fig. 3 to exhibit an undershoot, with the degree of undershoot increasing as the magnitude of current change is increased. For I = 0.7 A/cm^2, Fig. 3 shows that the voltage drops to zero, indicating a voltage reversal. The undershoot in the voltage response can be attributed to the jump in water electro-osmotic drag, which increases proportionally to the step change in the current density. This causes the anode to dryout and, in turn, increases the membrane resistance, leading to further drop in the voltage to a minimum. As the membrane at anode is rehydrated, the membrane resistance decreases, leading to increase in voltage and achieving steady state. The time scale associated with the back-diffusion of water dictates the time taken for the voltage response to improve, and is on the order of 0.7 s for the parametric combination considered. The figure shows close agreement between the voltage response obtained for the present simulations and those reported in Ref. [14].

The comparisons presented in Fig. 3 demonstrate the capabilities of the present model to accurately capture the water transport dynamics and predict voltage response, which forms the basis of the further studies reported in this section. The effects of water diffusivity in the GDL, gas channels and the membrane, the equivalent weight of membrane, the electro-osmotic drag coefficient and water uptake in the membrane on the dynamic response of the fuel cell is presented in the following discussion. Temporal variations in cell voltage for step change in current load are plotted to elucidate the response and is discussed in detail.

Figures 4(a) to (d) present the transient variation in cell potential for various H_2O diffusivity

values in the gas channel, $D_{H_2O}^{ref}$, as the current density is stepped up from (a) 0.1 A/cm^2 to 0.4 A cm^{-2}, (b) 0.1 A cm^{-2} to 0.5 A cm^{-2}, (c) 0.1 A/cm^2 to 0.6 A cm^{-2}, and (d) 0.1 A cm^{-2} to 0.7 A cm^{-2},

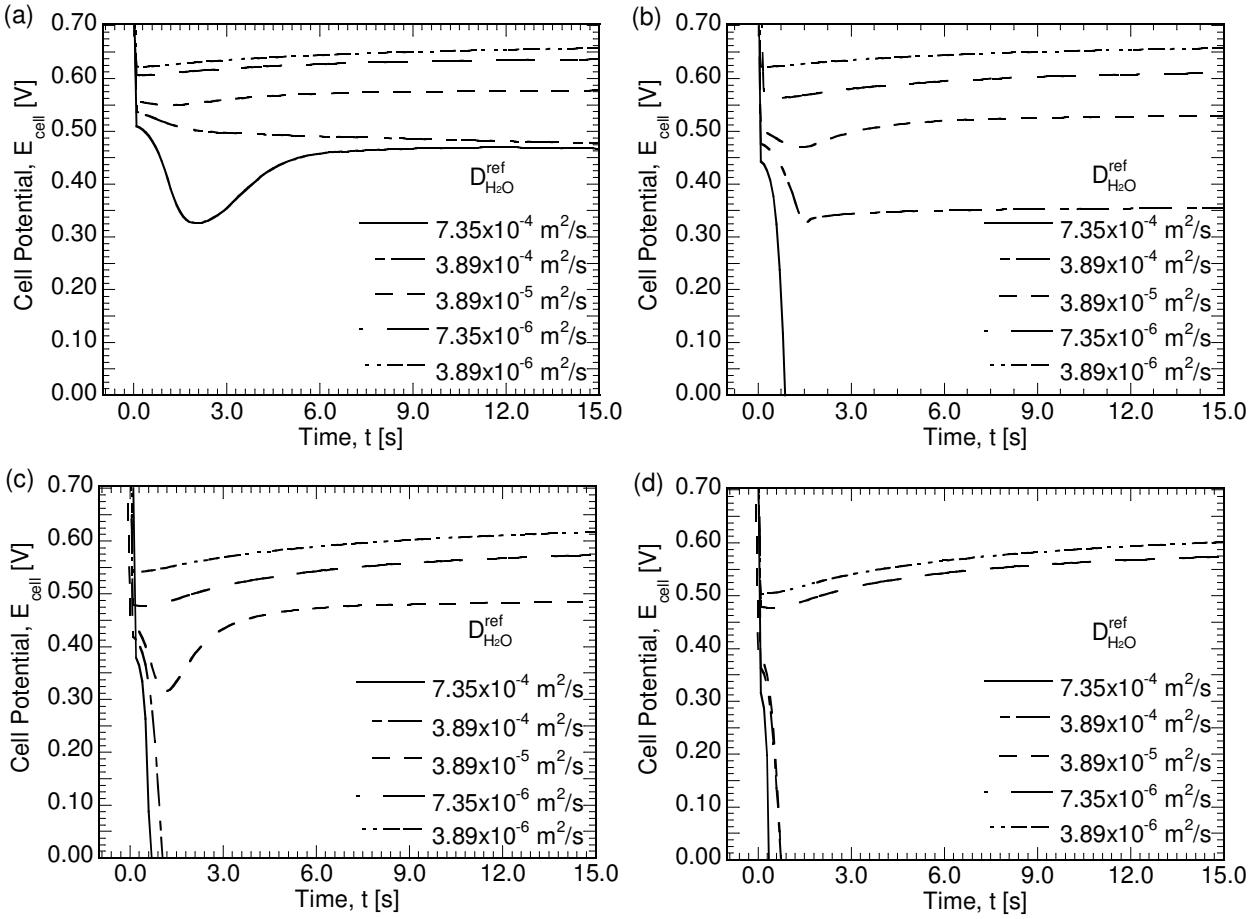

Figure 4.4: Transient variation in cell potential for various $D_{H_2O}^{ref}$, for (a) 0.1 A/cm^2 to 0.4 A/cm^2, (b) 0.1 A/cm^2 to 0.5 A/cm^2, (c) 0.1 A/cm^2 to 0.6 A/cm^2, and (d) 0.1 A/cm^2 to 0.7 A/cm^2, respectively.

respectively. In each plot, the effect of water diffusivity in gas is investigated for diffusivity values ranging from 3.89×10^{-6} m^2 s^{-1} to 3.89×10^{-4} m^2 s^{-1}, while the diffusivity values of the other reactants are kept constant as specified in Table 1. From Fig. 4(a) it is observed that, A cm^{-2} following the instantaneous drop in cell voltage, which is attributed to the time scale associated with electrochemical double layer discharge as explained before, the cell voltage recovers to a steady state, for all the diffusivity values except for $D_{H_2O}^{ref} = 3.89 \times 10^{-4}$ m^2/s. For $D_{H_2O}^{ref} = 7.35 \times 10^{-6}$ m^2 s^{-1}, the degree of voltage undershoot is the most, with voltage reaching a minimum at t = 2 s, as seen in Fig. 4(a). In contrast to that observed in Fig. 4(a), for a step change in current

density from 0.1 A cm^{-2} to 0.5 A cm^{-2} (Fig. 4(b)), voltage reversal occurs for $D_{H_2O}^{ref} = 7.35 \times 10^{-4}$ m^2/s , whereas for step change from 0.1 A cm^{-2} to 0.6 A cm^{-2} (Fig. 4(c)) voltage reversal occurs

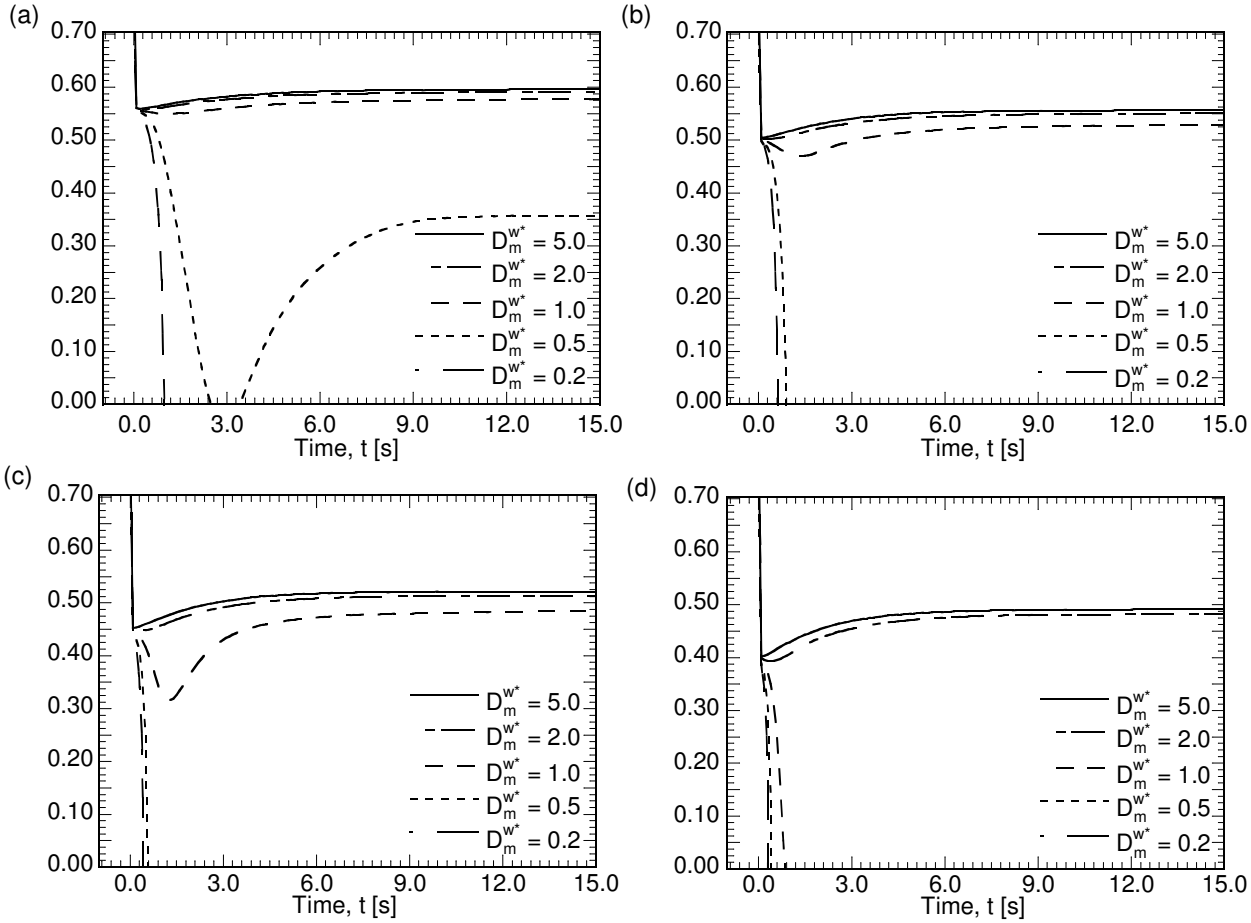

Figure 4.5: Transient variation in cell potential for various D_m^w, for (a) 0.1 A/cm^2 to 0.4 A/cm^2, (b) 0.1 A/cm^2 to 0.5 A/cm^2, (c) 0.1 A/cm^2 to 0.6 A/cm^2, and (d) 0.1 A/cm^2 to 0.7 A/cm^2, respectively.

for $D_{H_2O}^{ref} = 3.89 \times 10^{-4}$ and 7.35×10^{-4} m^{2}s^{-1} and for $D_{H_2O}^{ref} = 3.89 \times 10^{-4}, 7.35 \times 10^{-4}$ and 3.89×10^{-5} m^2 s^{-1} given step change in current density from 0.1 A cm^{-2} to 0.7 A cm^{-2} (Fig. 4(d)), resulting from anode dryout. Significant voltage undershoot is observed for $D_{H_2O}^{ref} = 7.35 \times 10^{-4}$ m^2 s^{-1} in Fig. 4(a) which is recovered with back-diffusion of water to the anode, with an undershoot of around 0.2 V. It can be seen in Fig. 4(a) to 4(d) that there exists a non-monotonic trend associated with variation in steady state cell potential values for different diffusivity values, with $D_{H_2O}^{ref} = 7.35 \times 10^{-4}$ m^2 s^{-1} and 3.89×10^{-6} m^2 s^{-1} defining the minimum and maximum values of steady state voltages, respectively, in Fig. 4(a). The diffusivity at the porous

layers determines the rate at water is transported to and from the anode and the cathode sides, determining the amount of water contained in the membrane. It is also noted that, for lower diffusivity values, voltage reversals are not observed (Fig. 4(a) to 4(d)). Although the properties of membrane are fixed, change in diffusivity values of water in porous layers presents a complex dynamic behavior affecting the time scales for voltage recovery. Therefore, it can be established that water diffusion through porous layers significantly affects the water distribution process, thus determining the voltage response for change in current.

Figures 5(a) to (d) depict the change in cell potential with time for different values of water diffusivity in the membrane as the current density undergoes a step change from (a) 0.1 A cm^{-2} to 0.4 A cm^{-2}, (b) 0.5 A cm^{-2}, (d) 0.6 A cm^{-2} and (d) 0.7 A cm^{-2}, respectively. The water diffusivity in membrane D_m^w is a function of the membrane water content, λ, and temperature, T, as defined in Eq. (11). The effect of variation in membrane diffusivity is studied by varying D_m^{w*}, where D_m^{w*} is a dimensionless parameter defined by $D_m^{w*} = \frac{D_m^w}{Eq.\ (11)}$. In the present study, D_m^{w*} is varied from 0.2 to 5 for the cases described above, while the other properties are fixed as given in Table 1. The change in net diffusion of water through the membrane can be also attributed to the changes in temperature and membrane thickness, thus the corresponding effects are not evaluated independently but can be represented by variations in the effective water diffusivity in the membrane.

In Fig. 5(a) it can be seen that $D_m^{w*} = 0.5$ almost defines the limiting case for voltage reversal. As seen from Figs. 5(a), 5(b) and 5(c), the voltage reversal occurs for $D_m^{w*} < 1.0$, whereas voltage reversal occurs for $D_m^{w*} < 2.0$ for step change in current density from 0.1 to 0.7 A cm^{-2} (Fig. 5(d)). Owing to the higher magnitude of step changes in current density, from 0.1 to 0.6 A/cm^2 and 0.1 to 0.7 A cm^{-2} in Fig. 5(c) and 5(d), respectively, voltage reversal occurs for a relatively high diffusivity value compared to that is observed in Fig. 5(a) and 5(b). Also, it is noted that for $D_m^{w*} = 1.0$, the extent of undershoot observed in the voltage is much larger in Fig. 5(c) compared to those observed in Fig. 5(a) and 5(b). It can be seen from Fig. 5(d) that, for $D_m^{w*} = 1.0$, the cell undergoes voltage reversal for step change in current density from 0.1 to 0.7 A cm^{-2}. Although, voltage reversal also occurs for $D_m^{w*} = 0.5$, for a step change in current density from 0.1 A cm^{-2} to 0.4 A cm^{-2} (Fig. 5(a)), the cell voltage recovers upon rehydration, after a reversal period from t = 2.5 to 3.5 s. For the higher diffusivity values, no undershoot is observed and the cell reaches

steady state following the expected initial instantaneous decrease in cell voltage, as illustrated in Figs. 5 (a) to (d) for $D_m^{w*} > 2$. This behavior can be attributed to the increased transport rate of

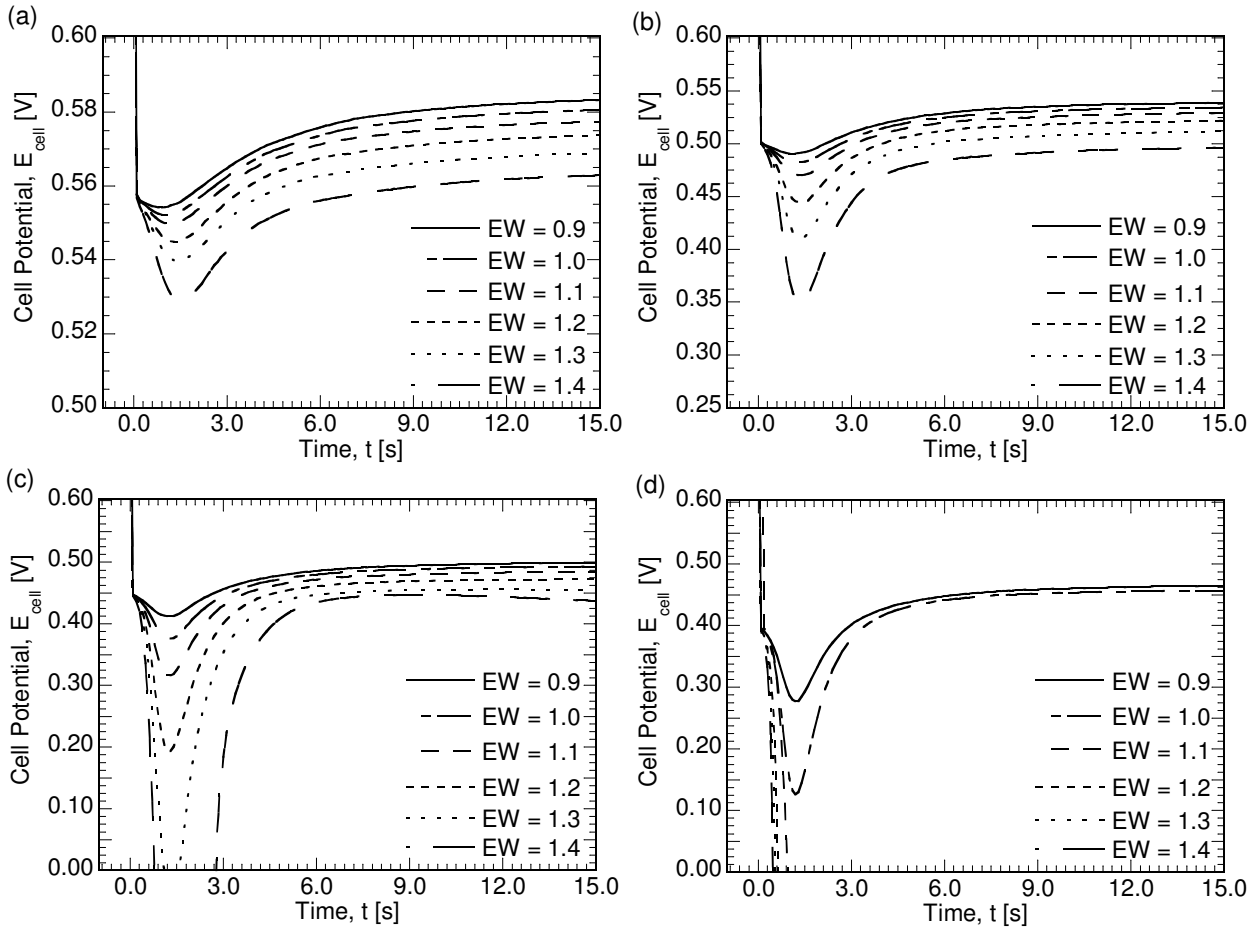

Figure 4.6: Transient variation in cell potential for various *EW*, for (a) 0.1 A/cm² to 0.4 A/cm², (b) 0.1 A/cm² to 0.5 A/cm², (c) 0.1 A/cm² to 0.6 A/cm², and (d) 0.1 A/cm² to 0.7 A/cm², respectively.

water generated at cathode to anode through back-diffusion. The diffusivity of water through membrane effects the distribution of water in the membrane, both through the thickness and along the direction of flow, thus affecting the steady state cell potential values. In Fig. 5(a), it can be seen that steady state values are nearly unaffected for $D_m^{w*} > 1.0$, whereas at $D_m^{w*} = 0.5$, the steady state recovered voltage value is much lower. Similar behavior is observed for $D_m^{w*} > 2.0$ in Figs. 5(b), 5(c) and 5(d), with the difference in the steady state voltage recovery value increasing with increasing amplitude of change in current density.

These trends can also be used to qualitatively explain the effect of change in thickness of

membrane on the transient response, where $D_m^{w*} > 1.0$ would represent decrease in thickness of membrane and $D_m^{w*} < 1.0$ would represent increase from the base value. The decrease in

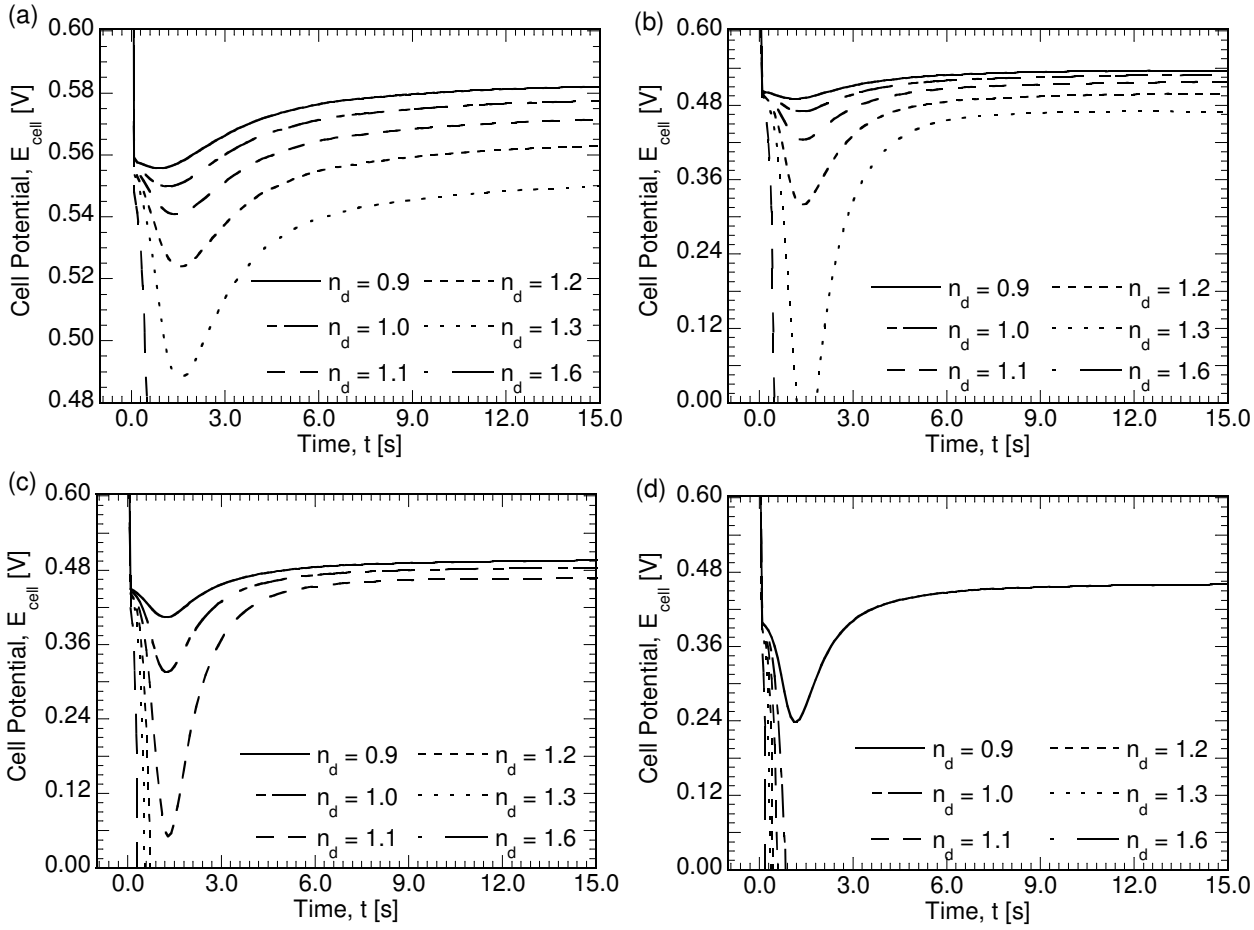

Figure 4.7: Transient variation in cell potential for various n_d, for (a) 0.1 A/cm² to 0.4 A/cm², (b) 0.1 A/cm² to 0.5 A/cm², (c) 0.1 A/cm² to 0.6 A/cm², and (d) 0.1 A/cm² to 0.7 A/cm², respectively.

thickness leads to increase in rate at which water is transported back to anode through back-diffusion, thus affecting the dynamic response. The decrease in thickness causes the membrane to fail early due to reduced structural ability and thus use of reinforced membranes with better structural stability is desirable. The equivalent molecular weight of dry membrane in kg mol^{-1} is denoted as *EW*, with lower values of *EW* indicating higher moles per kg, and, in turn, increased number of sulfonic acid groups. Increase in number of sulfonic acid groups leads to an increase in the amount of water stored in the unit mass membrane, for a given water activity. An increase in *EW* leads to a decrease in the amount of water that can be accumulated by

membrane for a given water activity. The effect of variations in *EW* on the dynamic response is presented in Fig. 6. Figures 6(a) to (d) depict the cell voltage response for change in current density from (a) 0.1 A cm^{-2} to 0.4 A cm^{-2}, (b) 0.1 A cm^{-2} to 0.5 A cm^{-2}, (c) 0.1 A cm^{-2} to 0.6 A cm^{-2} and (d) 0.1 A cm^{-2} to 0.7 A cm^{-2}, respectively, for various equivalent weights, *EW*. The results presented in Figs. 4 and 5 were based on *EW* = 1.1 and Fig. 6 shows the effect of varying *EW* from 0.9 to 1.4, in steps of 0.1. Similar to the observations in Figs. 4 and 5, a step change in current density is seen in Fig 6(a)-(d) to lead to sudden drop in voltage, followed by an undershoot due to membrane dryout and recovery on rehydration from back-diffusion of water to anode. It can be seen in Fig. 6(a) that an increase in *EW* from 0.9 to 1.4 leads to an increase in the degree of undershoot, with cell voltages approaching different steady state values for different *EW*'s over time. For the change in current density from 0.1 to 0.5 A cm^{-2} (Fig. 6(b)), there is an increase in the amount of observed undershoot compared to that observed in Fig. 6(a), owing to increase in current density from 0.4 to 0.5 A cm^{-2}.

Similar behavior is observed in Figs. 6(c) and 6(d), with an exception of voltage reversal for *EW* > 1.2 in Fig. 6(c) and *EW* > 1.0 in Fig. 6(d). The increase in the degree of undershoot can be attributed to a faster dryout of anode side of the membrane, with increase in *EW*, as the same amount of water is dragged to the cathode but the holding capacity is reduced with increase in *EW*. As previously observed in Fig. 5, the steady state cell voltage values vary monotonically with *EW*. It is also noted from Figs. 6(a)-(d) that with increase in *EW* the time taken for the membrane to rehydrate also increases. The time taken by the cell potential to reach a steady state value is dependent on the time scale associated with time constant for membrane hydration, which is inversely proportional to *EW*.

Figures 7(a) to (d) show the temporal variation in cell potential for various electro-osmotic drag coefficient, n_d, values as the current density undergoes a step change from (a) 0.1 A cm^{-2} to 0.4 A cm^{-2}, (b) 0.1 A cm^{-2} to 0.5 A cm^{-2}, (c) 0.1 A cm^{-2} to 0.6 A cm^{-2} and (d) 0.1 A cm^{-2} to 0.7 A cm^{-2}, respectively. The electro-osmotic drag coefficient gives a representative figure of the effective moles of water transported per mole of protons conducted from anode to cathode catalyst layer and appears as a source term (Table 1) in species conservation equation for water Eq. (4). The values of n_d used in the present study range from 0.7 to 2.0, following the values reported in Refs. [15-18]. Note that larger values of n_d indicate more water being transported from anode to

cathode, for a specified current density. It can be seen in Fig. 7(a) that cell voltage reaches zero for n_d > 1.3, whereas owing to increase in current density to 0.5 A cm^{-2} in Fig. 7(b), the voltage reaches zero and finally reverses for n_d > 1.2. Similar behavior is observed for n_d > 1.1 for step

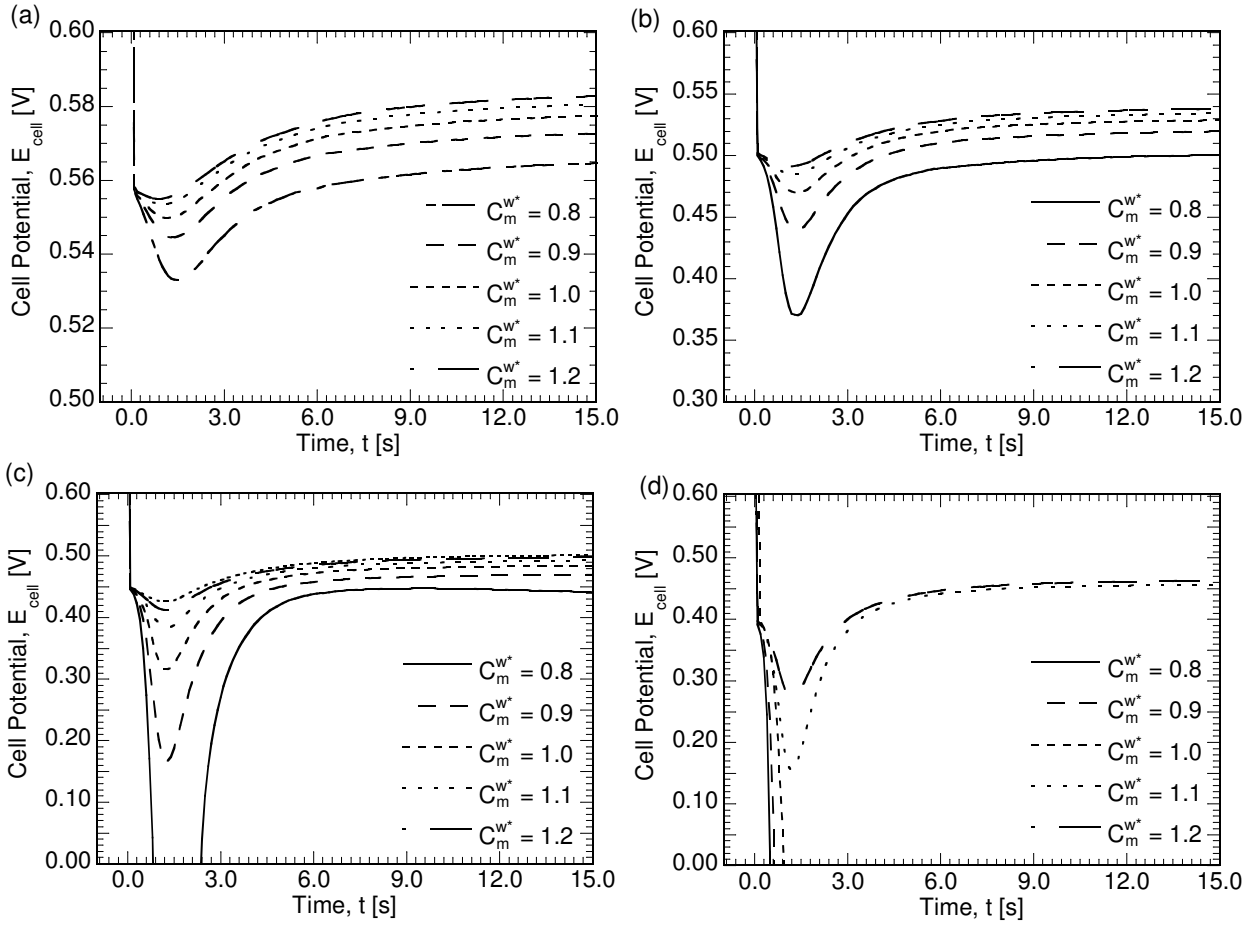

Figure 4.8: Transient variation in cell potential for various C_m^w, for (a) 0.1 A/cm² to 0.4 A/cm², (b) 0.1 A/cm² to 0.5 A/cm², (c) 0.1 A/cm² to 0.6 A/cm², and (d) 0.1 A/cm² to 0.7 A/cm², respectively.

change in current density to 0.6 A cm^{-2} in Fig. 7(c) and for n_d > 0.9 for change to 0.7 A cm^{-2} in Fig. 7(d). It is also noted in Fig. 7(a) that there is no observable undershoot in voltage due to drag for n_d < 1.0, and the voltage recovers as the membrane is further hydrated by back-diffusion. Similar behavior is observed for n_d < 0.9 in Fig. 7(b) and for n_d < 0.8 in Fig. 7(c), whereas in Fig. 7(d) there exists an undershoot for the all the values of n_d studied. The steady state cell voltage values for 0.4 A cm^{-2} (Fig. 7(a)), 0.5 A cm^{-2} (Fig. 7(b)), 0.6 A cm^{-2} (Fig. 7(c)) and 0.7 A cm^{-2} (Fig. 7(d)) exhibit monotonic trend for variation in n_d. This behavior can be attributed to increased membrane resistance, due to lower membrane water content as the rate at which

water is transported from anode to cathode increases. Also, it can be seen that degree of voltage undershoot is relatively smaller in Fig. 7(a) compared to that observed in Figs. 7(b), 7(c) and 7(d) owing to smaller current density with minima of 0.49 V for n_d = 1.3 (Fig. 7(a)), whereas voltage reversal occurs for n_d = 1.3 in other cases.

Following the same format in Fig. 7, Figs. 8(a) to (d) depict the change in cell potential over time for different values of water uptake in membrane as the current density is changed as a step from (a) 0.1 A cm^{-2} to 0.4 A cm^{-2}, (b) 0.1 A cm^{-2} to 0.5 A cm^{-2}, (c) 0.1 A cm^{-2} to 0.6 A cm^{-2} and (d) 0.1 A cm^{-2} to 0.7 A cm^{-2}, respectively. The water concentration in membrane, C_m^w, is a function of the membrane water content, λ, equivalent weight of membrane, *EW*, and density of the membrane, and is defined as $C_m^w = \frac{\rho\lambda}{EW}$. The effect of variation in membrane water content is studied by varying C_m^{w*} in Fig. 8, where C_m^{w*} is a dimensionless parameter, given by $C_m^{w*} = \frac{C_m^w}{\rho\lambda/EW}$. In the present study C_m^{w*} is varied from 0.8 to 1.2 for the cases described above. The above values are chosen to provide a systematic parametric study with a base of 1.0. The change in amount of water stored in the membrane can be achieved by changing the *EW*, λ, and density of membrane. The water content of the membrane, λ, is a function of water activity, a, which is function of temperature (Eq. 8). At high temperature, for a given concentration of water in gas, the amount of water stored in the membrane is lower, thus increasing the temperature during operation leads to lowering of water content in membranes. It can be seen from Fig. 8(a) that the increase in water uptake capacity leads to decrease in the amount of undershoot observed with a maximum undershoot for $C_m^{w*} = 0.7$. This can be attributed to increased amount of water to be removed by drag until back-diffusion rehydrates the membrane. Similar behavior is observed in Figs. 8(b), 8(c) and 8(d), with more pronounced undershoots, owing to higher current density. As seen from Figs. 8(a) and 8(b), no voltage reversal occurs for the values of C_m^{w*} studied, whereas voltage reversal occurs for $C_m^{w*} < 0.9$ and $C_m^{w*} < 1.1$ for step changes in current density from 0.1 to 0.6 A cm^{-2} (Fig. 8(c)) and from 0.1 to 0.7 A cm^{-2} (Fig. 8(d)), respectively. In Fig. 8(a) it can be seen that $C_m^{w*} = 0.5$ almost defines the limiting case for voltage reversal. Although, voltage reversal occurs for $C_m^{w*} = 0.8$, for a step change in current density from 0.1 A cm^{-2} to 0.6 A cm^{-2} (Fig. 8(c)), the cell voltage recovers upon rehydration, after a reversal period from t = 0.9 to 2.4 s. For higher water uptake values the observed undershoot is low and the cell reaches steady state following the expected initial instantaneous decrease in cell voltage, as illustrated

in Figs. 8 (a) to (d), with steady state cell voltage increasing monotonically with increase in water uptake. This behavior can be attributed to the improved conductivity of protons from anode to cathode.

Similar to the format in Figs. 7 and 8, Figs. 9(a) and (d) depict the change in cell potential

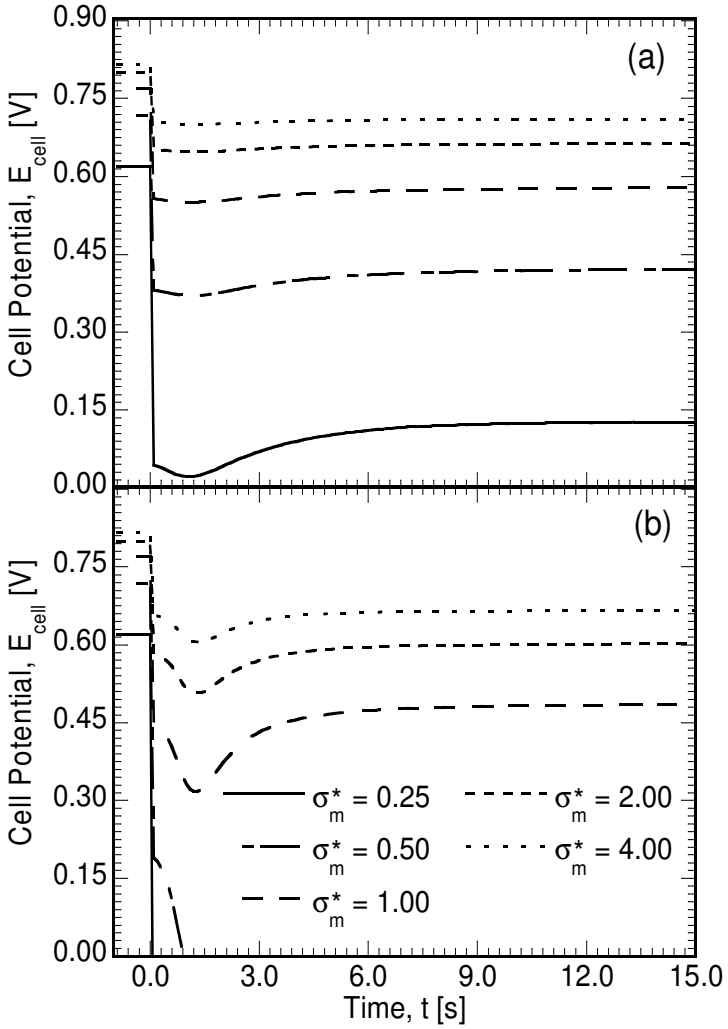

Figure 4.9: Transient variation in cell potential for various σ_m^*, for (a) 0.1 A/cm² to 0.4 A/cm² and (b) 0.1 A/cm² to 0.6 A/cm², respectively.

over time for different values of ionic conductivity of protons in membrane as the current density is changed as a step from (a) 0.1 A cm^{-2} to 0.4 A cm^{-2} and (b) 0.1 A cm^{-2} to 0.6 A cm^{-2}, respectively. The ionic conductivity of membrane, σ_m, is a function of the membrane water content, λ, and operating temperature, T, and is defined as

$\sigma_m = (0.005139\lambda - 0.00326)exp\left[1286\left(\frac{1}{303} - \frac{1}{T}\right)\right]$. The effect of variation in ionic conductivity of the membrane is studied by varying σ_m^* in Fig. 9, where σ_m^* is a dimensionless parameter, given by $\sigma_m^* = \frac{\sigma_m}{(0.005139\lambda - 0.00326)exp\left[1286\left(\frac{1}{303} - \frac{1}{T}\right)\right]}$. It can be seen from Fig. 9(a) that the steady state voltage increases with the increase in σ_m^*. It is also noted that for σ_m^* = 0.25 there is a significant drop in voltage upon step change in current density with the voltage almost reaching 0 before the anode region is replenished due to back diffusion. In contrast to the observation in Fig. 9(a) for step change in current density from 0.1 to 0.6 A cm^{-2} (Fig. 9(b)) the voltage reaches a value of 0 for σ_m^* = 0.25 and 0.50 owing to the dryout of the anode region. Similar to the observation in Fig. 9(a) it can be seen from Fig. 9(b) that the steady state voltage increases with the increase in σ_m^*.

It can be seen From Fig. 4 to 9 that the changes in diffusivity of water in the membrane, the electro-osmotic drag coefficient and ionic-conductivity of the membrane leads to significant changes in transient behavior for step change in current density. It is noted that the voltage reaches zero for n_d > 1.3, D_m^{w*} < 1.0 and approaches zero for σ_m < 0.50, whereas for other properties the transient variation in voltage is not as significant given the similar variations in values of the membrane property. It can be inferred from the discussion in Fig. 8 that increasing the water content of the membrane improves its dynamic behavior, in particular, with regard to the voltage reversal. It is noted that the anode region dries out rapidly owing to electro-osmotic drag, leading to increase in proton transport resistance, followed by rehydration through back-diffusion. This suggests that an improvement in the water storage capacity of the membrane near the anode would lead to an improved dynamic behavior, by avoiding complete dryout. One possible approach is a membrane design with graded water content, instead of constant water content, decreasing across its thickness from the anode to the cathode, which could prevent anode dryout, thus avoiding voltage reversal and possible damage to membrane. To explore this concept, the water uptake in the membrane is altered in the region of the membrane near the anode while keeping the water uptake capacity of rest of the membrane to a fixed value. The graded water uptake is denoted with $C_{m,1/4}^{w*}$, $C_{m,1/2}^{w*}$, $C_{m,3/4}^{w*}$ defining the water uptake capacity for 1/4th, 1/2 and 3/4th of the membrane thickness near the anode and $C_{m,0}^{w*}$ defining the water uptake capacity for the rest of the membrane. The changes in water content values affects the transport properties of the membrane and were accounted for in the simulations

accordingly. Figures 10(a) and (b) show the effect of change in water uptake capacity in the parts of membrane on the dynamic behavior, for $C_{m,0}^{w*} = 0.7$ and 0.9, respectively, given step change in current density form 0.1 to 0.7 A cm^{-2}. In each subplot, two different values of each of $C_{m,1/4}^{w*}$ and $C_{m,3/4}^{w*}$ are shown by the different lines. Although not shown in Fig. 10, changing the

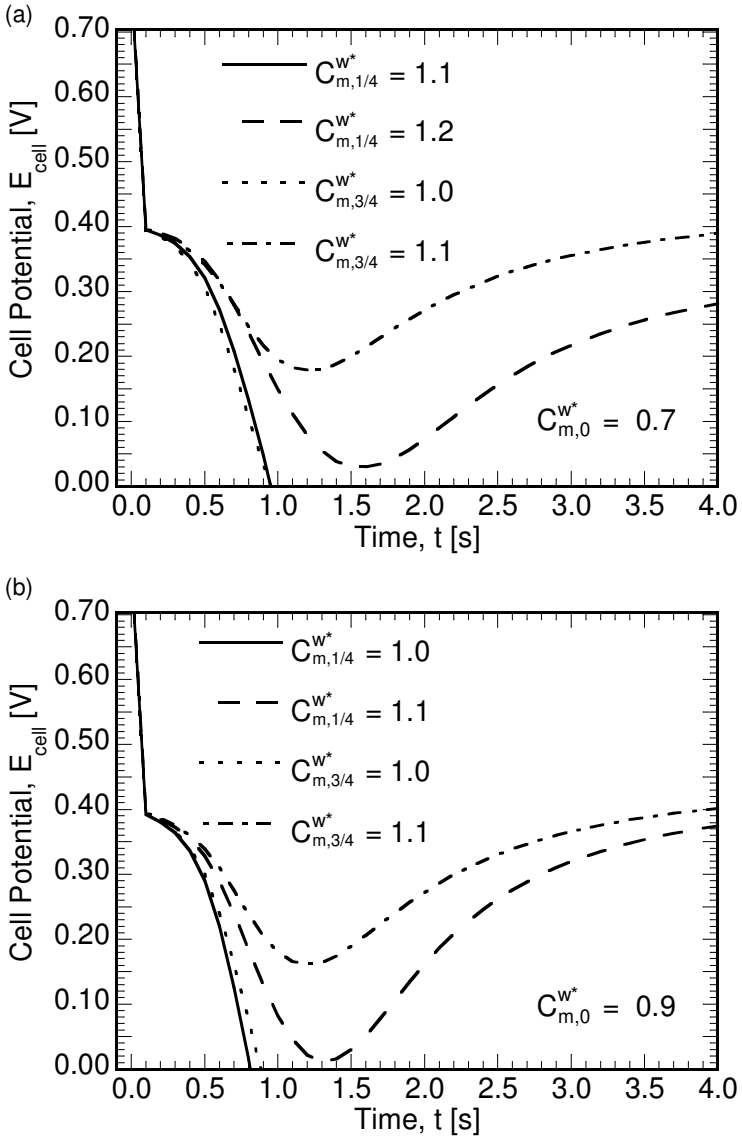

Figure 4.10: Transient variation in cell potential for graded design of membrane for (a) $C_{m,0}^{w*} = 0.7$, and (b) $C_{m,0}^{w*} = 0.9$, respectively.

water uptake capacity at the anode catalyst layer alone, with C_m^{w*} for rest of the membrane fixed to the $C_{m,0}^{w*}$ could not avoid voltage reversal, for the values of C_m^{w*} studied. It can be seen from Fig. 10(a) that, for $C_{m,1/4}^{w*} \leq 1.1$ the step change in current density leads to voltage reversal owing

to the anode dryout, whereas a further increase in uptake capacity, for $C_{m,1/4}^{w*} \geq 1.2$, the effects of back diffusion are dominant, avoiding voltage reversal. In comparison to that observed for $C_{m,1/4}^{w*}$ in Fig. 10(a), for $C_{m,3/4}^{w*}$ it can be seen that the cell voltage drops to zero for $C_{m,3/4}^{w*} \leq 1.0$ and can be avoided for $C_{m,1/2}^{w*} \geq 1.1$. For $C_{m,0}^{w*} = 0.9$, Figure 10(b) shows that in contrast to the

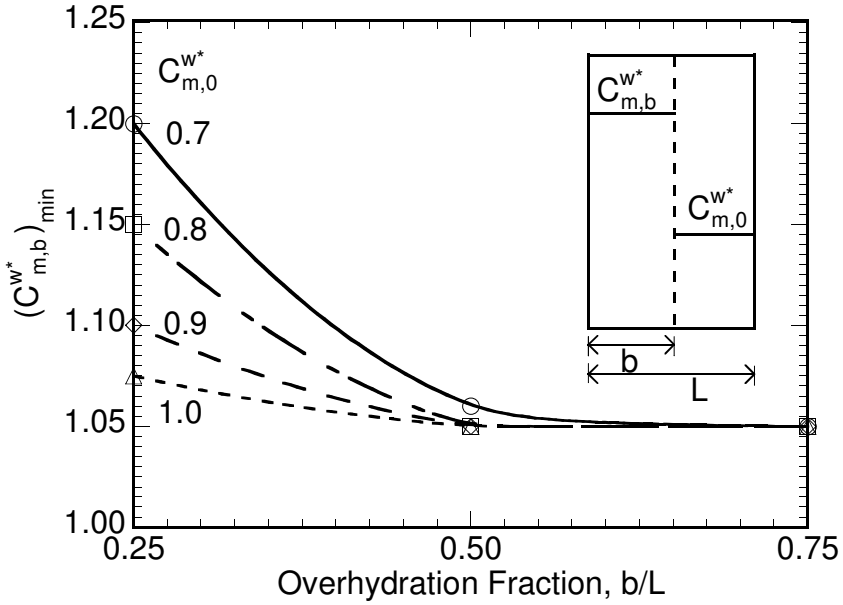

Figure 4.11: Variation in $(C_{m,b}^{w*})_{min}$ as a function of membrane overhydration fraction, b/L, for various $C_{m,0}^{w*}$.

observation for $C_{m,0}^{w*} = 0.7$ (Fig. 10(a)), there exists no voltage reversals for $C_{m,1/4}^{w*} \geq 1.1$. This behavior can be attributed to the increase in back diffusion rate owing to the increase in base water uptake capacity, $C_{m,0}^{w*}$. Similar to the observation for $C_{m,3/4}^{w*}$ in Fig. 10(a), it can be seen from Fig. 10(b) that the cell potential drops to zero for $C_{m,3/4}^{w*} \leq 1.0$, with no reversals observed for further increase in the water uptake. It is also noted from Fig. 10(b) that for there exists no voltage reversals for $C_{m,1/4}^{w*}$ and $C_{m,3/4}^{w*} \geq 1.1$, implying no considerable improvement in the dynamic behavior for improvements in C_m^{w*} beyond 1/4th of the membrane thickness.

From Fig. 10 it can be seen that there exists a minimum C_m^{w*}, $(C_{m,b}^{w*})_{min}$, for a given $C_{m,0}^{w*}$ and thickness in the membrane, such that the voltage reversal can be avoided. The variation of $(C_{m,b}^{w*})_{min}$ with the membrane overhydration fraction, *b/L* (see inset in Fig. 11), for $C_{m,0}^{w*}$ = 0.7, 0.8, 0.9 and 1.0, is presented in Fig. 11. It can be seen that there exists a considerable difference in the amount of over-hydration required to avoid voltage reversal for *b/L* = 0.25, for the different

values of $C_{m,0}^{w*}$. The cell voltage drops to zero for $C_{m,b}^{w*}$ < 1.20, 1.15, 1.10 and 1.075 for $C_{m,0}^{w*}$ = 0.7, 0.8, 0.9 and 1.0, respectively, as seen from the values of $(C_{m,b}^{w*})_{min}$. It is noted that the $(C_{m,b}^{w*})_{min}$ decreases monotonously with the increase in overhydration fraction, with no significant difference in the values of $(C_{m,b}^{w*})_{min}$ for b/L > 0.50. This behavior can be attributed to the effects of electro-osmotic drag being significantly dominant at near the anode region, and the improvements in the back diffusion rate with increase in C_m^{w*} along the length of the membrane. It is also noted that with the increase in $C_{m,0}^{w*}$, the difference in the $(C_{m,b}^{w*})_{min}$ drops significantly along the length of the membrane, as seen in Fig. 11.

The results presented in this section offer insight into the effects of various membrane properties on the hydration of the membrane during transient operation of fuel cells. Future work could include a study of various existing membranes, such as reinforced membranes, hydrocarbon membranes and others, using the present model. The effects of load change on mechanical behavior of membrane are also significant, as presented in Ref. [23] and could also be investigated for cases leading to anode dryout. The model can also be used to study the dry startup behavior of PEM fuel cells and to optimize operating parameters to improve performance as it closely emulates the actual load changes for automotive applications. Also, other factors such as reactant starvation during startups and load changes can lead to reversal in voltage and cause irreversible damage to the MEA [24] and can be studied in future. The combinations of water uptake explored in the present study serve as a proof of concept of a graded membrane design, and can be further optimized in a future work to suit desired performance characteristics. A more detailed study would be to solve an optimization problem to determine the optimized variation in uptake capacity for given load capacity or performance characteristics. By averting voltage reversals, the graded design of membrane also improves the operating range of the fuel cell to large current densities.

4.4 Nomenclature

A superficial electrode area [m^2]

C_k molar concentration of species k [mol m^{-3}]

D mass diffusivity of species [$m^2\ s^{-1}$]

E_{cell} cell potential or voltage [V]

EW equivalent weight of dry membrane [kg mol^{-1}]

F Faraday Constant [96,487 C $equivalent^{-1}$]

j transfer current [A m^{-3}]

K permeability [m^2]

n_d electro-osmotic drag coefficient [H_2O/H^+]

p pressure [bar]

R Universal gas constant [8.314 J $mol^{-1}\ K^{-1}$]

RH relative humidity

S source term in transport equations

T temperature [K]

$\vec{u}$ velocity vector

Greek letters

α transfer coefficient

ε porosity

η surface overpotential [V]

λ membrane water content

μ viscosity [kg $m^{-1}\ s^{-1}$]

ρ density [kg m^{-3}]

σ electronic conductivity [S m^{-1}], ionic conductivity [S m^{-1}]

τ shear stress [N m^{-2}]; tortuosity

ϕ phase potential [V]

Superscripts and subscripts

a	anode
c	cathode
$cell$	single fuel cell
e	electrolyte
eff	effective value
eq	equivalent
g	gas phase
in	inlet
k	species
m	membrane phase
0	t=0 s, initial state
ref	reference value
s	electronic phase
sat	saturated value
SS	steady state
t	time > 0 s
w	water

References

[1] C.Y. Wang, Chemical Reviews, 104 (2004) 4727-4766.

[2] M.L. Perry, T.F. Fuller, J. Electrochemical So., 149 (7) (2002), S59-67.

[3] J. Hamelin, K. Agbossou, A. Laperriere, F. Laurencelle, T.K. Bose, Int. J. Hydrogen Energy,

26 (6) (2001) 625–629.

[4] S. Kim, S. Shimpalee, J.W. Van Zee, J. Power Sources 135 (1/2) (2004) 110–121

[5] S. Kim, S. Shimpalee, J.W. Van Zee, J. Power Sources, 137 (1) (2004) 43–52.

[6] J. Benziger, E. Chia, J.F. Moxley, I.G. Kevrekidis, Chemical Engineering Science 60 (2005) 1743–1759.

[7] Q. Yan, H. Toghiani, H. Causey, J. Power Sources, 161(1) (2006) 492–502,

[8] S. Um, C. Y. Wang, K.S. Chen, J. Electrochemical So., 147 (12) (2000) 4485–4493.

[9] J.C. Amphlett, R.F. Mann, B.A. Peppley, P.R. Roberge, A. Rodrigues, J Power Sources, 61(1-2) (1996) 183-188.

[10] P.R. Pathapati, X. Xue, J. Tang, *Renewable Energy*, 30 (2005) 1-22

[11] X. Xue, J. Tang, A. Smirnova, R. England, N. Sammes, J Power Sources, 133(2) (2004) 188-204.

[12] M. Ceraolo, M. Miulli, A. Pozio, J Power Sources, 113(1) (2003) 183-188.

[13] Y. Wang, C.Y. Wang, *Electrochem. Acta*, 50 (2005) 1307-1315

[14] Y. Wang, C.Y. Wang, *Electrochem. Acta*, 51 (2005) 3924-3933

[15] P.W. Majsztrik, "Mechanical and Transport Properties of Nafion for PEM Fuel Cells; Temperature and Hydration Effects," (2008) *PhD Thesis*, *in: Chemistry*, Princeton University, Princeton, NJ

[16] T.A. Zawodzinski, T.E. Springer, F. Uribe, S. Gottesfeld, *Solid State Ionics*, 60 (1993) 199-221.

[17] Slade. S., Campbell, S.A., Ralph, T.R., Walsh, F.C., 2002, J. Electrochemical So., 149 (12) A1556-64.

[18] T.A. Zawodzinski, C. Derouin, S. Radzinski, R. Sherman, V.T. Smith, T.E. Springer, S. Gottesfeld, J. Electrochemical So., 140 (12) (1993) 1041-1047.

[19] Y. Zhang, A. Mawardi, R. Pitchumani, ASME J Fuel Cell Sc. and Tech. 3(4) (2006) 464-476

[20] R.B. Bird, W.E. Stewart, E.N. Lightfoot, Transport Phenomena, Wiley (1960) New York.

[21] T.E. Springer, T.A. Zawodzinski, S. Gottesfeld, 1991, J. Electrochemical So., 138 (8) 2334-2342.

[22] S. Motupally, A.J. Becker, J.W. Weidner, J. Electrochemical So., 147 (9) (2000) 3171-3177.

[23] A. Verma and R. Pitchumani, *J Fuel Cell Science and Technology*, In Press, 2014, DOI: 10.1115/1.4026551.

[24] A. Taniguchi, T. Akita, K. Yasuda, Y. Miyazaki, J. Power Sources 130 (2004) 42-49

[25] ANSYS® Academic Research, Release 14.0, Help System, Fluent® Theory Reference, ANSYS, Inc.

Table 4.1: Source terms in the governing equations

Domain	S_v	S_i	S_s , S_m
Gas channels	0	0	0
Diffusion layers	$-\frac{\mu}{K_{GDL}}\vec{u}$	0	0
Catalyst layers	$-\frac{\mu}{K_{GDL}}\vec{u}$	anode: $-\frac{j_a}{2F}$ $(i = H_2)$ *[1]* $(i = O_2)$ $-\nabla.\left(\frac{n_d i_e}{F}\right)$ $(i = H_2O)$	anode: $S_s = -j_a < 0$ $S_m = +j_a < 0$
		cathode: *0* $(i = H_2)$ $-\frac{j_c}{4F}$ $(i = O_2)$ $\frac{j_c}{2F} - \nabla.\left(\frac{n_d i_e}{F}\right)$ $(i = H_2O)$	cathode: $S_s = +j_c > 0$ $S_m = -j_c < 0$
Membrane	$-\frac{\mu}{K_{GDL}}\vec{u}$	0	0

Table 4.2. Geometrical and physical parameters used in the numerical simulations [8,9,14]

Parameter [units]	Symbol	Value
Gas channel depth [mm]		1.0
Diffusion layer thickness [mm]		0.3
Catalyst layer thickness [mm]		0.01
Membrane (N112) thickness [mm]		0.051
Fuel cell/ Gas channel length [mm]		100.0
Temperature [K]	T	353
Permeability of diffusion layer [m^2]	K_{GDL}	10^{-12}
Permeability of catalyst layer [m^2]	K_{CL}	10^{-15}
Gas diffusion layer porosity	ε_{GDL}	0.6
Catalyst layer porosity	ε_{CL}	0.4
Volume fraction membrane in catalyst layer	ε_m	0.26
Anode reference exchange current density [A/m^3]	$j_{a,ref}$	5.00×10^8
Cathode reference exchange current density [A/m^3]	$j_{c,ref}$	500
H_2 diffusivity membrane [m^2/s]	$D_{H_2,mem}$	2.59×10^{-10}
H_2 diffusivity in gas [m^2/s]	$D_{H_2,ref}$	1.1×10^{-4}
O_2 diffusivity in membrane [m^2/s]	$D_{O_2,mem}$	1.22×10^{-10}
O_2 diffusivity in gas [m^2/s]	$D_{O_2,ref}$	3.2348×10^{-5}
H_2O diffusivity in gas [m^2/s]	$D_{H_2O,ref}$	7.35×10^{-5}

Chapter 5: Investigation of Mechanical Behavior of Membrane in Polymer Electrolyte Fuel Cells Subject to Dynamic Load Changes

One of the major barriers for polymer electrolyte membrane (PEM) fuel cells to be commercially viable for stationary and transportation applications is the durability of membranes undergoing chemical and mechanical degradation over the period of operation. Toward understanding the effects of operating parameters on membrane durability, this chapter presents numerical simulations for a single channel PEM fuel cell undergoing changes in load, by subjecting a unit cell to step changes in voltage. The objective is to elucidate the mechanical response of membrane, which is subjected to hygral (water) loading and unloading cycles at constant temperature. Detailed three-dimensional (3D) computational fluid dynamics (CFD) simulations are conducted, taking in to account the complex interactions of water transport dynamics and load changes, to accurately capture the water content in the membrane with changes in cell voltage. The water content obtained through CFD simulations is, in turn, used to carry out two-dimensional (2D) finite element (FE) analysis to predict the mechanical response of the membrane undergoing cyclic change in water content, as the operating voltage is cycled. The effects of cyclic changes in cell potential on the stresses induced, amount of plastic strain and its localization are analyzed for various inlet cathode humidity values for two sections along the length of the fuel cell.

5.1 Introduction

PEM fuel cells (PEMFCs) are regarded as potential energy sources for mobile and stationary applications due to their clean, quiet and efficient operation. Due to their faster transient response and low-temperature operation, PEMFCs are better suited for automotive applications compared to other types of fuel cells. Improving the durability of membranes is one of the vital considerations for fuel cells to become a more viable option as power source in practical applications [1, 2].

The mechanical and chemical degradation processes affect the fuel cell performance and durability over the period of operation and are linked to the mechanical stresses induced due to swelling and shrinking of membranes, requiring careful examination [3]. Mechanical stresses arise as membrane swells (hydrates) or shrinks (dehydrates) as a function of moisture content

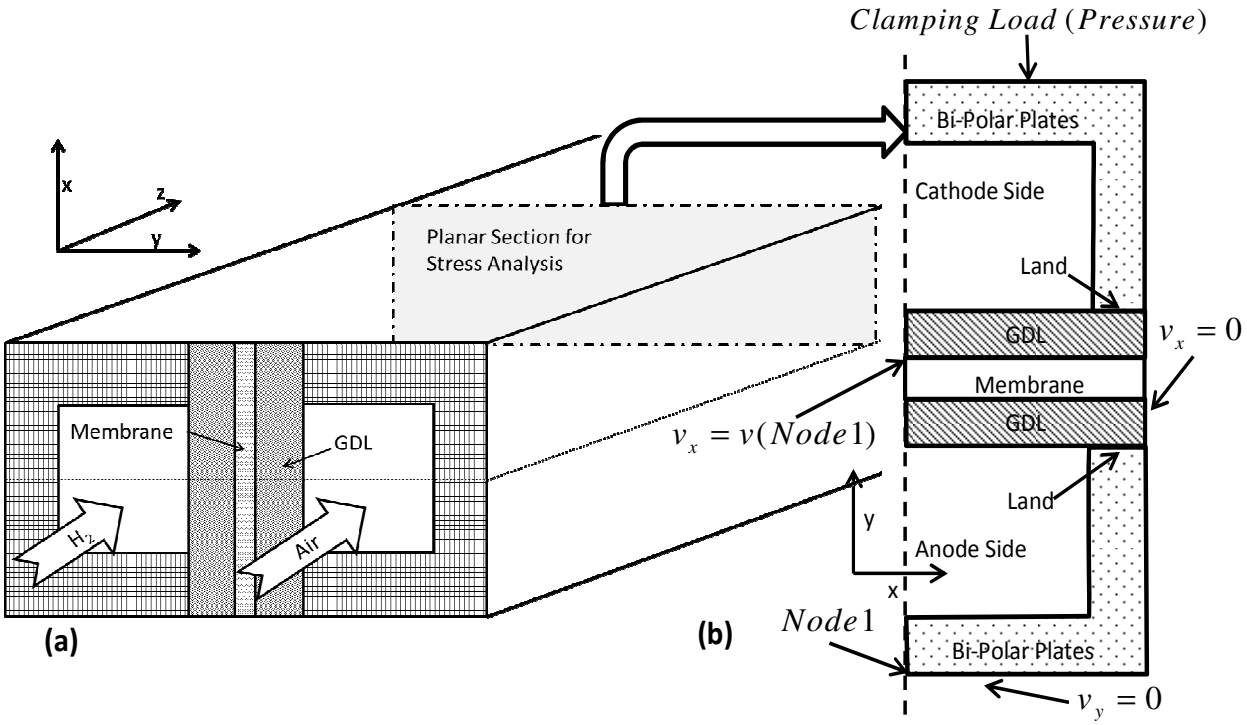

Figure 5.1: Schematic of a PEM fuel cell showing (a) a three-dimensional view of a single channel and (b) a planar half-section along the z-axis.

during the transient process. These stresses may exceed the material yield-limit causing the membrane to deform plastically, which, in turn, induces residual stresses, causes opening and propagation of cracks, and formation of pin-holes in the membrane or delamination between the membrane and the GDL, causing degradation [3-11]. One of the first numerical studies incorporating the effects of mechanical stresses on fuel cell was the work by Weber and Newman [8], which considered a one-dimensional analysis of a fuel cell and did not take in to account the property changes across layers of the fuel cell. Tang et al. [9] investigated the effects of stresses induced by swelling and thermal expansion on a uniformly hydrated membrane for different clamping methods, and suggested that the contribution by in-plane stresses are more significant than others. Kusoglu et al. [10,11] incorporated plastic deformation and anisotropy to demonstrate the residual stresses induced as the membrane is cycled through various uniformly distributed humidity loads. Kusoglu et al. [12] later incorporated the effects of non-uniform distribution of water in membrane, by specifying the water volume fraction at the membrane boundaries and solving for diffusion of water across the membrane.

The above-mentioned approaches [9–11] have been limited to either using uniform membrane hydration or simplistic water content profiles that do not take in to account the complex water distribution across length and thickness for realistic load changes. To address this limitation, in the present study, computational fluid dynamics (CFD) simulations are carried out to model the complex water transport dynamics for various load changes under different operating conditions and obtain membrane water content distribution across the fuel cell dimensions. The water content distribution, in turn, is used in a finite element analysis of a planar geometry of the membrane to calculate the localized stress and deformation in the membrane. Considering a step change in voltage for various operating conditions, causing the membrane to hydrate or dehydrate with non-uniform water content distribution, the objective of the coupled transport-structural analysis is to elucidate the mechanical behavior of membranes due to complex water transport dynamics under cyclic load changes. The mathematical model is presented in the next section, followed by a section on the presentation and discussion of the results of the study.

5.2 Mathematical Model

Figure 1(a) shows a schematic view of the three-dimensional section of a single channel PEM fuel cell with the z-axis along the channel length. Bipolar plates, gas channels, gas diffusion layers and catalyst layers on anode and cathode sides of a membrane constitute the different regions for this study. The three-dimensional schematic of single channel fuel cell shown in Fig. 1(a) forms the computational domain for the computational analysis, which is used to predict the water distribution in the membrane. Figure 1(b) shows a two-dimensional (2D) half-section of the single channel fuel cell in Fig. 1(a) along z-axis and forms the computational domain for the finite element hygroscopic stress analysis. The modeling for the water transport and the stress analysis are detailed in this section under two headings corresponding to each.

5.2.1 Water Transport Modeling

A comprehensive three-dimensional, single phase, transient, isothermal model is assumed following the assumptions in Ref. [1] to simulate the fuel cell dynamics, with the objective of determining the transient water content distribution in the membrane. The model takes into

consideration important transient processes such as gas transport, water accumulation, and electrochemical double layer discharge. A single-channel of the fuel cell forms the computational domain for this study. The equations governing the dynamics of fuel cell behavior are as follows [13,14]:

Continuity: $$\nabla.\vec{u} = 0 \quad (1)$$

Momentum: $$\frac{1}{\varepsilon}\left[\frac{\partial \vec{u}}{\partial t} + \frac{1}{\varepsilon}\nabla.(\vec{u}\vec{u})\right] = -\nabla.\left(\frac{p}{\rho}\right) + \nabla.\tau + S_u \quad (2)$$

Species: $$\varepsilon\frac{\partial C_k}{\partial t} + \nabla.(\vec{u}C_k) = \nabla.\left(D_k^{eff}\nabla C_k\right) + S_k \quad (3)$$

Charge Transport: $$\nabla.\left(\sigma_k^{eff}\nabla\phi_i\right) + S_i = 0; \quad i = s, m \quad (4)$$

A more detailed discussion about the water transport model can be found in Section 2.2.

5.2.2 Membrane Hygroscopic Stress Analysis

A brief description of the approach to incorporate the effects of swelling and de-swelling due to hydration and dehydration of the membrane, along with theory of the isotropic elasto-plasticity, is presented in this subsection. For a typical temperature distribution observed in the fuel cell, the thermal stresses are a fraction of the stresses induced due to swelling, thus isothermal condition is assumed. An isothermal plane strain model is incorporated to predict the strain and stress in the computational domain shown in Fig. 1(b). It is to be noted here that due to symmetry, the computational domain consists of only a half-section on the x–y plane and the full section along the z-axis. The total strain tensor, ε, is defined as the sum [10,11,18]:

$$\varepsilon = \varepsilon^{el} + \varepsilon^{pl} + \varepsilon^{S} \quad (9)$$

where superscripts el, pl and S represent the elastic-, plastic- and swelling-induced components of strain, respectively. The swelling due to hydration is represented as $\varepsilon^S = \beta(\mathrm{RH} - \mathrm{RH}^0)$ where β is the swelling-expansion coefficient, RH is the relative humidity and RH^0 is the reference relative humidity, which is taken to be 30% in this study. Assuming a linear response in the elastic region, the stress tensor, σ_{ij}, is obtained using the isotropic Hooke's law as:

$$\sigma_{ij} = \frac{E}{(1+\nu)(1-2\nu)}\left[\upsilon\delta_{ij}\varepsilon_{kk}^{el} + (1-2\nu)\varepsilon_{ij}^{el}\right] \quad (10)$$

where $\varepsilon_{kk}^{el} = \varepsilon_{xx}^{el} + \varepsilon_{yy}^{el} + \varepsilon_{zz}^{el}$, E is the Young's Modulus and υ is the Poisson's ratio. By virtue of the generalized plane strain state assumed, $\varepsilon_{xy} = \varepsilon_{yx} = \varepsilon_{xz} = \varepsilon_{zx} = 0$ and $\varepsilon_{zz} =$ constant. Considering a three-dimensional unit cell, the membrane is constrained along the planar section, as shown in Fig. 1(a) and 1(b), whereas no external forces or constraints are applied on

the membrane along the direction of flow, thus justifying the plane strain assumption. It is to be noted, however, that a more detailed three-dimensional study is required near the ends, where the assumptions may not hold. Incompressible plastic deformation with rate-independent plastic flow is assumed for the inelastic response. The von Mises yield function (J2-flow theory), is given by [10,11,16]:

$$f(\sigma_{ij}) = \sqrt{\frac{3}{2} S_{ij} S_{ij}} - \sigma_0 \tag{11}$$

where σ_{ij} represents the components of true stress tensor, and σ_0 is the yield strength, which is function of RH. The deviatoric stress S_{ij} is given as:

$$S_{ij} = \sigma_{ij} - \frac{1}{3}\sigma_{kk}\delta_{ij} \tag{12}$$

The material is assumed to be perfectly plastic, and yield is considered to occur when $f(\sigma_{ij}) = 0$ such that the material deforms elastically for $f(\sigma_{ij}) < 0$. According to the Mises flow theory [10,11,16], the plastic strain increment, $d\varepsilon^{pl}$, is given by $d\varepsilon_{ij}^{pl} = S_{ij} d\lambda$, implying proportionality to S_{ij}, where $d\lambda$ is a scalar proportionality factor. Results are presented in terms of equivalent plastic strain, ε_{eq}^{pl}, and von-Mises Stress (equivalent stress), σ_{eq}, which are computed as [12]:

$$\varepsilon_{eq}^{pl} = \int \sqrt{\frac{2}{3} d\varepsilon_{ij}^{pl} d\varepsilon_{ij}^{pl}} \tag{13}$$

$$\sigma_{eq} = \sqrt{\frac{3}{2} S_{ij} S_{ij}} \tag{14}$$

The change in RH is specified for each node, with the stress and strain tensor as unknowns. The schematic in Fig. 1(b) shows the boundary conditions used in the finite element modeling. A clamping force is applied to hold the stack together, resulting in a pressure of 1 MPa being applied on the upper surface of bipolar plate, as shown in Fig. 1(b). The bottom surface of the bipolar plate is constrained such that $v_y = 0$ and $v_x = 0$ at the right edge (Fig. 1(b)). A linear constraint $v_x(Node\ 1) - v_x^{N_2} = 0$ is applied along the left edges of the unit cell, where *Node 1* is the node at the bottom left in Fig. 1(b) and N_2 represents the remaining nodes on the left hand side. This condition constrains the left hand side to displace uniformly [10,11]. The material properties used for the stress analysis are given in Table 3 and 4, with Table 4 containing the *RH* dependent properties.

The three-dimensional CFD simulations give the water concentration at the membrane, which in turn provides the RH to be used as input for the FE analysis. It should be noted here

that the sections along the z-axis are taken at various lengths and are used for the FE analysis on two-dimensional slices. In general, the deformation of membrane affects the water transport through the membrane, and a coupled FE framework would be required to model the water transport and deformation simultaneously and is beyond the scope of present study. For simplicity, the RH is changed linearly from one steady state value to another steady state value locally. The membrane is pre-stressed before the load cycling by applying mechanical loading and changing the RH profile from a constant value ($RH \leq 30\%$), which defines the zero stress state for the present study, to that corresponding to E_{cell} = 0.8 V. The initial conditions used for the analysis are sequentially depicted in Table 5. The above model and boundary conditions are implemented in commercial FE analysis software, ANSYS® version 14.0, and solved using coupled-field ANSYS® Mechancial APDL solver [18], for above specified load changes. About 5000 elements are used to capture the detailed stress and strain profiles over different regions. The simulation time is dependent on the number of iterations require to get a converged solution and highly dependent on the levels of plastic deformation induced. The maximum time taken by a simulation is less than 30 minutes for each cycle on an Intel® Xeon™ Processor 3.33 GHz.

5.3 Results and Discussion

This section presents the results and discussion for the stresses and plastic deformation induced in the membrane due to changes in RH profiles, resulting from changes in voltage. The unit cell is cycled from E_{cell} = 0.80 V to each of E_{cell} = 0.50, 0.60, 0.65 and 0.70 V, and back to E_{cell} = 0.80 V, cycling the membrane humidity to the corresponding RH values. This, in turn, induces stresses as the membrane swells and de-swells, and plastic deformation in the cases where the stresses exceed the yield strength. The results are presented for planar sections taken at z = 0.01 m, 0.05 m and z = 0.09 m, with z = 0.0 m being the inlet and z = 0.1 m being the outlet.

Figure 2 shows the contour plots for RH in the membrane for $RH_c^{in} = 0\%$ at z = 0.01 m, with the top region of the membrane representing the cathode side and the bottom region representing the anode side. Figure 2(a) shows the humidification, RH, in membrane for E_{cell} = 0.80 V. It can be seen in Fig. 2(a) that the anode side of the membrane is more hydrated than the cathode side, resulting from the higher RH at the anode inlet ($RH_a^{in} = 100\%$) compared to 0%

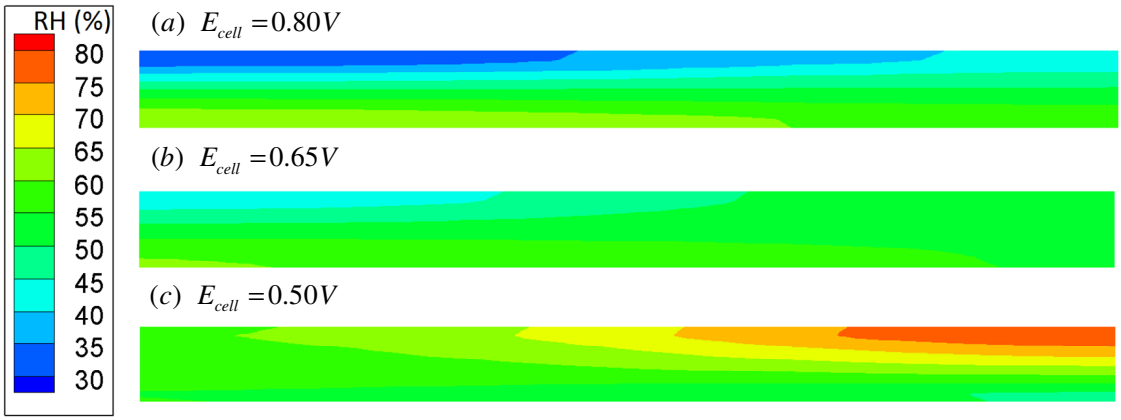

Figure 5.2: Contours of humidification, RH, at z = 0.01 m, for cycling from (a) E_{cell} = 0.80 V to (b) E_{cell} = 0.65 V and back to (c) E_{cell} = 0.50 V.

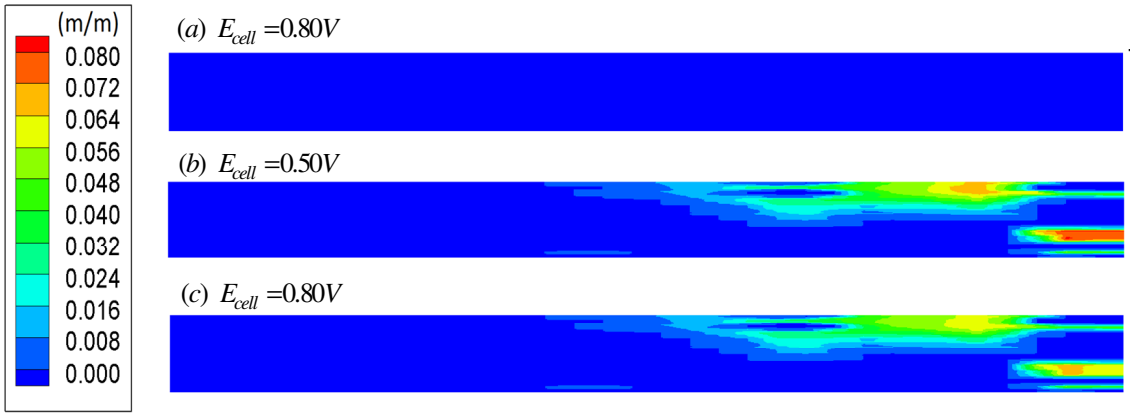

Figure 5.3: Contours of equivalent plastic strain, ε_{eq}^{pl}, for RH_c^{in} = 0%, at z = 0.01 m, for cycling from (a) E_{cell} = 0.80 V to (b) E_{cell} = 0.50 V and back to (c) E_{cell} = 0.80 V.

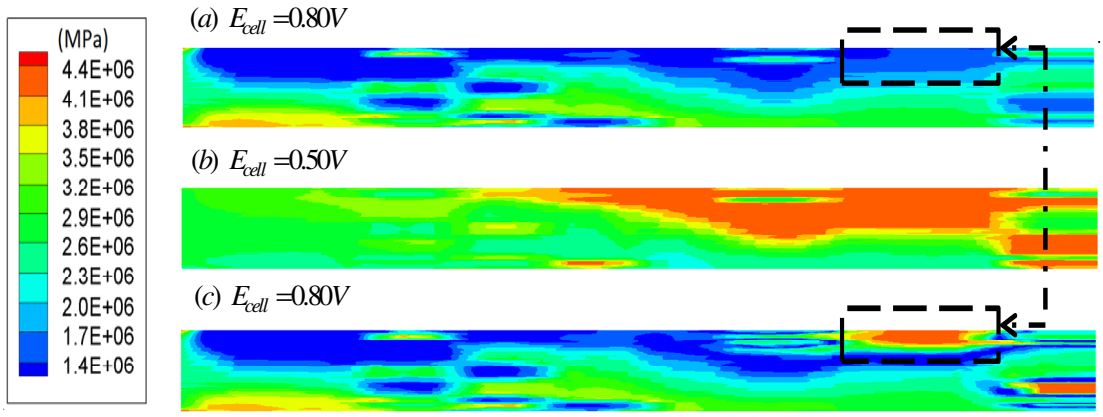

Figure 5.4: Contours of von-Mises Stress (equivalent stress), σ_{eq}, at z = 0.01 m, for cycling from (a) E_{cell} = 0.80 V to (b) E_{cell} = 0.50 V and back to (c) E_{cell} = 0.80 V.

humidity at the cathode inlet (RH_c^{in}). Figure 2(b) shows the humidity profile for E_{cell} = 0.65 V. With the increased current density at 0.65 V, the membrane hydration increases along its length, resulting in higher RH values compared to that for E_{cell} = 0.80 V (Fig. 2(a)). Figure 2(c) shows the humidity profile for E_{cell} = 0.50 V. Lowering the voltage to 0.5 V further increases the current density, resulting in the humidity gradient to be directed from cathode to anode, implying higher RH values at the cathode side compared to that observed for 0.80 and 0.65 V in Fig. 2(a) and 2(b), respectively. Also the region near the land (Fig. 1(b)) in Fig. 2(c) is found to have maximum RH as compared to the corresponding locations in Fig. 2(a) and Fig. 2(b).

Figure 3 depicts the contour plots for equivalent plastic strain, ε_{eq}^{pl}, as the membrane is cycled from E_{cell} = 0.80 V (Fig. 3(a)) to 0.50 V (Fig. 3(b)) and back to 0.80 V (Fig. 3(c)). Figure 3(a) shows the ε_{eq}^{pl} contours for E_{cell} = 0.80 V, at the beginning of the cycle. As the membrane swells owing to increase in water content, compressive stresses are induced and if the stresses exceed the yield strength, it leads to a plastic deformation in the membrane. The stresses corresponding to the strain in Fig. 3 are depicted in Fig. 4, with Fig. 4(a) showing the von-Mises stress, or as referred to in this work as equivalent stress, σ_{eq}, for the corresponding strain in Fig. 3(a). It can been seen in Fig. 3(a) that no plastic strain occurs for the RH loading specified in Fig. 2(a), as the stresses do not reach the yield limit. Figure 3(b) shows the ε_{eq}^{pl} contours for E_{cell} = 0.50 V, as the load is changed from E_{cell} = 0.80 V to E_{cell} = 0.50 V, changing the RH loading to what is seen in Fig. 2(c). It can be seen that the membrane undergoes plastic deformation at regions of high swelling namely, at the cathode side near the land region. This can be attributed to the high RH values near the land region at the cathode side, as seen in Fig. 2(c). It is also noted from Fig. 3(b) that the plastic strain induced is highly non-uniform along the thickness and width of the membrane. As the membrane is cycled back to 0.80 V the RH loading changes from what is seen in Fig. 2(c) to that in Fig. 2(a), thus de-swelling the membrane. Figure 3(c) shows the ε_{eq}^{pl} contours, after the load is changed back to 0.80 V from 0.50 V. Localized plastic deformation of the membrane causes the redistribution of stresses and thus changing the profile of plastic strain locally and can be seen in Fig. 3(c).

Figure 4 represents contours of the von-Mises (equivalent) stress, σ_{eq}, for the load cycle discussed above (Fig. 3), with Figs. 4(a)–(c) corresponding to the strains observed in Fig. 3(a)–(c). Figure 4(a) shows the variation of σ_{eq} for an initial load of 0.80 V, for which the membrane

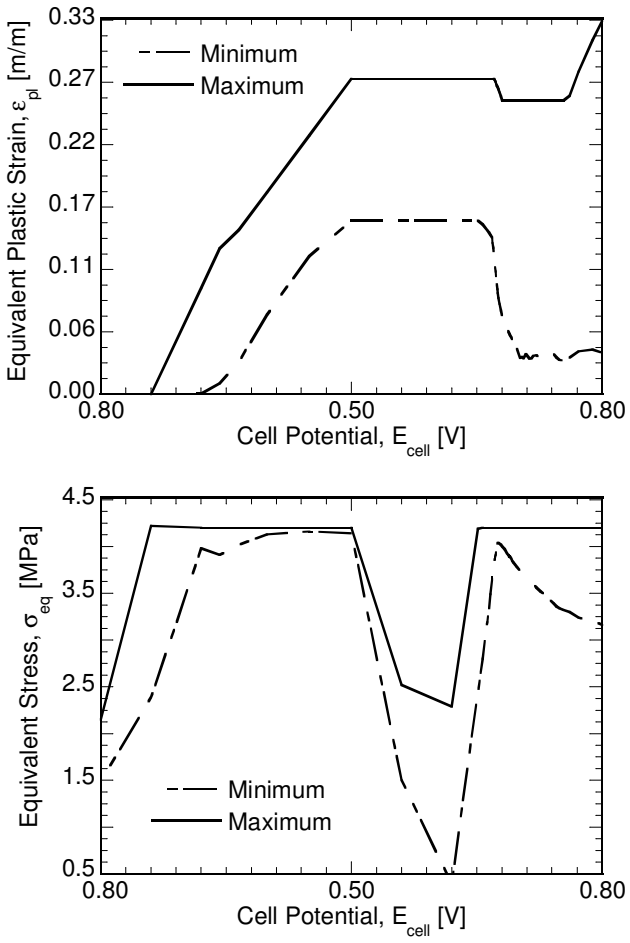

Figure 5.5: Variation in maximum and minimum values of (a) equivalent plastic strain and (b) equivalent stress with the cell voltage, E_{cell}, at z = 0.09 m.

deforms elastically since the stresses are below the yield limit. It can be seen that maximum stress occurs in the anode region where the RH is maximum (Fig. 2(a)). Figure 4(b) shows the stress, σ_{eq}, for a change in load from 0.80 V to 0.50 V. In contrast to the observation in Fig. 4(a), it can be seen in Fig. 4(b) that the part of the membrane near cathode land reaches yield-limit and deforms plastically (Fig. 3(b)). It is noted here that the equivalent stress at the plastically deformed regions are not fixed to a single value, but since the yield strength is a function of RH, we see a distribution of yield stress values, implying that the membrane undergoes plastic deformation over a range of RH values. Also, with plastic deformation, the stresses are redistributed locally, further changing the profile of equivalent stress across the membrane. Consequently, the best way to represent the plastically deformed region is through ε_{eq}^{pl}, indicating plastic deformation for non-zero values.

Figure 4(c) shows the stresses after the membrane is cycled back to the RH corresponding to 0.80 V (Fig. 2(a)). As the membrane dehydrates, owing to the change in the RH profile to that in Fig. 2(a), there is a reduction in the compressive stresses, as seen in Fig. 4(c). Due to plastic deformation (yielding) at loading, the unloading results in residual tensile stresses being developed locally in the regions of plastic deformation. This is exemplified by the box drawn comparing the stresses in Fig. 4(a) at the start of the cycle, before loading, and in Fig. 4(c) after unloading. It can be seen in Fig. 4(c) that the stresses developed upon unloading can reach significantly high values. These residual stresses can lead to further plastic deformation if they exceed the yield limit, and can, in turn, contribute to the degradation of the membrane.

While Fig. 4 discussed the contours of ε_{eq}^{pl} and σ_{eq} induced in the membrane near the inlet region (z = 0.01 m), Figure 5 shows the variation in maximum and minimum ε_{eq}^{pl} (Fig. 5(a)) and σ_{eq} (Fig. 5(b)), at z = 0.09 m (near the outlet region), for the load cycle specified for Fig. 4. The water generated at the cathode catalyst layer gets redistributed along the length through the transport mechanisms discussed previously. This leads to an increase in RH at z = 0.09 m, thus affecting the mechanical behavior of the membrane along the length of the fuel cell. Figure 5(a) shows the variation in maximum and minimum ε_{eq}^{pl} for the membrane section at z = 0.09 m. In Fig. 5(a) it can be seen that, for 0.80 V, at the beginning of cycle, there exists no plastic strain. With increase in load, the membrane goes through plastic deformation due to compressive stresses, owing to swelling, and the strain increases till the maximum load is reached at 0.50 V. Unlike the observation in Fig. 3(b), it is noted in Fig. 5(a) that the entire membrane deforms plastically, as seen by the increase in minimum plastic strain from 0 at 0.80 V to 0.17 (approx.) at 0.50 V. Thus, water produced along the length is redistributed such that the water content at the end of channel is maximized, swelling the entire section of the membrane at z = 0.09 m, causing it to deform plastically. After unloading, marked by a change in the cell potential from 0.50 V to 0.80 V, it can be seen that membrane undergoes further plastic deformation, reaching a maximum after unloading. This can be explained as the occurrence of plastic deformation due to tensile stretching upon unloading.

Figure 5(b) shows the variation of maximum and minimum σ_{eq} for the corresponding plastic strain presented in Fig. 5(a). It can be seen that both minimum and maximum stress

values increase with the increase in load. The maximum stress increases with increase in load

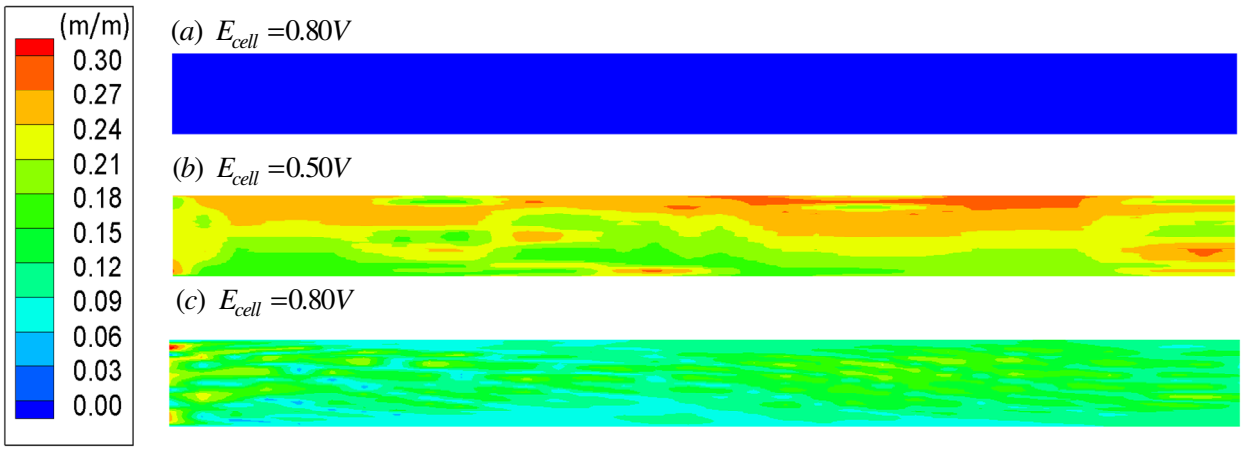

Figure 5.6: Contours of equivalent plastic strain, ε_{eq}^{pl}, at z = 0.09 m, for cycling from (a) E_{cell} = 0.80 V to (b) E_{cell} = 0.50 V and back to (c) E_{cell} = 0.80 V.

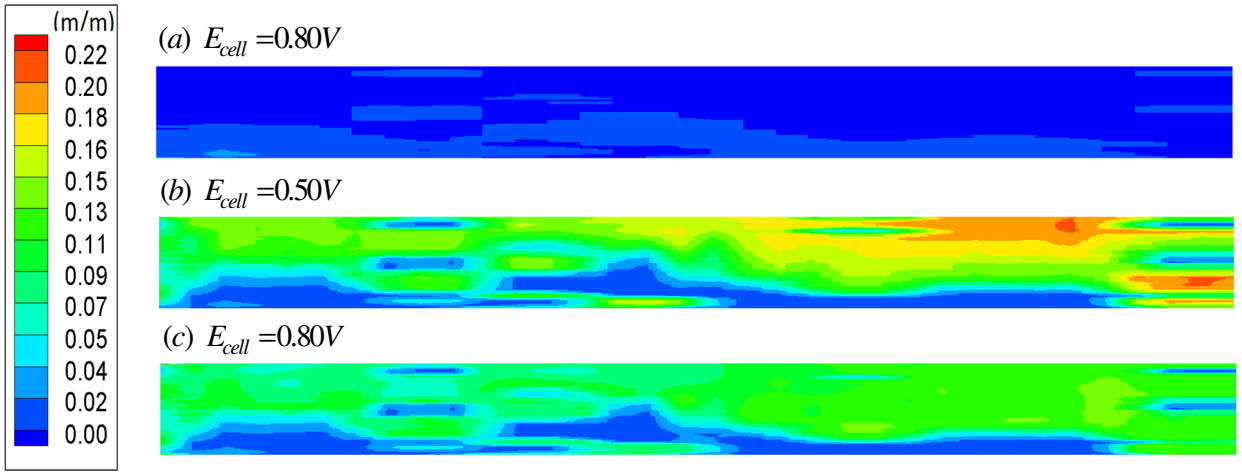

Figure 5.7: Contours of equivalent plastic strain, ε_{eq}^{pl}, for RH_c^{in} = 25%, at z = 0.01 m, for cycling from (a) E_{cell} = 0.80 V to (b) E_{cell} = 0.50 V and back to (c) E_{cell} = 0.80 V.

reaching

a yield point, implying the onset of plastic deformation of membrane, as seen in Fig. 5(b). It is evident from Figs. 5(a) and 5(b) that a part of membrane reaches the yield limit at the later part of the loading cycle, as seen by the minimum stress reaching the yield limit implying the onset of plastic deformation. Although the entire membrane goes though plastic deformation, the minimum and maximum stresses obtained are different, which can be attributed to the dependence of the yield strength on RH. Hence, the regions with higher RH have lower yield

strength and deform plastically at lower stresses. Upon unloading from 0.50 V, the compressive stresses decrease, as marked by a decrease in the both the maximum and minimum equivalent stresses in Fig. 5(b). As the membrane is a further unloaded, residual tensile stress develops, marked by the corresponding increase in the equivalent stress. The residual stress reaches the yield limit, as seen in Fig. 5(b), causing the membrane to deform plastically as a result of unloading. Consequently, cycling through high loads induces further plastic deformation in cases where residual stresses exceed yield limit, and can lead to further degradation of the membrane.

Figure 6 shows the contours of the equivalent plastic strain, ε_{eq}^{pl}, for z = 0.09 m, for the load cycle discussed in Fig. 3. Figure 6(a) presents the plastic strain for 0.80 V, before loading, and shows that the membrane deforms elastically with no plastic strain. It is noted here that at the outlet region, the low loads (E_{cell} = 0.80 V) do not lead to sufficient water generation, due to the low current density, to cause plastic deformation. Figure 6(b) shows ε_{eq}^{pl} for 0.50 V after loading from 0.80 V. In contrast to the observation in Fig. 3(b), upon loading, the entire membrane deforms plastically. It is also noted in Fig. 6(b) that the maximum strain is induced on the cathode side of the membrane, owing to the higher humidification at the cathode region. Figure 6(c) shows the plastic strain contours after unloading from 0.50 V. It was noted in Fig. 5 that the membrane undergoes further plastic deformation upon unloading, owing to the development of residual stresses. Hence, a higher value of plastic strain is evident in Fig. 6(c) in certain regions of the membrane, compared to that seen in Fig. 6(b). It can also be seen in Fig. 6(c) that the strains are more homogenized, which can be attributed to a redistribution of stresses upon plastic deformation.

Figure 7 portrays the contours of ε_{eq}^{pl} at z = 0.01 m (near the inlet) and for RH_c^{in} = 25%, for cyclic loading of cell from (a) 0.80 V to (b) 0.50 V and back to (c) 0.80 V. It can be seen in Fig. 7(a) that at the beginning of cycle before loading (E_{cell} = 0.80 V), the plastic strain is not 0, unlike that observed in Fig. 3(a) and Fig. 6(a). This suggests that under higher inlet humidification, the membrane undergoes plastic deformation at the lower loads (such as E_{cell} = 0.80 V). The plastic deformation for E_{cell} = 0.80 V occurs dominantly on the anode side of the membrane, in contrast to the observation for the higher loads (E_{cell} = 0.50 V) in Fig. 3(b) and 6(b), where the plastic deformation is more prominent on the cathode side of the membrane. This behavior can be

attributed to the higher water content on the anode side near the inlet region, owing to the low current density. Figure 7(b) shows the plastic strain for E_{cell} = 0.50 V upon loading from 0.80 V. In comparison to the observation in Fig. 3(b), it can be seen that all of the membrane deforms plastically due to the higher water content, owing to the increased inlet humidity ($RH_c^{in} = 25\%$) in comparison to that of $RH_c^{in} = 0\%$ in Fig. 3. It is also noted in Fig. 7(b) that the maximum strain occurs at the location of maximum humidity, which is at the cathode side of the membrane. Figure 7(c) shows ε_{eq}^{pl} upon unloading from 0.50 V. Unlike in Fig. 6(c), the strain contours in Fig. 7(c) do not show regions of high plastic strain upon unloading, due to the additional strain associated with the residual stresses. It is also noted that, as the stresses get redistributed in the membrane undergoing plastic deformation, the profiles are more homogenized as discussed earlier for Fig. 6(c).

While the discussion so far focused on the variations in ε_{eq}^{pl} at a given section for two different relative humidity at the cathode inlet, $RH_c^{in} = 0\%$ and 25%, it is instructive to examine the variation in maximum ε_{eq}^{pl} and V^{pl}as a function of load change for various RH_c^{in}, where V^{pl} represents the percentage volume of the membrane at a given section undergoing plastic deformation, with V^{pl}= 0% representing no plastic strain in the membrane and V^{pl}= 100% implying that the entire membrane goes through plastic deformation at that particular section. Three sections are considered for the study: (1) at the near inlet region given by z = 0.01 m, (2) at the middle of the length of fuel cell, z = 0.05 m, and (3) at the near outlet region, z = 0.09 m, to elucidate the effects of load change and inlet relative humidity on the mechanical behavior of the membrane.

Figure 8 shows the variation of maximum ε_{eq}^{pl} (Fig. 8(a)) and V^{pl} (Fig. 8(b)) as a function of voltage change, ΔE_{cell}, from E_{cell} = 0.80 V for various RH_c^{in} at the near inlet region, z = 0.01m. The load changes depicted by ΔE_{cell} = 0.10 V, 0.15 V, 0.20 V and 0.30 V represent the change in voltage from E_{cell} = 0.80 V to 0.70 V, 0.65 V, 0.60 V and 0.50 V, respectively, and back to 0.80 V. The value of the maximum equivalent plastic strain at the end of the cycle is presented as a function of ΔE_{cell}. Figure 8(a) depicts the variation in maximum ε_{eq}^{pl} as a function of load change for various RH_c^{in}. It can be seen from Fig. 8(a) that the maximum plastic strain shows a monotonic increase as the change in load (ΔE_{cell}) is increased, with the maximum strain

occurring for a change from 0.80 V to 0.50 V. This behavior can be attributed to increased water content with increase in current density, as the voltage is lowered. Also, for $RH_c^{in} = 0\%$ in Fig. 8(a), the membrane deforms plastically for ΔE_{cell} > 0.20 V, whereas for $RH_c^{in} \geq 10\%$, the

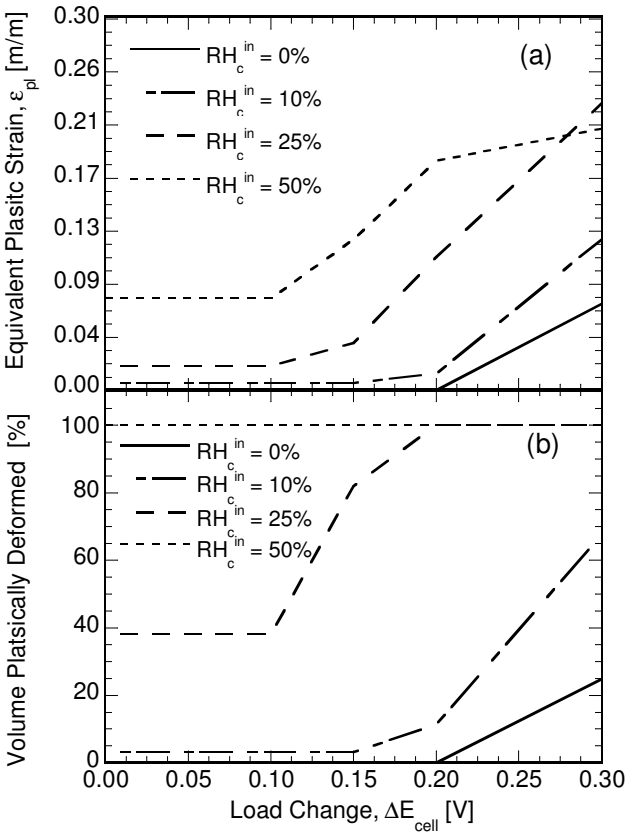

Figure 5.8: Variation in maximum (a) equivalent plastic strain, $\boldsymbol{\varepsilon_{eq}^{pl}}$, and (b) volume percentage of plastic deformation, $\boldsymbol{V^{pl}}$, as a function of change in cell potential, $\boldsymbol{\Delta E_{cell}}$, for various cathode inlet relative humidity, $\boldsymbol{RH_c^{in}}$, at z = 0.01m.

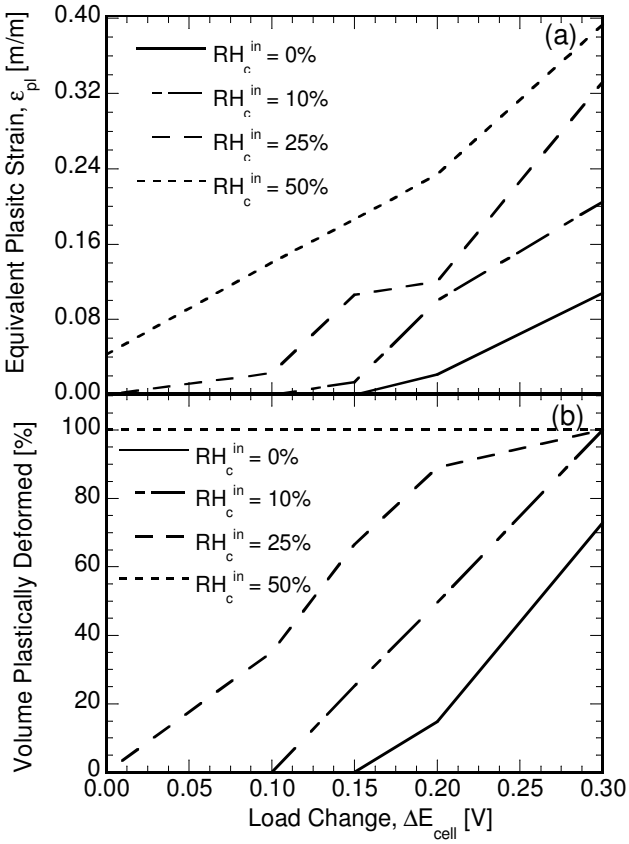

Figure 5.9: Variation in maximum (a) equivalent plastic strain, $\boldsymbol{\varepsilon_{eq}^{pl}}$, and (b) volume percentage of plastic deformation, $\boldsymbol{V^{pl}}$, as a function of $\boldsymbol{\Delta E_{cell}}$, for various $\boldsymbol{RH_c^{in}}$, at z = 0.05m.

membrane shows plastic deformation at base load (0.80 V). It is noted here that the increase in plastic strain for ΔE_{cell} = 0.10 V from that observed for base load (ΔE_{cell} = 0 V) is negligible in comparison to the increase in plastic strain for the larger load changes ($\Delta E_{cell} \geq$ 0.15 V). This can be attributed to relatively small increase in the current production rate for E_{cell} = 0.70 V compared to that of E_{cell} = 0.80 V. For $RH_c^{in} = 10\%$, a significant increase in plastic deformation is noted for ΔE_{cell} > 0.2 V, whereas the same occurs for ΔE_{cell} > 0.1 V for RH_c^{in} = 25% and 50%. It

is also seen that the maximum ε_{eq}^{pl} (Fig. 8(a)) increases with the increase in RH_c^{in}, for $\Delta E_{cell} \leq$ 0.25 V, owing to the increase in membrane humidification with increase in RH_c^{in}, whereas the amount of plastic strain at $RH_c^{in} = 25\%$ is higher than that for $RH_c^{in} = 50\%$, for a given ΔE_{cell} = 0.30 V. This can be attributed to the dominant effect of electro-osmotic drag at the near inlet region leading to decrease in the water content values and thus the amount of plastic strain.

While the amount of plastic strain induced for a given load change can be ascertained from Fig. 8(a), it does not elucidate on the percentage of membrane that undergoes plastic deformation for the prescribed load change. Hence, V^{pl} is used a guiding parameter to represent the overall membrane characteristic. Figure 8(b) shows the variation in V^{pl} as a function of load change (ΔE_{cell}) for various values of inlet humidification. Similar to the observation for ε_{eq}^{pl} in Fig. 8(a), the value of V^{pl} increases with the increase in load change, as seen in Fig. 8(b). It can see that almost 25% of the membrane undergoes plastic deformation for ΔE_{cell} = 0.30 V, at $RH_c^{in} = 0\%$, whereby V^{pl} increases significantly with the increase in inlet relative humidity, with the entire membrane undergoing plastic deformation for $RH_c^{in} > 25\%$. Similar to the observation in Fig. 8(a), it is noted from Fig. 8(b) that the increase in V^{pl} (for ΔE_{cell} = 0.10 V) from that for base load (ΔE_{cell} = 0 V), is negligible in comparison to the increase for the higher load changes ($\Delta E_{cell} \geq$ 0.15 V). It can be seen that the entire membrane undergoes plastic deformation at RH_c^{in} = 50% for all load cycles, whereas at RH_c^{in} = 25% this is observed for $\Delta E_{cell} \geq$ 0.20 V. Thus, near the inlet region, higher inlet humidification values lead to total plastic deformation of membrane at lower loads. Also, high loads lead to significant plastic deformation of membrane at low inlet humidification values. It can be seen that Figs. 8(a) and 8(b) provide a complete picture of the membrane behavior upon loading and unloading, and can be used to design operating windows presenting the limits on RH and ΔE_{cell}.

The mechanical behavior of the membrane at the mid-section along the length of fuel cell, z = 0.05 m, is presented in Fig. 9. Figure 9(a) depicts the variation in maximum ε_{eq}^{pl} as a function of load change for various RH_c^{in}. It can be seen from Fig. 9(a) that the maximum plastic strain increases monotonically as the change in load (ΔE_{cell}) is increased, with the maximum strain occurring for a change from 0.80 V to 0.50 V. In contrast to the observation in Fig. 8(a), it can be seen from Fig. 9(a) that for $RH_c^{in} = 0\%$, there exists no plastic strain for $\Delta E_{cell} \leq$ 0.15 V, whereas

ε_{eq}^{pl} = 0 for $\Delta E_{cell} \leq$ 0.20 V in Fig. 8(a). Similar to the observation in Fig. 8(a), the equivalent plastic strain, ε_{eq}^{pl} increases with the increase in load change for all the values of RH_c^{in} studied. The maximum ε_{eq}^{pl} is obtained for ΔE_{cell} = 0.30 V at $RH_c^{in} = 50\%$, whereas near the inlet region (Fig. 8(a)), the maximum occurs at $RH_c^{in} = 25\%$. It can be seen from Fig. 9(a) that there is considerable increase in ε_{eq}^{pl} for ΔE_{cell} = 0.10 V, from that observed for the base load (ΔE_{cell} = 0 V), compared to the corresponding value in Fig. 8(a). It is also noted that there is significant increase in the maximum ε_{eq}^{pl} from 0.21 m/m at z = 0.01 m (Fig. 8(a)) to ~0.40 m/m at z = 0.05 m (Fig. 9(a)).

Figure 9(b) shows the variation in V^{pl} as a function of load change (ΔE_{cell}) for various values of inlet humidification. As noted for ε_{eq}^{pl} in Fig. 9(a), V^{pl} is seen in Fig. 9(b) to increase with the increase in load change. In contrast to the observation in Fig. 8(b), it can be seen that for RH_c^{in}= 25%, V^{pl} reaches 100% at ΔE_{cell} = 0.30 V, whereas this occurs for ΔE_{cell} = 0.20 V at the near inlet region (Fig. 8(b)). Also, a considerable increase in ε_{eq}^{pl} is seen for ΔE_{cell} = 0.30 under low humidity conditions ($RH_c^{in} = 0\%$). It is evident from Fig. 9 that there is significant increase in the amount of plastic strain induced and the volume of the membrane that undergoes plastic deformation at its mid-section, compared to that seen in Fig. 8 at the near inlet region, owing to the increased hydration of membrane along the length of the fuel cell by the water generated at the cathode catalyst layer. Similar trends, as seen in Figs. 8 and 9 are observed for the behavior of ε_{eq}^{pl} and V^{pl} at the near outlet region (z = 0.09 m) with an increase in ε_{eq}^{pl} and V^{pl} at the various loads, also owing to the increased hydration. However, unlike in Figs. 8 and 9, at z = 0.09 m, entire membrane undergoes plastic deformation (V^{pl} = 100%), for ΔE_{cell} = 0.30 V.

The results discussed in this article illustrate the localization of stresses and strain and their dependency on inlet humidification and load changes. Future work could include a study of the combine effects of other operating parameters on the mechanical behavior. In addition, the impact of complex membrane properties such as anisotropy, strain hardening and creep is worthy of assessment using the present approach. Also, the effects of deformation on the fuel cell performance can be included in the current model for a more comprehensive analysis.

5.4 Nomenclature

A	superficial electrode area [m^2]
C_k	molar concentration of species k [mol/m^3]
D	mass diffusivity of species [m^2/s]
E_{cell}	cell potential or voltage [V]
EW	equivalent weight of dry membrane [kg/mol]
F	Faraday constant [96,487 C/equivalent]
j	transfer current [A/m^3]
K	permeability [m^2]
n_d	electro-osmotic drag coefficient [H_2O/H^+]
p	pressure [bar]
R	gas constant [8.314 J/mol K]
RH	relative humidity
S	source term in transport equations
T	temperature [K]
$\vec{u}$	velocity vector
v	displacement

Greek letters

α	transfer coefficient
ε	porosity; strain
η	surface overpotential [V]
λ	membrane water content; proportionality scalar
μ	viscosity [kg/m s]
ρ	density [kg/m^3]
σ	electronic conductivity [S/m]; stress
τ	shear stress [N/m^2]; time constant; tortuosity
ϕ	phase potential [V]

Superscripts and subscripts

a	anode

c	cathode
$cell$	single fuel cell
e	electrolyte
el	elastic
eff	effective value
eq	equivalent
g	gas phase
in	inlet
k	species
m	membrane phase
0	t = 0 s, initial state
pl	plastic
ref	reference value
s	electronic phase
S	swelling
sat	saturated value
SS	steady state
t	time > 0 s
w	water

References

[1] Wang, C.Y., 2004, "Fundamental Models for Fuel Cell Engineering," *Chemical Reviews*, **104**, pp. 4727-4766.

[2] Perry, M.L., Fuller, T.F., 2002, "A Historical Perspective of Fuel Cell Technology in the 20th Century," *J. Electrochemical So.*, **149 (7)**, pp. S59-67.

[3] Borup, R., Meyers, J., Pivovar, B., Kim, Y. S., Mukundan, R., Garland, N., Iwashita, N., et al., 2007, "Scientific aspects of polymer electrolyte fuel cell durability and degradation," *Chemical Reviews-Columbus*, **107(10)**, 3904-3951.

[4] Stanic, V., Hoberecht, M., 2004, "Mechanism of Pin-hole Formation in Membrane Electrode Assemblies for PEM Fuel Cells," *4th International Symposium on Proton Conducting Membrane Fuel Cells*, October.

[5] Liu, W., Ruth, K., and Rusch, G., 2001, "Membrane Durability in PEM Fuel Cells," *J. New Mater. Electrochem. Syst.*, **4**, pp. 227—231.

[6] P. Gode, J. Ihonen, A. Strandroth, H. Ericson, G. Lindbergh, M. Paronen, F.Sundholm, G. Sundholm, N. Walsby, 2003, "Membrane durability in a PEM fuelcell studied using PVDF based radiation grafted membranes," Fuel Cells **3**(1-2)**,** pp. 21–27.

[7] Lai, Y., Mittelsteadt, C. K., Gittleman, C. S., Dillard, D. A., 2005, "Viscoelastic Stress Model and Mechanical Characterization of Perfluorosulfonic Acid (PFSA) Polymer Electrolyte Membranes," *Proceedings of the Third International Conference on Fuel Cell Science, Engineering and Technology*, May 23–25, Ypsilanti, Michigan., pp. 161–167.

[8] Webber, A., Newman, J., 2004, "A Theoretical Study of Membrane Constraint in Polymer-Electrolyte Fuel Cell," AIChE J., **50**(12), pp. 3215–3226.

[9] Tang, Y., Santare, M.H., Karlsson, A.M., Cleghorn, S., Johnson, W.B., 2006, "Stresses in Proton Exchange Membranes due to Hydro-Thermal Loading," *J. Fuel Cell Sci. Technol.*, **3**, pp. 119–124.

[10] Kusoglu, A., Karlsson, A. M., Santare, M. H., Cleghorn, S., Johnson, W.B., 2006, "Mechanical Response of Fuel Cell Membranes Subjected to a Hygro-Thermal Cycle," Journal of Power Sources, **161**, pp. 987-996.

[11] Kusoglu, A., Karlsson, A. M., Santare, M. H., 2007, Cleghorn, S., Johnson, W.B., "Mechanical Behavior of Fuel Cell Membranes under Humidity Cycles and Effect of Swelling Anisotropy on the Fatigue Stresses," *Journal of Power Sources*, **170,** pp. 345-358.

[12] Kusoglu, A., Santare, M. H.,Karlsson, A. M., Cleghorn, S., Johnson, W.B., 2010, "Numerical Investigation of Mechanical Durability in Polymer Electrolyte Membrane Fuel Cells," *J. Electrochemical So.,* **157** (5), pp. B705-13.

[13] Zhang, Y., Mawardi, A., Pitchumani, R., 2006, "Effects of Operating Parameters on the Uniformity of Current Density Distribution in Proton Exchange Membrane Fuel Cells," *ASME Journal of Fuel Cell Science and Technology*, 3(4), pp. 464-476

[14] Wang, Y., Wang, C.Y., 2005, "Transient Analysis of Polymer Electrolyte Fuel Cells," *Electrochem. Acta*, **50**, pp. 1307-1315

[15] Bird, R.B., Stewart, W.E., Lightfoot, 1960, E.N., *Transport Phenomena*, Wiley, New York.

[16] Hill, R., 1950, "*The Mathematical Theory of Plasticity*," Clarendon Press, Oxford.

[17] Verma, A., Pitchumani, R., "Effects of Membrane Properties on Dynamic Behavior of Polymer Electrolyte Membrane Fuel Cell," ESFuelCell2013-18209, Proceedings of the7th International Conference on Energy Sustainability and 11th Fuel Cell Science Engineering and Technology Conference, July 23–26, 2013, Minneapolis, MN, USA.

[18] ANSYS® Academic Research, Release 14.0, Help System, Mechanical APDL Theory Reference, ANSYS, Inc.

Table 5.1: Source terms in the governing equations

Domain	S_v	S_i	S_s , S_m
Gas channels	0	0	0
Diffusion layers	$-\frac{\mu}{K_{GDL}}\vec{u}$	0	0
Catalyst layers	$-\frac{\mu}{K_{GDL}}\vec{u}$	anode: $-\frac{j_a}{2F}$ $(i = H_2)$ *[1]* $(i = O_2)$ $-\nabla.\left(\frac{n_d i_e}{F}\right)$ $(i = H_2O)$ cathode: *0* $(i = H_2)$ $-\frac{j_c}{4F}$ $(i = O_2)$ $\frac{j_c}{2F} - \nabla.\left(\frac{n_d i_e}{F}\right)$ $(i = H_2O)$	anode: $S_s = -j_a < 0$ $S_m = +j_a < 0$ cathode: $S_s = +j_c > 0$ $S_m = -j_c < 0$
Membrane	$-\frac{\mu}{K_{GDL}}\vec{u}$	0	0

Table 5.2. Geometrical and physical parameters used in the numerical simulations [13,14]

Parameter [units]	Symbol	Value
Gas channel depth [mm]		1.0
Diffusion layer thickness [mm]		0.3
Catalyst layer thickness [mm]		0.01
Membrane (N112) thickness [mm]		0.051
Fuel cell/Gas channel length [mm]		100.0
Temperature [K]	T	353
Permeability of diffusion layer [m^2]	K_{GDL}	10^{-12}
Permeability of catalyst layer [m^2]	K_{CL}	10^{-15}
Gas diffusion layer porosity	ε_{GDL}	0.6
Catalyst layer porosity	ε_{CL}	0.4
Volume fraction membrane in catalyst layer	ε_m	0.26
Anode reference exchange current density [A/m^3]	$j_{a,ref}$	5.00×10^8
Cathode reference exchange current density [A/m^3]	$j_{c,ref}$	500
H_2 diffusivity membrane [m^2/s]	$D_{H_2,mem}$	2.59×10^{-10}
H_2 diffusivity in gas [m^2/s]	$D_{H_2,ref}$	1.1×10^{-4}
O_2 diffusivity in membrane [m^2/s]	$D_{O_2,mem}$	8.328×10^{-10}
O_2 diffusivity in gas [m^2/s]	$D_{O_2,ref}$	3.2348×10^{-5}
H_2O diffusivity in gas [m^2/s]	$D_{H_2O,ref}$	7.35×10^{-5}

Table 5.3: Physical properties of materials used in the finite element analysis [10,11]

Material	ρ **[kg/m³]**	E **[MPa]**	υ
Bipolar plates	1800	10,000	0.25
GDE (Carbon Paper)	400	10,000	0.25
Membrane (Nafion® 112)	200	*Table 4*	0.25

Table 5.4: Physical properties of the membrane (Nafion® 112) used in the analysis [10,11]

RH [%]	**Young's Modulus [MPa]**	**Yield Stress [MPa]**	$\boldsymbol{\beta\left[\frac{m}{m\%RH}\right]\times 10^{-6}}$
30	121	4.20	1456
50	85	3.32	1197
70	59	2.97	2128
90	46	2.29	3670

Table 5.5: Initial conditions used in the FE analysis

Zero-stress Condition	RH *in membrane <= 30%*
Step 1: Mechanical Loading	Clamping Pressure is applied (p = 1 MPa)
Step 2: Pre-stressed + Hygral Loading	RH loading corresponding to E_{cell} = 0.8 V on membrane

Appendix A

The RH contour values in Fig. 5.2 can be represented terms of water content values and is given below. The relationship between RH and water content is clearly described in mathematical modeling and can the contour values can be converted to derive the water content values from RH values or vice-versa.

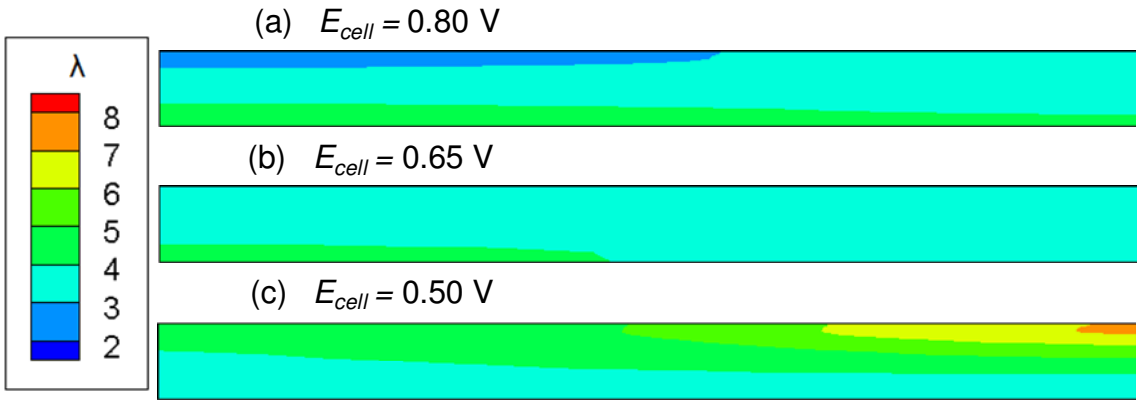

Figure A.1: Representation of Fig. 5.2 in terms of water content value, λ.

Chapter 6: Influence of Transient Operating Parameters on the Mechanical Behavior of Fuel Cells

Towards understanding the factors contributing to mechanical degradation, this chapter presents numerical simulations on the effects of operating conditions on the stresses and strain induced in the membrane constrained by bipolar plates on either sides and subjected to changing humidity levels. The fuel cell is subjected to dynamic changes in load to capture the water content values in the membrane using detailed three-dimensional (3D) computational fluid dynamics simulations. Using the information from the three-dimensional simulations, two-dimensional (2D) finite element (FE) analysis is used to predict the mechanical response of the membrane at various planar sections for hygral (water) loading and unloading cycles. The effects of operating parameters (anode and cathode pressure, stoichiometry and relative humidity at cathode inlet) on evolution of stresses and plastic deformations in the membrane are analyzed for cyclic changes in operating load.

6.1 Introduction

Polymer electrolyte membrane (PEM) fuel cells are attractive options as energy source for mobile and stationary applications. Faster transient response and low-temperature operation, makes PEM fuel cells a better power source alternative for automotive applications compared to other types of fuel cells. Improving the durability of membranes such as to meet the operational life of 5000h (150,000 miles equivalent) is one of the vital considerations for fuel cells to become a more viable option as power source in automotive applications [1-4]. Mechanical stresses arise as membrane swells (hydrates) or shrinks (dehydrates) as a function of moisture content during the transient process, requiring careful examination. These stresses may exceed the yield-limit causing the membrane to deform plastically, which, in turn, induces residual stresses, causes opening and propagation of cracks, and formation of pin-holes in the membrane or delamination between the membrane and the GDL, causing degradation [5-13]. The operating conditions play an important role in determining the membrane water content for given external load changes thus affecting the performance and durability of fuel cells.

Numerical studies have been carried out by several researchers focusing on the degradation mechanisms and mechanical behavior. One of the first numerical studies incorporating the effects of mechanical stresses on fuel cell was performed by Weber and Newman [10]. The model presented a one-dimensional analysis of a fuel cell and did not incorporate the property changes across layers of the fuel cell. Tang et al. [11] investigated the effects of stresses induced by swelling and thermal expansion on a uniformly hydrated membrane for different clamping methods, and suggested that the contribution by in-plane stresses are more significant than others. Kusoglu et al. [12,13] incorporated plastic deformation and anisotropy to demonstrate the residual stresses induced as the membrane is cycled through various uniformly distributed humidity loads. The above approaches [11-13] have been limited to either using uniform membrane hydration or simplistic water content profiles that do not take in to account the complex water distribution across length and thickness for realistic load changes. Kusoglu et al. [14] later incorporated the effects of non-uniform distribution of water in membrane, by specifying the water volume fraction at the membrane boundaries and solving for diffusion of water across the membrane. Kleeman et al. [15] characterized the local compression distributions in GDL and the associated effect on electrical material resistance. Zhou et al. [16] analyzed the effects of assembly pressure and operating temperature and humidity on PEM fuel cell stack deformation, contact resistance, overall performance and current distribution. Serincan and Pasaogullari [17] studied the effects of humidity, and operating voltage on the mechanical stresses induced due to thermal and hygral loading, suggesting that thermal stresses are typically a fraction of the hygral stresses in a typical PEMFC operation. Taymaz and Benli [18] studied the effect of assembly pressure on the performance of PEM fuel cells. Wang et al. [19] conducted endurance experiments to emphasize the impact of in-cell water management techniques on the degradation. In our previous study [20], we have presented a model to predict the mechanical stresses induced in membrane due change in loads for specified inlet humidification value of cathode feed for two different sections along the length of fuel cell.

In the present study, CFD simulations are carried out to model the complex water transport dynamics for various load changes under different operating conditions and obtain membrane water content distribution across the fuel cell dimensions. The water content distribution, in turn, is used in a finite element analysis of a planar geometry of the membrane to calculate the evolution of stress and deformation in the membrane for hygral loading and unloading cycles.

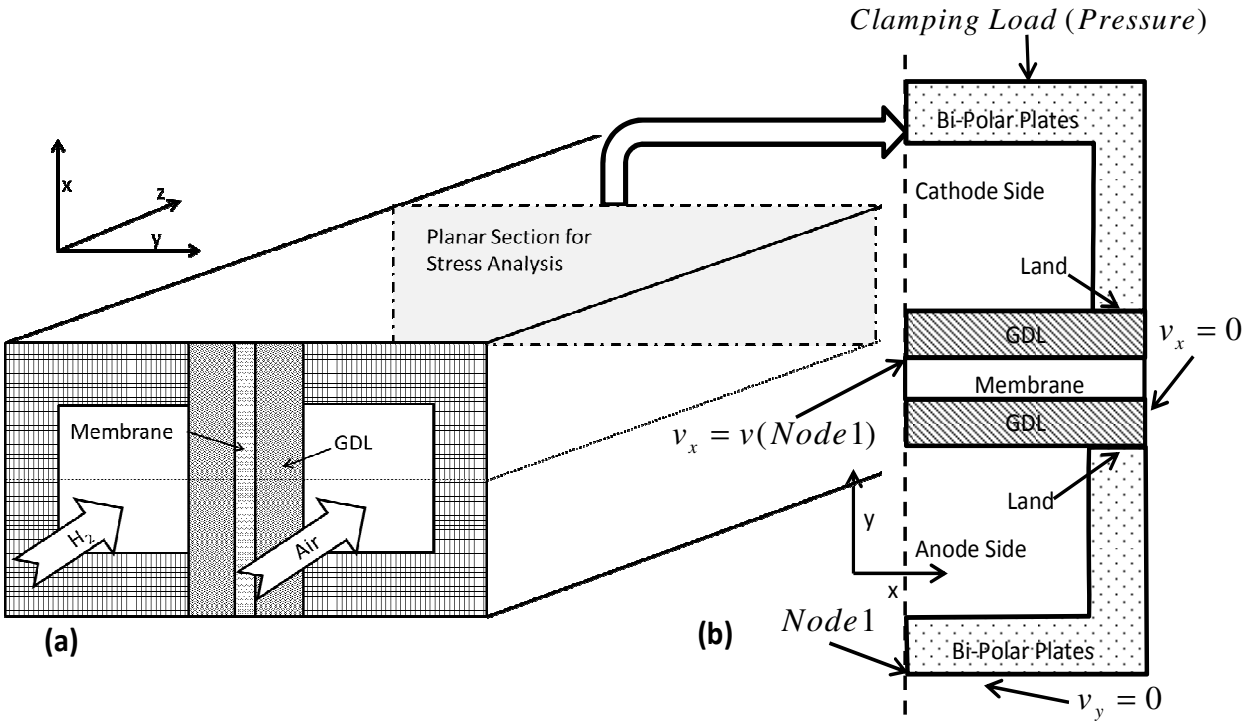

Figure 6.1: Schematic of a PEM fuel cell showing (a) a three-dimensional view of a single channel and (b) a planar half-section along the z-axis.

The operating conditions studied are anode and cathode pressure, anode and cathode stoichiometry, and relative humidity at cathode inlet. The mathematical modeling is presented in the next section, followed by the presentation and discussion of results in a later section.

6.2 Mathematical Model

Please refer to section 5.2 for a detailed discussion on the Water Transport Modeling (Section 5.2.1) and Membrane Hygroscopic Stress Analysis (Section 5.2.2).

The three-dimensional CFD simulations give the water concentration at the membrane, which in turn provides the *RH* to be used as input for the FE analysis. It should be noted here that the sections along the z-axis are taken at various lengths and are used for FE analysis, which is two-dimensional. For simplicity the *RH* is changed linearly from one steady state value to another steady state value locally. The above model and boundary conditions are implemented in commercial FE analysis software ANSYS®14.0 [26] and solved using coupled-field ANSYS® Mechanical APDL solver, for specified load changes at various operating conditions. About 5000 elements are used to capture the detailed stress and strain profiles over

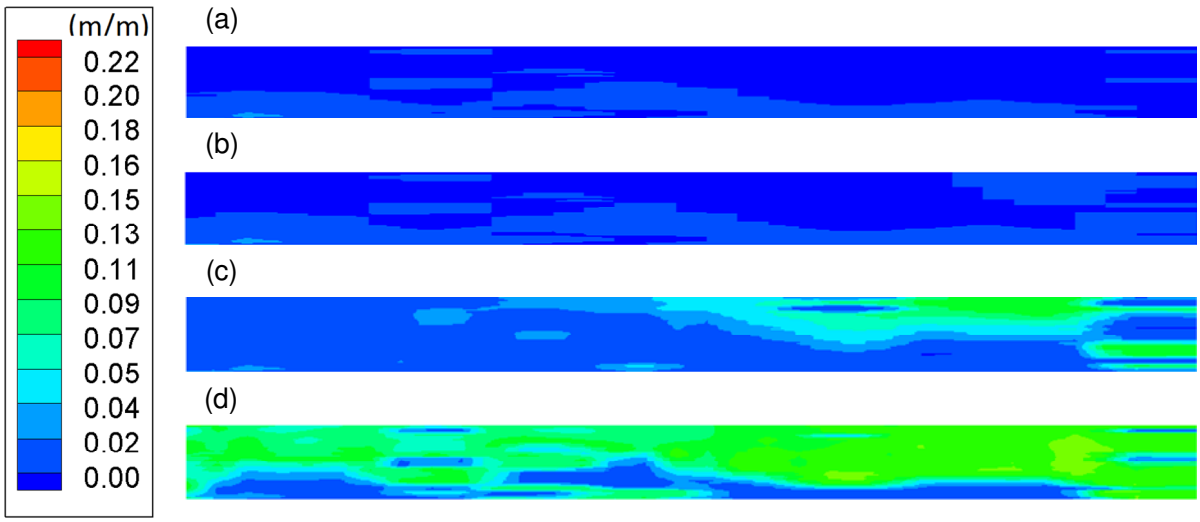

Figure 6.2: Contours of equivalent plastic strain, ε_{eq}^{pl}, for $RH_c = 25\%$, at z = 0.01 m, for for (a) ΔE_{cell} = 0.00 V, (b) ΔE_{cell} = 0.10 V, (c) ΔE_{cell} = 0.20 V and (d) ΔE_{cell} = 0.30 V.

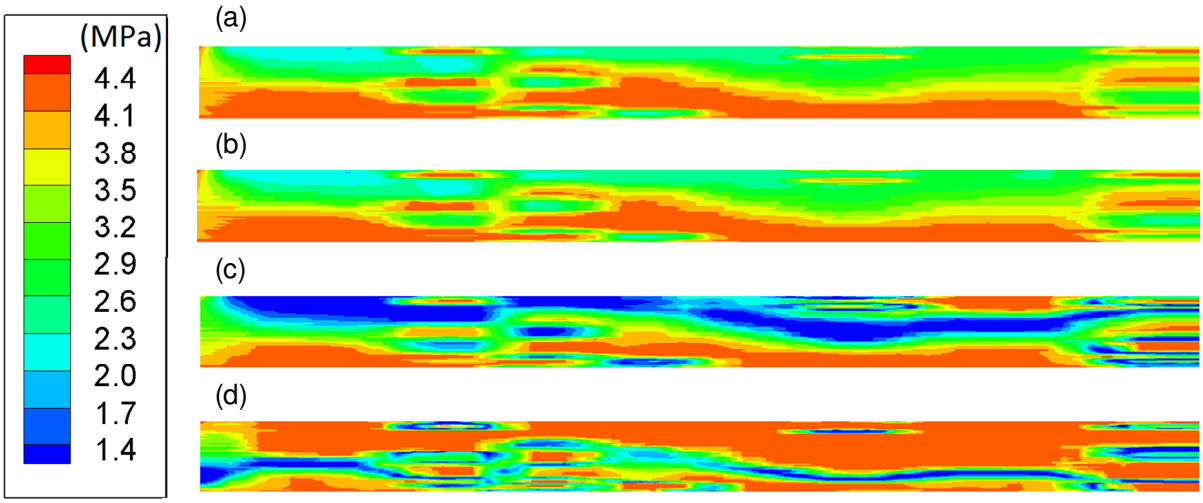

Figure 6.3: Contours of von-Mises Stress (equivalent stress), σ_{eq}, for RH_c = 25%, at z = 0.01 m, for (a) ΔE_{cell} = 0.00 V, (b) ΔE_{cell} = 0.10 V, (c) ΔE_{cell} = 0.20 V and (d) ΔE_{cell} = 0.30 V.

different regions. The simulation time is dependent on the levels of plastic deformation induced as well as on the number of iterations required to get a converged solution, based on a convergence criteria of 10^{-6} on the residuals for all the equations. The maximum time taken by a simulation is less than 30 minutes for each cycle on an Intel® Xeon™ Processor 3.33 GHz. The computational techniques used in the present work were reported in our previous studies

[20,22,24,25]. In particular, model validation and information on grid independence study can be found in Ref. [20,22] and are omitted here for brevity.

6.3 Results and Discussion

This section presents the results and discussion for the stresses and plastic deformation induced in the membrane due to changes in RH profiles, resulting from changes in load. The unit cell is cycled from E_{cell} = 0.80 V to E_{cell} = 0.50, 0.60, 0.65 and 0.70 V, and back to E_{cell} = 0.80 V, cycling the membrane moisture content to the corresponding *RH*s, thus inducing, stresses as the membrane swells and de-swells, and plastic deformation in case stresses exceed yield strength. The results are presented for planar sections taken at z = 0.01 m, 0.03 m, 0.05 m, 0.07 m and 0.09 m, with z = 0.0 m being the inlet and z = 0.1 m being the outlet. The variation of maximum plastic strain induced and percentage volume of membrane plastically deformed as a function of load change and operating parameters for various sections along the length of the fuel cell is presented and discussed in detail. Quantities representative of mechanical behavior such as maximum stress, strain in membrane and percentage volume of membrane deformed plastically are used to analyze the mechanical behavior at a section.

Figure 2 depicts the contour plots for equivalent plastic strain, ε_{eq}^{pl}, at z = 0.01 m (near the inlet) and for $RH_c = 25\%$, for ΔE_{cell} = 0.0 V (Fig. 2(a)), ΔE_{cell} = 0.10 V (Fig. 2(b)), ΔE_{cell} = 0.20 V (Fig. 2(c)) and ΔE_{cell} = 0.30 V (Fig. 2(d)) representing the cyclic load change from 0.80 V to 0.80, 0.70, 0.60 and 0.50 V and back to 0.80 V, respectively. Following the configuration in Fig. 1(b), the top of the membrane denotes the cathode and the bottom of the membrane denotes the anode, in the contour plots presented in Fig. 2. Figure 2(a) shows the ε_{eq}^{pl} contours for E_{cell} = 0.80 V or ΔE_{cell} = 0.0 V, at the beginning of the cycle. As the membrane swells owing to increase in water content, compressive stresses are induced and if the stresses exceed the yield strength, it leads to a plastic deformation in the membrane. The stresses corresponding to the strain in Fig. 2 are depicted in Fig. 3, with Fig. 3(a) showing the von-Mises stress, or as referred to in this work as equivalent stress, σ_{eq}, for the corresponding strain in Fig. 2(a). Fig. 2(a) shows that the membrane undergoes plastic deformation for base load (E_{cell} = 0.80 V or ΔE_{cell} = 0.00 V), owing to the higher water content on anode side at the near inlet region. It can be seen that additional strain is observed at the cathode land region for ΔE_{cell} = 0.10 V (Fig 2(b)), in comparison to that observed for ΔE_{cell} = 0.00 V in Fig. 2(a). This behavior can be attributed to increase in membrane

water content at cathode region owing to higher current density for ΔE_{cell} = 0.10 V. It is noted from Fig. 2(c) that there is a considerable increase in magnitude of plastic strain at the cathode side owing to higher current density for E_{cell} = 0.60 V in comparison to that observed in Figs. 2(a) and 2(b). It can be seen Fig. 2(d) that almost all of the membrane undergoes plastic deformation for ΔE_{cell} = 0.30 V.

Figure 3 shows the contours for equivalent stress, σ_{eq}, corresponding to the equivalent strain observed in Fig. 2. It can been seen from Fig. 3(a) that regions of high stress occur at the anode region due to the higher water content in the anode region at the inlet for lower loads. It is noted that there is no significant difference in the stress distribution for ΔE_{cell} = 0.00 V (Fig. 3(a)) and ΔE_{cell} = 0.10 V (Fig. 3(b)) owing to the relatively small difference in current density. In comparison to the observed contours in Figs. 3(a) and 3(b) the stress contours for ΔE_{cell} = 0.20 V (Fig. 3(c)) show considerable difference in the distribution. This behavior can be attributed to the redistribution of stresses as the membrane undergoes further plastic deformation upon unloading. In comparison to the observed distribution in Figs. 3(a), (b) and (c), Fig 3(d) shows higher stress values upon unloading at the cathode regions. The comparison of Figs. 3(b), (c) and (d) from Fig. 3(a) shows the residual stresses and their localization at the membrane undergoes cyclic load changes. It is noted here that the equivalent stress at the plastically deformed regions are not fixed to a single value, but since the yield strength is a function of RH, we see a distribution of yield stress values, implying that the membrane undergoes plastic deformation over a range of RH values. Also, with plastic deformation, the stresses are redistributed locally, further changing the profile of equivalent stress across the membrane. Consequently, the best way to represent the plastically deformed region is through ε_{eq}^{pl}, indicating plastic deformation for non-zero values. Note that the contours presented and discussed in Figs. 2 and 3 are illustrative of representative combinations of load change and operating parameters. In the interest of conciseness, contours of RH, stress and strain for the various combinations of load change and operating parameters studied are not presented in the discussion below. Instead, the discussion in the remainder of this section is on the maximum values of the parameters, and deriving design windows based on the maximum values.

Figure 4(a) shows the variation of maximum equivalent plastic strain along length of the membrane for RH_c = 25% with the variations for percentage volume of membrane plastically

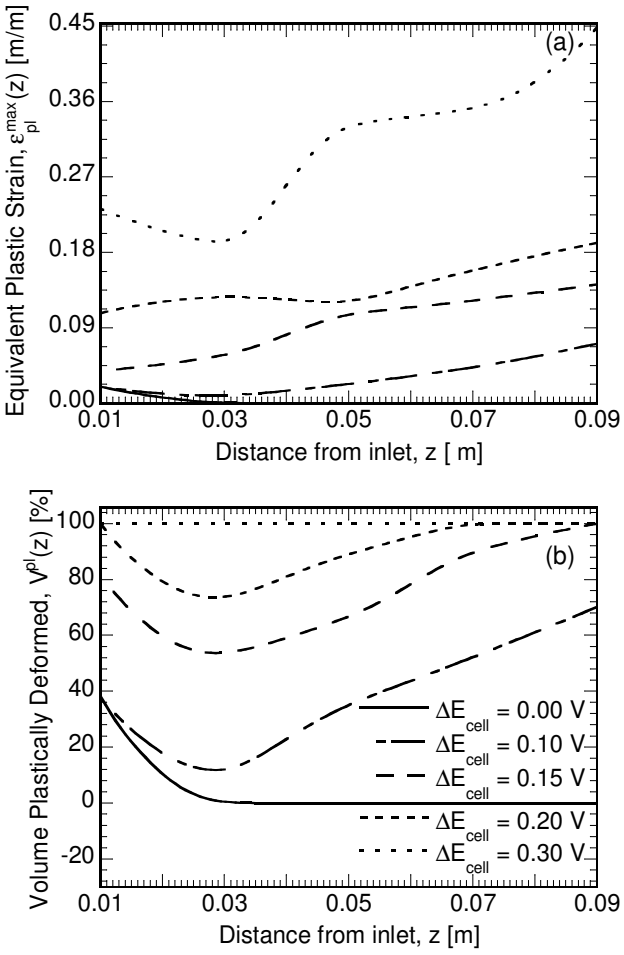

Figure 6.4: Variation in (a) $\varepsilon_{pl}^{max}(z)$ and (b) $V^{pl}(z)$ as a function of z, for RH_c = 25%.

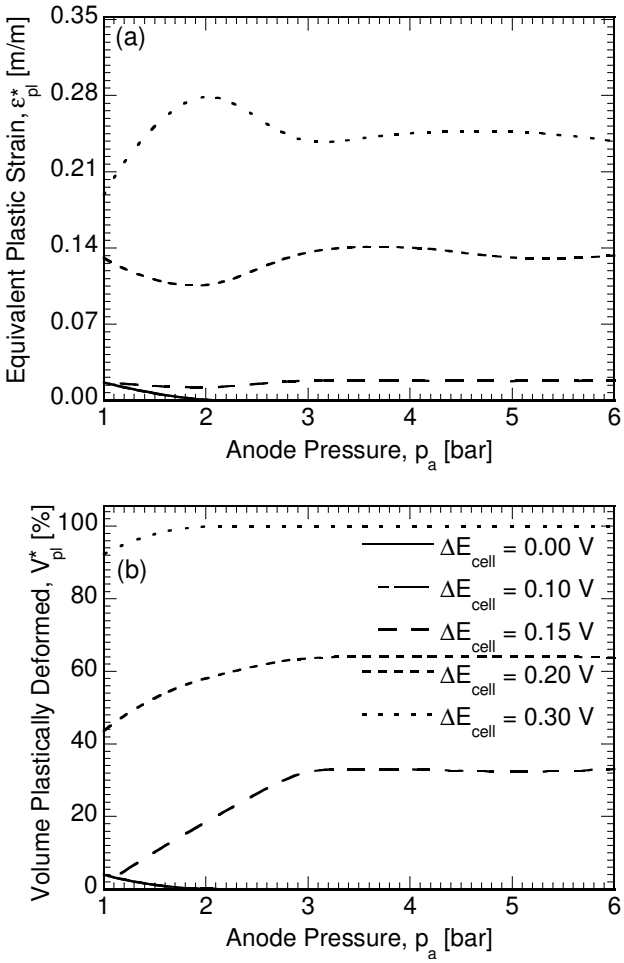

Figure 6.5: Variation in (a) ε_{pl}^{*} and (b) V_{pl}^{*} as a function of anode pressure (p_a).

deformed depicted in Fig. 4(b). The other operating conditions are fixed at base value p_a = 2.0 bar, ζ_a = 2.0, ζ_c = 2.0, p_c = 2.0 bar and RH_a =100%. The maximum ε_{eq}^{pl} at a planar section is represented by $\varepsilon_{pl}^{max}(z)$, and the percentage volume of the membrane undergoing plastic deformation at that location by $V^{pl}(z)$. It can be seen from Fig. 4(a) that for ΔE_{cell} = 0.00 V there exists no plastic strain for $z \geq 0.03$ m. This can be attributed to the fact that the high humidity at inlet leads to plastic deformation at inlet but as the water is further redistributed along the length due to electro-osmotic drag, the water content values drop implying reduced swelling and plastic strain values. A more detailed discussion on the variation of water content along the length of the membrane for various operating parameters can be found in Refs. [22,24,25].

Similarly from Fig. 4(b) it can be seen that the $V^{pl}(z)$ drops from 40% (approx) to 0% for $z \geq$ 0.03 m. It can be seen from Fig. 4(a) that the plastic strain is maximized at the outlet for $\Delta E_{cell} >$ 0.00 V. This behavior can be attributed to the increase in the water content at the outlet for cycling through higher loads. It is noted that $\varepsilon_{pl}^{max}(z)$ increases monotonically for ΔE_{cell} = 0.15 V whereas for ΔE_{cell} = 0.10, 0.20 and 0.30 V a non-monotonic behavior is observed. The decrease in the $\varepsilon_{pl}^{max}(z)$ for ΔE_{cell} = 0.30 V from z = 0.01 m to 0.03 m can be attributed to the decrease in water content values owing to the electro-osmotic drag. As the water generated at the cathode catalyst layer is redistributed, an increase in $\varepsilon_{pl}^{max}(z)$ is observed for $z >$ 0.03 m. It can be seen from Fig. 4(b) that the $V^{pl}(z)$ decreases from z = 0.01 m to z = 0.03 m for ΔE_{cell} < 0.30 V owing to the effect of electro-osmotic drag on water content values, as discussed earlier. It is also noted from Fig. 4(b) that all of the membrane undergoes plastic deformation for ΔE_{cell} = 0.30 V, whereas for ΔE_{cell} = 0.20 V the membrane undergoes complete deformation for $z >$ 0.07 m and z = 0.01 m. It is also noted that although the $V^{pl}(z)$ decreases from z = 0.01 m to z = 0.03 m for ΔE_{cell} = 0.15 and 0.20 V the $\varepsilon_{pl}^{max}(z)$ shows an increase. This behavior can be attributed to the localized increase in the membrane water content at the cathode region leading to such an increase. Similar to the observation in Fig. 4(a), it can be seen from Fig. 4(b) that the $V^{pl}(z)$ is maximized at the outlet region.

The results in the remainder of this section focus on the effect of operating parameters discussed earlier on the plastic deformation induced due to load cycling. The maximum of $\varepsilon_{pl}^{max}(z)$, for all z, and $V^{pl}(z)$ over the length of the fuel cell are chosen to be the representative parameter for discussion and are represented by ε_{pl}^{*} and V_{pl}^{*}, respectively. The effects of pressure and stoichiometry on anode and cathode sides along with relative humidity on cathode side are discussed in detail.

Figure 5 shows the variation in ε_{pl}^{*} (Fig. 5(a)) and V_{pl}^{*} (Fig. 5(b)) as a function of anode pressure, p_a. It can be seen from Fig. 5(a) that ε_{pl}^{*} shows a non-monotonic variation for ΔE_{cell} = 0.15, 0.20 and 0.30 V. The ε_{pl}^{*} for ΔE_{cell} = 0.30 V increases for increase in anode pressure p_a from 1 to 2 followed owing to the significant increase in the hydrogen concentration with increase in anode pressure. It is noted that there exists no significant variation for further in ε_{pl}^{*} for $p_a >$ 3. This behavior can be attributed to the fact that the reaction rate is limited by the oxygen

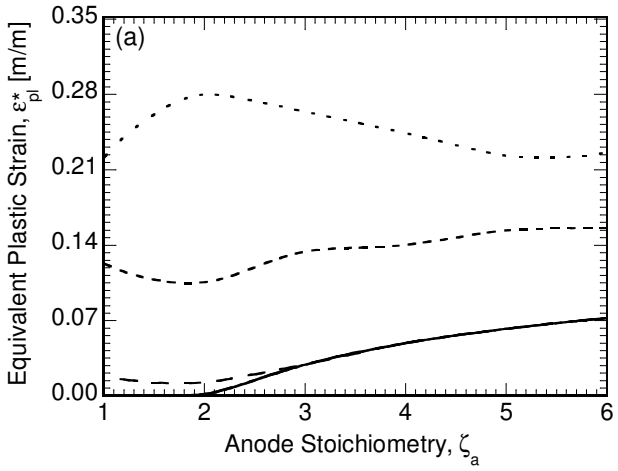

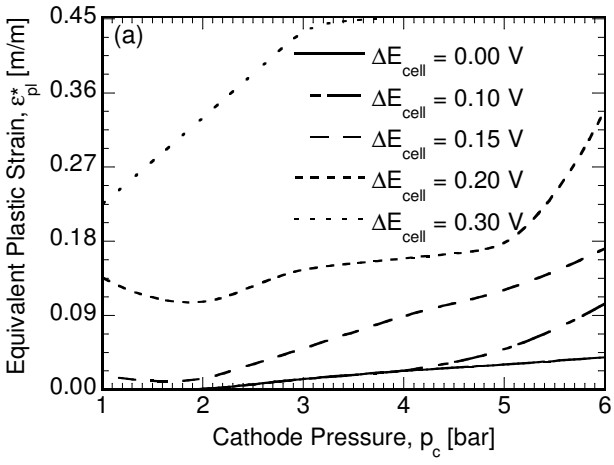

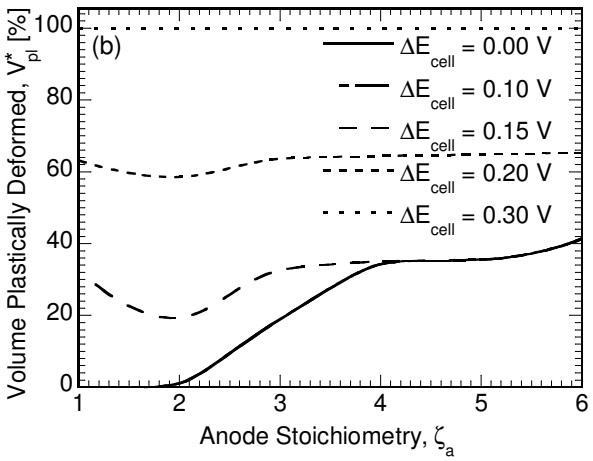

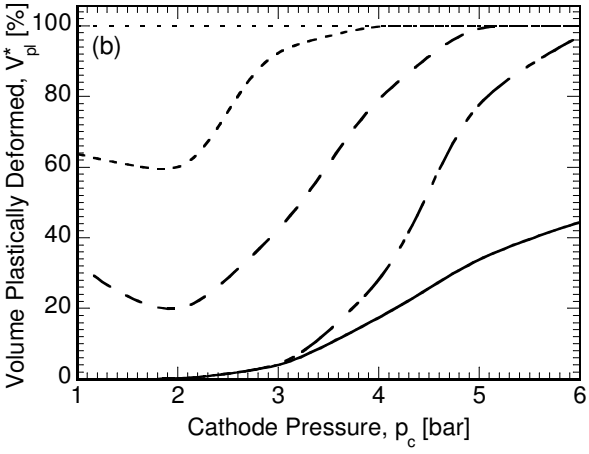

Figure 6.6: Variation in (a) ε_{pl}^{*} and (b) V_{pl}^{*} as a function of anode stoichiometry (ζ_a).

Figure 6.7: Variation in (a) ε_{pl}^{*} and (b) V_{pl}^{*} as a function of cathode pressure (p_c).

concentration on cathode side and thus increase in anode pressure does not lead to any significant changes in membrane water content. The higher value for ε_{pl}^{*} for p_a = 2 is due to the fact that the membrane undergoes further plastic deformation upon unloading, resulting in higher localized strain values. It is noted from Fig. 5(b) that the V_{pl}^{*} increases from increase in pressure from 1 to 2 bar with complete plastic deformation for p_a > 2. In contrast to that observed for ΔE_{cell} = 0.30 V, for ΔE_{cell} = 0.20 V the ε_{pl}^{*} decreases for increase in anode pressure from 1 to 2 bar. It is also noted that the variation in ε_{pl}^{*} for p_a > 2 is relatively small compared to that observed for increase in pressure from 1.0 to 2.0 bar. It can be seen from Fig. 5(a) and 5(b) that for ΔE_{cell} = 0.0 and 0.10 V there exists no plastic strain for p_a > 2.0. It is also noted that increase in anode pressure does not lead to significant increase in ε_{pl}^{*} for ΔE_{cell} = 0.15 V whereas

the V_{pl}^{*} shows an considerable increase for increase in p_a from 1.0 to 2.0, with no observable change for further increase in anode pressure.

Figure 6 depicts the variation in ε_{pl}^{*} (Fig. 6(a)) and V_{pl}^{*} (Fig. 6(b)) as a function of anode stoichiometry, ζ_a. It can be seen from Fig. 6(a) that ε_{pl}^{*} shows a non-monotonic variation for ΔE_{cell} = 0.15, 0.20 and 0.30 V. The ε_{pl}^{*} for ΔE_{cell} = 0.30 V increases for increase in ζ_a from 1.0 to 2.0 owing to the significant increase in the supply rate of anode feed with increase in anode stoichiometry. As the anode stoichiometry is further increased the rate at which the water is taken out by the anode feed also increases resulting in decrease in ε_{pl}^{*} values for ζ_a > 2.0, for ΔE_{cell} = 0.30 V, as seen in Fig. 6(a). It can be seen from Fig. 6(b) that the V_{pl}^{*} for ΔE_{cell} = 0.30 V is 100% for the range of ζ_a studied. In contrast to that observed for ΔE_{cell} = 0.30 V, for ΔE_{cell} = 0.20 V, ε_{pl}^{*} slows a slight decrease for increase in ζ_a from 1.0 to 2.0 followed by increase in maximum values for further increase in ζ_a. The above behavior can be attributed to a much smaller increase in current density and thus the water content for ΔE_{cell} = 0.20 V in comparison to that observed for ΔE_{cell} = 0.30 V, for increase in ζ_a from 1.0 to 2.0. It is also noted from Fig. 6(b) that the variation in V_{pl}^{*} for ΔE_{cell} = 0.20 V is not as pronounced as observed for ΔE_{cell} < 0.20 V. It can be seen that for ΔE_{cell} = 0.0 and 0.10 V there exists no plastic strain for ζ_a < 1.6, followed by an increase in ε_{pl}^{*} for further increase in ζ_a. It is also noted that the variation of ε_{pl}^{*} and V_{pl}^{*} are coincident implying that the water content is not significantly affected by the increase in load to ΔE_{cell} = 0.10 V. The similar is observed for ΔE_{cell} = 0.15 V for ε_{pl}^{*} and V_{pl}^{*} given ζ_a > 3.0 and ζ_a > 4.0, respectively.

Figure 7 shows the variation in ε_{pl}^{*} (Fig. 7(a)) and V_{pl}^{*} (Fig. 7(b)) as a function of cathode pressure, p_c. It can be seen from Fig. 7(a) that ε_{pl}^{*} shows a monotonic increase for an increase in p_c for ΔE_{cell} = 0.30 V. The increase in cathode pressure leads to increase in the oxygen concentration at cathode side implying higher current density and thus higher water content and strain values. In contrast to that observed for ΔE_{cell} = 0.30 V for ΔE_{cell} < 0.20 V there exists no plastic deformation for p_c < 2.0. It can be seen from Fig. 7(b) that the V_{pl}^{*} = 100% for the range of cathode pressure studied. It is also noted that there is a significant difference in the ε_{pl}^{*} values observed for ΔE_{cell} = 0.30 V and that observed for ΔE_{cell} < 0.30 V, owing to relatively higher current density for E_{cell} = 0.50 V compared to higher voltages. The variation in ε_{pl}^{*} for ΔE_{cell} =

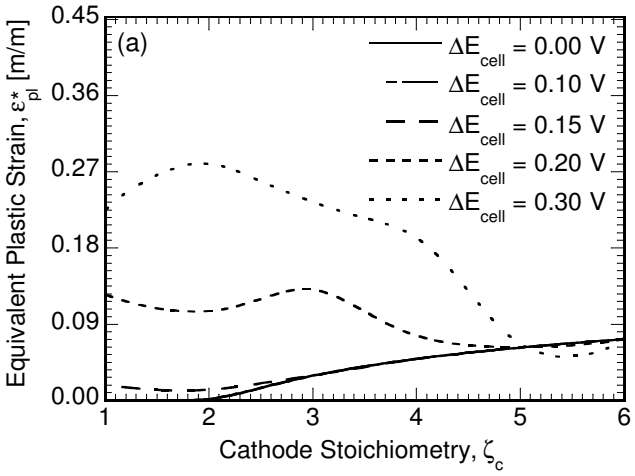

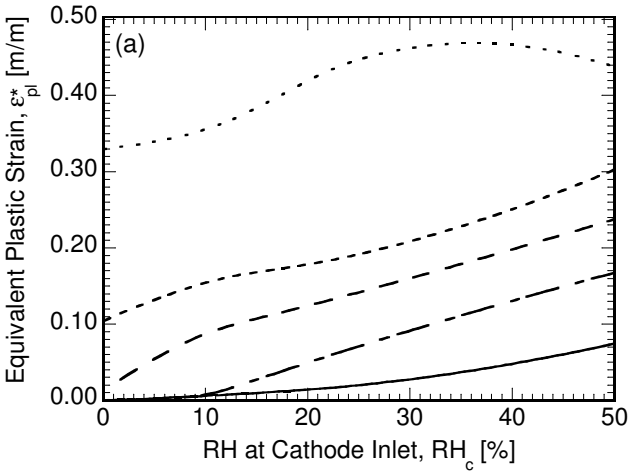

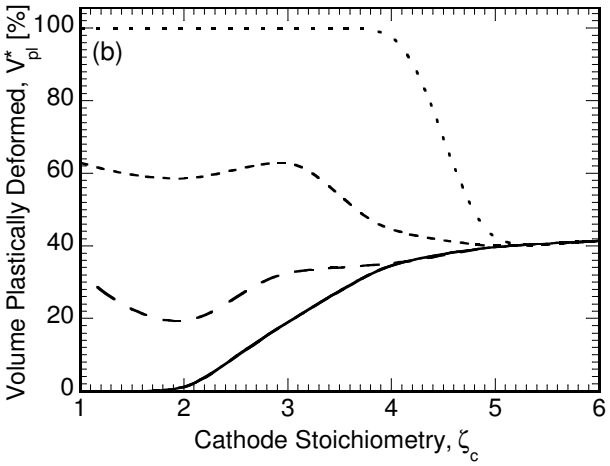

Figure 6.9: Variation in (a) ε_{pl}^{*} and (b) V_{pl}^{*} as a function of relative humidity at cathode stoichiometry (ζ_c).

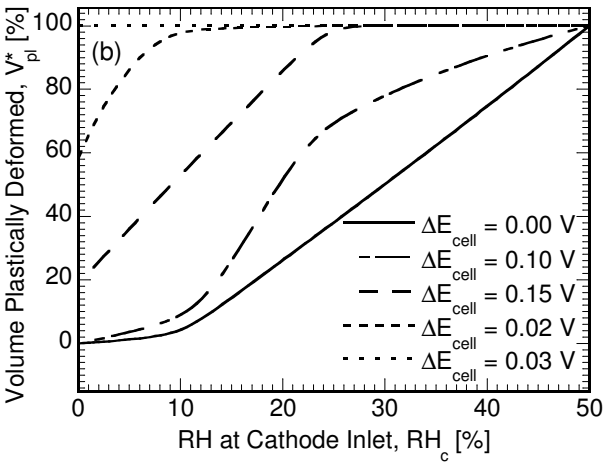

Figure 6.9: Variation in (a) ε_{pl}^{*} and (b) V_{pl}^{*} as a function of relative humidity at cathode inlet (RH_c).

0.0 and 0.10 V are coincident for p_c < 4.0, as seen from Fig. 7(a) implying relatively smaller difference in the current density values for lower values of cathode pressure. It can be seen that V_{pl}^{*} = 100% for ΔE_{cell} = 0.20 V for p_c > 5.0. In comparison to that observed in Fig. 5(b) and 6(b), the V_{pl}^{*} for ΔE_{cell} = 0.10 V reaches a high of 96% (approx) as seen in Fig. 7(b) implying stronger correlation of water content to cathode pressure for higher voltages. Comparing the maximum ε_{pl}^{*} in Figs. 5(a), 6(a) and 7(a) it can be seen that the cathode pressure significantly affects the plastic strain values.

Figure 8 depicts the variation in ε_{pl}^{*} (Fig. 8(a)) and V_{pl}^{*} (Fig. 8(b)) as a function of cathode stoichiometry, ζ_c. It can be seen from Fig. 8(a) that ε_{pl}^{*} shows a non-monotonic variation for ΔE_{cell} = 0.15, 0.20 and 0.30 V. The ε_{pl}^{*} for ΔE_{cell} = 0.30 V increases for increase in ζ_c from 1.0 to 2.0 owing to the significant increase in the supply rate of cathode feed with increase in cathode stoichiometry. As the cathode stoichiometry is further increased the rate at which the water is taken out by the cathode feed also increases resulting in decrease in ε_{pl}^{*} values for ζ_c > 2.0, for ΔE_{cell} = 0.30 V, as seen in Fig. 8(a). The similar is observed for ΔE_{cell} = 0.20 V as the stoichiometry is increased from 3.0. It is noted that there exists no plastic strain for ΔE_{cell} = 0.0 and 0.10 V for ζ_c < 2.0, with increase in ε_{pl}^{*} for increase in ζ_c beyond 2.0. It is also noted that the plastic strain for ζ_c > 2.0 is governed by the plastic strain at base load ΔE_{cell} = 0.00 V as seen by the coincident variations. As discussed earlier this behavior can be attributed to the dominating effect of water removal rate from cathode on the water content values. In contrast to the behavior observed for higher loads, for lower loads the maximum plastic deformation happens at the near inlet region and the effect of water generation dominates that of water removal leading to the observed behavior in Fig. 8(a). It can be seen from Fig. 8(b) that the V_{pl}^{*} for ΔE_{cell} = 0.30 V is 100% for ζ_c < 4.0, with decrease in V_{pl}^{*} for increase in ζ_c from 4.0 to 5.0 and finally coinciding with the $V_{pl}^{*}$for ΔE_{cell} = 0.00 V. The similar behavior is observed for the variation in V_{pl}^{*} for ΔE_{cell} = 0.20 V. The V_{pl}^{*} for ΔE_{cell} = 0.0 and 0.10 V shows significant increase for increase in ζ_c beyond 2.0.

Figure 9 depicts the variation in ε_{pl}^{*} (Fig. 8(a)) and V_{pl}^{*} (Fig. 8(b)) as a function of inlet humidity at cathode inlet, RH_c. It can be seen from Fig. 8(a) that ε_{pl}^{*} shows a monotonic increase for increase in RH_c for ΔE_{cell} < 0.30 V, whereas the similar is observed for RH_c < 35% for ΔE_{cell} = 0.30 V. This behavior can be attributed to increase in water content in the membrane as the relative humidity at the cathode inlet is increased. It can be seen that the ε_{pl}^{*} at a given RH_c increase with increase in ΔE_{cell}, with maximum for ΔE_{cell} = 0.30 V. It is also noted there is a significant difference in the maximum plastic strain values for ΔE_cell = 0.30 V and ΔE_{cell} < 0.30 V, owing to the relative difference in current density. It can be seen from Fig. 9(b) that the V_{pl}^{max} for ΔE_{cell} = 0.30 V is 100% for the range of RH_c studied, whereas for ΔE_{cell} = 0.15 and 0.20 V, V_{pl}^{*} = 100% for RH_c > 10% and RH_c > 25%, respectively. In contrast to the observation in Figs. 5(b),

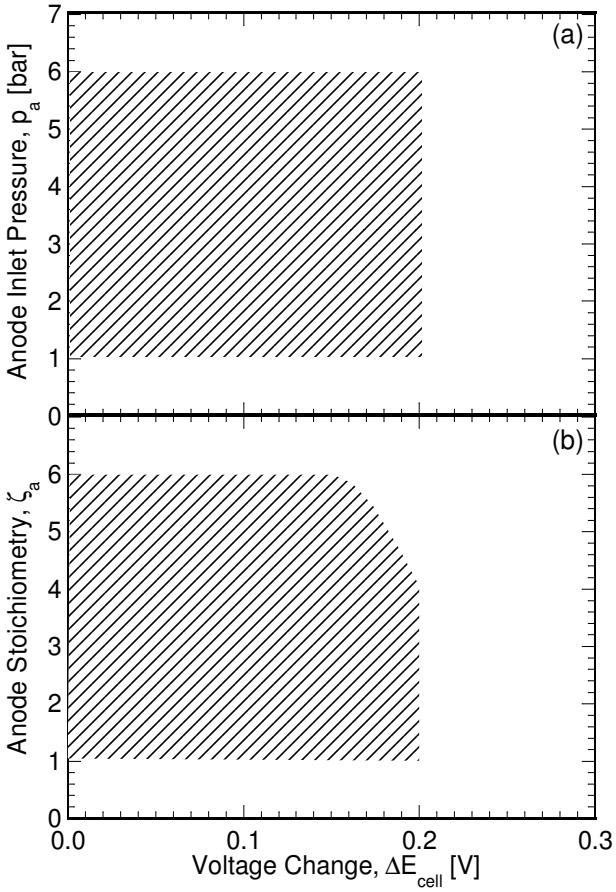

Figure 6.10: Design window based on limiting the ε_{pl}^{*} < 0.14 m/m, for (a) anode pressure, p_a and (b) anode stoichiometric flow ratio, ζ_a, as a function of cell voltage change, ΔE_{cell}.

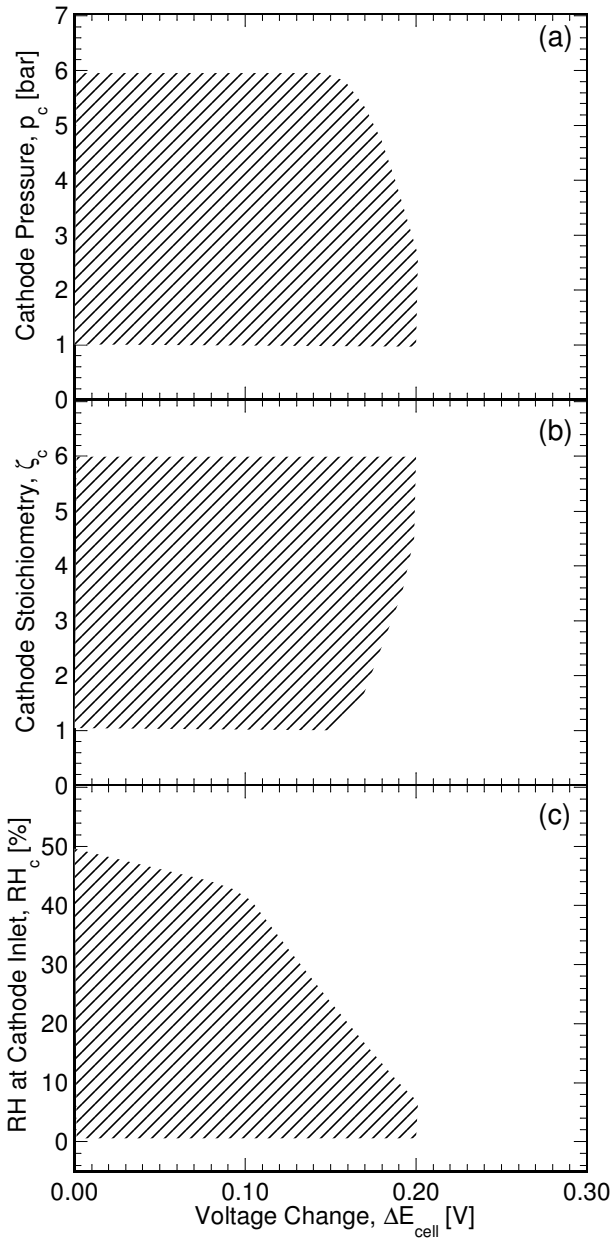

Figure 6.11: Design window based on limiting the ε_{pl}^{*} < 0.14 m/m, for (a) cathode pressure, p_c, (b) cathode stoichiometric flow ratio, ζ_c, and (c) cathode relative humidity RH_c, as a function of cell voltage change, ΔE_{cell}.

6(b), 7(b), 8(b) it can be seen from Fig. 9(b) that V_{pl}^{*} reaches 100% for ΔE_{cell} = 0.0 and 0.10 V at RH_c = 10%.

It is seen from Fig. 5–9 that operating conditions and magnitude of load change significantly affect the plastic deformation of membrane in a constrained environment. Cathode pressure and inlet relative humidity at cathode side, are the dominant parameters that affect the amount of plastic deformation incurred by the membrane. It is also seen that the operating parameters affect the sections along the length of fuel cell differently. The increase in cathode stoichiometry leads to increase in the plastic strain at the near inlet region, whereas, there is significant decrease in the plastic deformation at the near outlet region. Increase in cathode stoichiometry leads to faster removal of water generated at cathode layers, thus minimizing the water content values, leading to decrease in the plastic strain. On the other hand, anode stoichiometry does not affect the plastic strain significantly compared to other parameters. Figures 5–9 can be used to identify the values of the operating conditions for which ε_{pl}^{*} is minimized. It can be seen that for ΔE_{cell} = 0.30 V and 0.20 V ε_{pl}^{*} is minimum for ζ_c = 5.0, while other operating conditions are fixed at base value (p_a = 2.0 bar, ζ_a = 2.0, p_c = 2.0 bar and RH_c = 0%). Whereas, for ΔE_{cell} = 0.15 V, ε_{pl}^{*} is minimized for base value of parameters, p_a = 2.0 bar, ζ_a = 2.0, p_c = 2.0 bar, ζ_c = 2.0 and RH_c = 0%. In contrast to the observation for ΔE_{cell} = 0.30 and 0.20, 0.15 V, for ΔE_{cell} = 0.10 and 0.00 V, ε_{pl}^{*} is minimized over range of operating parameters; ε_{pl}^{*} is zero for $p_a \geq$ 2.0 bar, $\zeta_a \leq$ 2.0, $p_c \leq$ 2.0 bar, $\zeta_c \leq$ 2.0 and RH_c = 0%, independently, while other operating parameters are fixed at base values.

The variations in Figs. 5–9 may be used to identify upper and lower bounds on the operating parameters at the anode and the cathode for which the ε_{pl}^{*} is maintained within a specified value, for given load changes. For this study, the desired value is chosen to be 0.14 m/m. Based on the identified upper and lower bounds, design windows can be constructed for the operating conditions, as presented in Figs. 10 and 11 for the anode and cathode parameters, respectively. Figures 10(a) and (b) present the operating windows for the anode pressure and anode stoichiometric flow ratio, respectively, as a function of the change in the voltage, ΔE_{cell}. It can be seen from Figs 10(a) and (b) that there exists no operable region for ΔE_{cell} > 0.20 V. The upper limit and lower limits for $\Delta E_{cell} \leq$ 0.20 V is marked by the limiting value of anode pressure used in the study. It can be seen that for $\Delta E_{cell} \leq$ 0.20 V the ε_{pl}^{*} is below 0.14 m/m for the range of anode pressure studied. In contrast to the observation in Fig. 10(a), in Fig. 10(b) it can be seen that for ΔE_{cell} > 0.15 V the upper limit for anode stoichiometry decreases with the increase in load change, with no operable range for ΔE_{cell} > 0.20 V. Similar to the observation in

Fig. 10(a), the upper and lower limits are decided by the range of study which are 6.0 and 1.0, respectively for $\Delta E_{cell} \leq 0.15$ V.

Design windows similar to those in Fig. 10 are constructed for the cathode operating parameters, as presented in Fig. 11. Figures 11(a), (b) and (c) show the operating windows for cathode pressure, stoichiometric flow ratio and relative humidity, respectively, such that $\varepsilon_{pl}^{*} <$ 0.14 m/m. Similar to the observation in Fig. 10 that there exists no operable region for $\Delta E_{cell} >$ 0.20 V in Fig. 11. The upper limit and lower limits for $\Delta E_{cell} \leq 0.15$ V is marked by the limiting value of range of cathode pressure used in the study. It can be seen from Fig. 11(a) that for $\Delta E_{cell} > 0.15$ V the upper limit for cathode pressure decreases with the increase in load change, with no operable range for $\Delta E_{cell} > 0.20$ V. This behavior can be attributed to the relatively higher increase in ε_{pl}^{*} with the increase in cathode pressure for higher ΔE_{cell}. Figure 11(b) shows the design window for cathode stoichiometry. Similar to the observation for cathode pressure the upper limit and lower limits for $\Delta E_{cell} \leq 0.15$ V is marked by the limiting value of range of cathode stoichiometry used in the study. It is also noted that the lower limit for cathode stoichiometry increases with the increase in load change. This can be attributed to the high plastic strain values at lower stoichiometric flow ratios, which decreases with the increase in cathode stoichiometry, as seen from Fig. 8. Figure 11(c) shows the design window for relative humidity at cathode inlet. It can be seen that for $\Delta E_{cell} \leq 0.20$ V the lower limit is 0%, while there exists no operable region for $\Delta E_{cell} > 0.20$ V.

The results presented above offer insight into the effects of various operating conditions on the mechanical behavior of the membrane for specified load cycles. Future work could include a study of various existing membranes, such as reinforced membranes, hydrocarbon membranes and others, using the present model. The time dependency of plastic strain, along with the anisotropy in material properties can be added to the present model to predict a more realistic behavior. A coupled model, although computationally expensive, can be incorporated to capture the mechanical effects on water transport and vice-versa. A better design of membranes based on the water content in membrane, by optimization of membrane physical and transport properties can be performed, so as to minimize the degradation.

6.4 Nomenclature

A	superficial electrode area [m^2]
C_k	molar concentration of species k [mol/m^3]
D	mass diffusivity of species [m^2/s]
E_{cell}	cell potential or voltage [V]
EW	equivalent weight of dry membrane [kg/mol]
F	Faraday constant [96,487 C/equivalent]
j	transfer current [A/m^3]
K	permeability [m^2]
n_d	electro-osmotic drag coefficient [H_2O/H^+]
p	pressure [bar]
R	gas constant [8.314 J/mol K]
RH	relative humidity
S	source term in transport equations
T	temperature [K]
$\vec{u}$	velocity vector
v	displacement

Greek letters

α	transfer coefficient
ε	porosity; strain
η	surface overpotential [V]
λ	membrane water content; proportionality scalar
μ	viscosity [kg/m s]
ρ	density [kg/m^3]

σ	electronic conductivity [S/m]; stress
τ	shear stress [N/m²]; time constant; tortuosity
ϕ	phase potential [V]

Superscripts and subscripts

a	anode
c	cathode
$cell$	single fuel cell
e	electrolyte
el	elastic
eff	effective value
eq	equivalent
g	gas phase
in	inlet
k	species
m	membrane phase
max	maximum
0	t = 0 s, initial state
pl	plastic
ref	reference value
s	electronic phase
S	swelling
sat	saturated value
SS	steady state

t time > 0 s

w water

References

[1] N.L. Garland, J.P. Kopasz, Journal of Power Sources 172(1) (2007) 94-99.

[2] D.O. Energy (Ed.), Basic Research Needs for the Hydrogen Economy, report of basic energy science workshop on hydrogen production, storage and use prepared by Argonne National Laboratories, Rockville, Maryland (2003) 53-60.

[3] C.Y. Wang, Chemical Reviews. 104 (2004) 4727-4766.

[4] M.L. Perry, T.F. Fuller, J. Electrochemical So. 149 (7) (2002) S59-67.

[5] R. Borup, J. Meyers, B. Pivovar, Y.S. Kim, R. Mukundan, N. Garland, N. Iwashita, et al. 107(10) (2007) 3904-3951.

[6] V. Stanic, M. Hoberecht, 4th International Symposium on Proton Conducting Membrane Fuel Cells 2004, October.

[7] W. Liu, K. Ruth, G. Rusch, J. New Mater. Electrochem. Syst.; 4 (2001) 227-231.

[8] P. Gode, J. Ihonen, A. Strandroth, H. Ericson, G. Lindbergh, M. Paronen, F. Sundholm, G. Sundholm, N. Walsby, Fuel Cells 3(1-2) (2003) 21-27.

[9] Y. Lai, C.K. Mittelsteadt, C.S. Gittleman, D.A. Dillard, Proceedings of the Third International Conference on Fuel Cell Science, Engineering and Technology (2005) May 23–25; Ypsilanti, Michigan:161–167.

[10] A. Webber, J. Newman, Fuel Cell, AIChE J. 50(12) (2004) 3215–3226.

[11] Y. Tang, M.H. Santare, A.M. Karlsson, S. Cleghorn, W.B. Johnson, J. Fuel Cell Sci. Technol 3 (2006) 119–124.

[12] A. Kusoglu, A.M. Karlsson, M.H. Santare, S. Cleghorn, W.B. Johnson, Journal of Power Sources, 161 (2006) 987-996

[13] Kusoglu, A.M. Karlsson, M.H. Santare, S. Cleghorn, W.B. Johnson, Journal of Power Sources; 170 (2007)345-358

[14] Kusoglu, M.H. Santare, A.M. Karlsson, S. Cleghorn, W.B. Johnson, J. Electrochemical So. 2010; **157** (5): B705-13.

[15] J. Kleemann, F. Finsterwalder, W. Tillmetz, Journal of Power Sources 190(1) (2009) 92-102.

[16] Y. Zhou, G. Lin, J. Shih, S.J. Hu, Journal of Power Sources 192 (2009) 544-551.

[17] M.F. Serincan, U. Passaogullari, Journal of Power Sources 196 (2011) 1314-1320.

[18] Taymaz, M. Benli, Energy 35 (2010) 2134-2140

[19] X. Wang, X. Huang, L. Bonville, H.R. Kunz, M.L. Perry, D. Condit, J. Electrochemical So. 161(6) (2014) F761-F769

[20] A. Verma, R. Pitchumani, J. Fuel Cell Sci. Technol 11(3) (2014) 031009, 9pp., doi: 10.1115/1.4026551

[21] Y. Wang, C.Y. Wang, Electrochem. Acta 50 (2005) 1307-1315

[22] A. Verma, R. Pitchumani, Journal of Power Sources 268 (2014) 733-743

[23] P. Commer, A.G. Cherstvy, E. Spohr, A.A. Kornyshev, Fuel Cells 2 (2002) 127–136.

[24] A. Verma, R. Pitchumani, Int. J. of Hydrogen Energy 39 (2014) I9024-I9038

[25] A. Verma, R. Pitchumani, J. Fuel Cell Sci. Technol. 2014; (Accepted, In Production)

[26] Ansys ® Academic Research, Release 14.0

Table 6.1: Source terms in the governing equations

Domain	S_v	S_i	S_s , S_m
Gas channels	0	0	0
Diffusion layers	$-\frac{\mu}{K_{GDL}}\vec{u}$	0	0
Catalyst layers	$-\frac{\mu}{K_{GDL}}\vec{u}$	anode: $-\frac{j_a}{2F}(i=H_2)$ [1] $(i=O_2)$ $-\nabla.\left(\frac{n_d i_e}{F}\right)$ $(i=H_2O)$	anode: $S_s=-j_a<0$ $S_m=+j_a<0$
		cathode: 0 $(i=H_2)$ $-\frac{j_c}{4F}(i=O_2)$ $\frac{j_c}{2F}-\nabla.\left(\frac{n_d i_e}{F}\right)(i=H_2O)$	cathode: $S_s=+j_c>0$ $S_m=-j_c<0$
Membrane	$-\frac{\mu}{K_{GDL}}\vec{u}$	0	0

Table 6.2: Geometrical and physical parameters used in the numerical simulations [13,14]

Parameter [units]	Symbol	Value
Gas channel depth [mm]		1.0
Diffusion layer thickness [mm]		0.3
Catalyst layer thickness [mm]		0.01
Membrane (N112) thickness [mm]		0.051
Fuel cell/Gas channel length [mm]		100.0
Temperature [K]	T	353
Permeability of diffusion layer [m^2]	K_{GDL}	10^{-12}
Permeability of catalyst layer [m^2]	K_{CL}	10^{-15}
Gas diffusion layer porosity	ε_{GDL}	0.6
Catalyst layer porosity	ε_{CL}	0.4
Volume fraction membrane in catalyst layer	ε_m	0.26
Anode reference exchange current density [A/m^3]	$j_{a,ref}$	5.00×10^8
Cathode reference exchange current density [A/m^3]	$j_{c,ref}$	500
H_2 diffusivity membrane [m^2/s]	$D_{H_2,mem}$	2.59×10^{-10}
H_2 diffusivity in gas [m^2/s]	$D_{H_2,ref}$	1.1×10^{-4}
O_2 diffusivity in membrane [m^2/s]	$D_{O_2,mem}$	8.328×10^{-10}
O_2 diffusivity in gas [m^2/s]	$D_{O_2,ref}$	3.2348×10^{-5}
H_2O diffusivity in gas [m^2/s]	$D_{H_2O,ref}$	7.35×10^{-5}

Table 6.3: Physical properties of materials used in the finite element analysis [10,11]

Material	ρ [kg/m^3]	E [MPa]	υ
Bipolar plates	1800	10,000	0.25
GDE (Carbon Paper)	400	10,000	0.25
Membrane (Nafion® 112)	200	*Table 4*	0.25

Table 6.4: Physical properties of the membrane (Nafion® 112) used in the analysis [10,11]

RH [%]	Young's Modulus [MPa]	Yield Stress [MPa]	$\beta\left[\frac{m}{m\%RH}\right] \times 10^{-6}$
30	121	4.20	1456
50	85	3.32	1197
70	59	2.97	2128
90	46	2.29	3670

Table 6.5: Initial conditions used in the finite element analysis

Zero-stress Condition	*RH in membrane <= 30%*
Step 1: Mechanical Loading	Clamping Pressure is applied (p = 1 MPa)
Step 2: Pre-stressed + Hygral Loading	RH loading corresponding to E_{cell} = 0.8 V on membrane

Chapter 7: Dynamic fractal model for porous media undergoing deposition

A dynamic fractal model is developed to predict the evolution in pore structure undergoing deposition. An artificial saturation in pores is created using dilation of solid boundaries in the pore structure image. Fractal dimensions of the image are analyzed using box counting method for changes in saturation levels and compared with predictions from the dynamic model. The changes in transport characteristics of the porous media are evaluated and compared against other existing models.

7.1 Introduction

Modification in structure of porous media can be commonly observed as a part of several physical processes such as chemical vapor deposition, transport in fuel cell layers and batteries, fouling in membranes, percolation through rock structures etc. Thus characterizing the changes in pore structure is important for successfully predicting the transport in these applications and forms the focus of current study.

Several experimental studies over past decades has focused on measurement of transport properties in porous media by quantifying pressure drop, species concentration and flow. A more recent literature has seen increase in the numerical work involving reconstruction of porous media combined with Lattice Boltzmann modeling to predict transport properties [1-7].

Owing to the disordered nature of pore structures it can be well described by fractal dimensions, that in turn is used to predict transport properties such as permeability, conductivity and diffusivity. Analysis of pore structure image using box counting method is one of the commonly used techniques to evaluate fractal dimensions and has been actively employed by several researchers to predict transport properties for a variety of microstructures such as sandstones, fibers, etc. [8-12]. Although the properties of porous media have been explored extensively, the study of changes in pore structure and thus the corresponding properties owing to deposition or erosion remains a relatively unexplored area. Previous theoretical and experimental studies have largely focused on determining the fractal dimensions for pore structures at the beginning of deposition or erosion, followed by use of analytical models or experimental correlations to describe changes in transport properties with

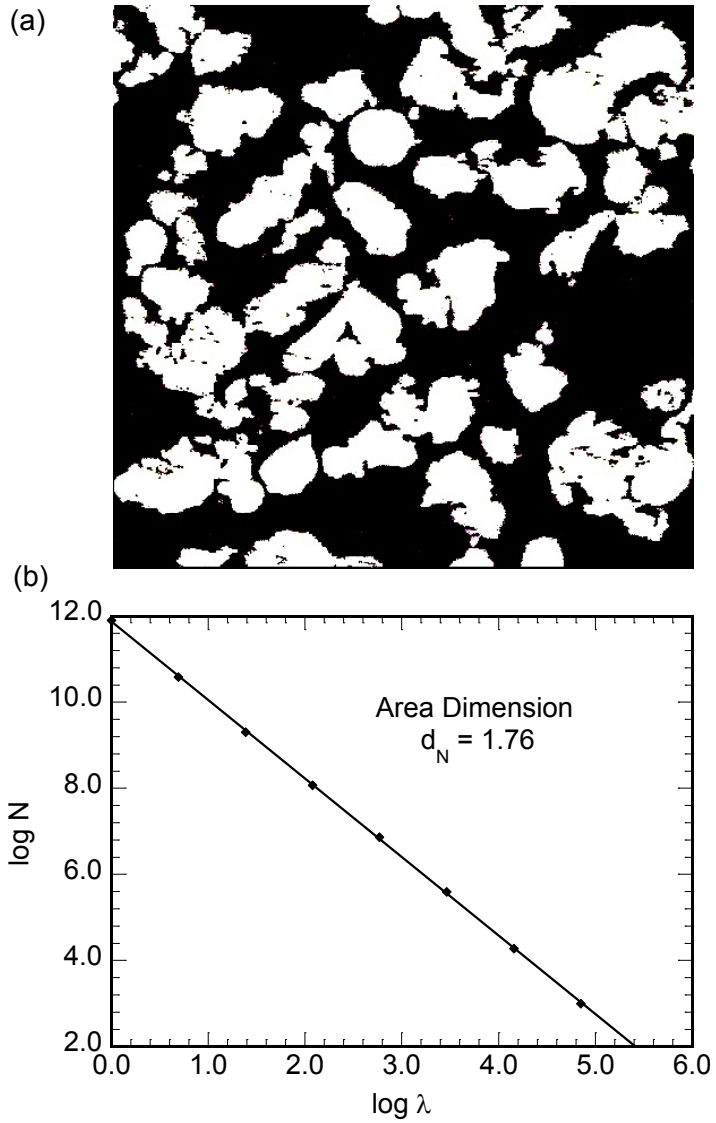

Figure 7.1 : (a) Pore structure image (Yu and Cheng [11]) and (b) the cumulative pore count as a function of pore size.

deposition. The studies relating to permeability reduction, few in number, have used pore scale analysis of structures, constructed through x-ray micro chromatography (XMCT), serial sectioning or laser scanning confocal microscopy, using either pore network model or Lattice Boltzmann (LB) model. Chen et al.[6] used x-ray micro chromatography to construct three-dimensional (3D) geometry of the pore structure before and after colloid deposition, followed by LB simulations to evaluate change in local permeability and tortuosity. It was found that the change in permeability followed a power law variation with respect to porosity and the results

significantly differed from the predictions using Kozeny-Carman relationship. Similar studies involving XMCT and LB modeling was performed by Okabe et al.[7].

In this letter, we address the challenge of predicting the evolution of pore structure as a function of deposition or saturation using fractal model. A model to predict the changes in fractal dimensions for a pore structure undergoing deposition is developed and compared with the predictions obtained from image analysis (box counting method). The variation in effective diffusivity is predicted with the dynamic fractal model and compared with other analytical solutions.

7.2 Fractal Model

In a fractal representation the pore architecture is usually quantified in terms of fractal dimensions d_T and d_N, corresponding to the tortuosity and area dimensions, respectively. The porous medium can be envisioned to be a distribution of capillaries of several sizes. The effective length, L_c, of a capillary of size λ can be given by [8-12]:

$$L_c(\lambda) = \lambda^{1-d_T} L_0^{d_T} \text{ []} \tag{1}$$

where L_0 is the representative length. Thus $d_T = 1$ would correspond to a straight capillary and $d_T = 2$ would correspond to a highly tortuous media. The cumulative pore distribution, as seen in representation of geomorphology of earth $N\ (A > a) \sim a^{-D/2}$ [13], can be represented by [8-12]:

$$N(L \geq \lambda) = \left(\frac{\lambda_{max}}{\lambda}\right)^{d_N} \tag{2}$$

The theory of fractal dimensions and representation of porous media using these dimensions is well established and is not discussed in detail here. Readers are advised to refer to Refs. [8-12] for a more detailed explanation.

Figure 1 shows the image of a porous media, studied by Yu and Cheng [11] (Fig. 1(a)) and the corresponding cumulative pore count as a function of pore size (Fig. 1(b)). The black and white regions represent the pore and solid regions, respectively, with the solid regions formed by the agglomeration of copper particles [11]. The log-log plot of the cumulative distribution of pores (Fig. 1(b)) obtained through box-counting method indicate fractal nature to the pore distribution with the area fractal dimension d_N = 1.76. The value calculated by Yu and Cheng

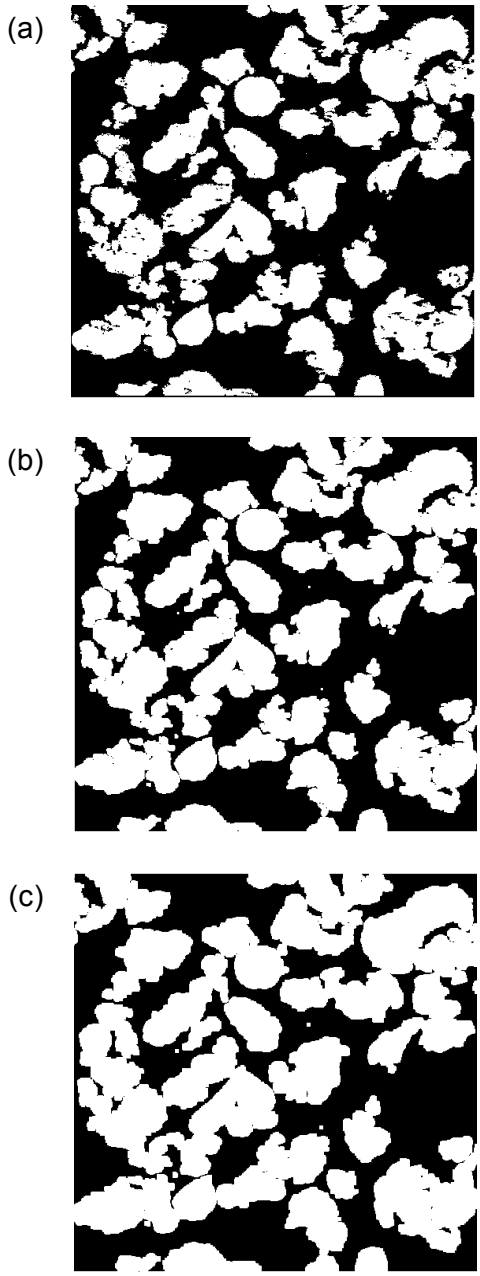

Figure 7.2 : Pore structure images for saturation (a) s = 0, (b) s = 0.116 and (c) s = 0.208.

[11] for the above geometry was 1.79 considering a bi-dispersed porous media, which is very close to the value obtained here, while treating the media as mono-dispersed.

7.3 Saturation/ Deposition in Porous media:

An artificial deposition/ saturation is generated in porous media by dilation of the solid boundaries in the pore structure image using Image Processing Toolbox™ [14] to mimic the physical deposition in pores. Figure 2 shows the pore structure images with different saturation values, where saturation is defined as $s = 1 - \varepsilon^{new}/\varepsilon^0$, with ε^0 and ε^{new} as the porosity of the medium before and after deposition, respectively. The porosity and saturation values for Fig. 2(a), (b), (c) are s = 0, 0.116, 0.208 and ε = 0.575, 0.508, 0.456, respectively.

Evaluating changes in d_N

According to Yu and Cheng [11] the area fractal dimension, d_N, can be given by:

$$d_N = k - \frac{ln\varepsilon}{ln\frac{\lambda_{min}}{\lambda_{max}}} \tag{3}$$

where k = 2 (two dimensions) and 3(3 dimensions) , λ_{min} and λ_{max} are the minimum and maximum size of the pores, respectively. Thus for the present case,

$$d_N = 2 - \frac{ln\varepsilon}{ln\frac{\lambda_{min}}{\lambda_{max}}}. \tag{4}$$

Thus for change in porosity from ε^0 to $\varepsilon(s) = \varepsilon^0(1-s)$,

$$\frac{ln\varepsilon^0}{ln\varepsilon(s)} = \frac{ln\varepsilon^0}{ln\varepsilon^0(1-s)} = \frac{2-d_N}{2-d_N^{'}} \tag{5}$$

where $d_N^{'}$ is the area fractal dimension of the pore structure at saturation, s. Thus $d_N^{'} < d_N$ for increase in saturation, s. Pitchumani and Ramakrishnan [9] used area fraction to establish relationship between geometric and fractal dimensions. For area fraction being a representative of volume fraction it was derived that,

$$d_N = 2(1-\beta^2),\ \beta = \lambda_{max}/L_0 \tag{6}$$

implying that $d_N^{'} > d_N$ for increase in saturation.

Figure 3(a) presents the variation in d_N as calculated from the box counting method and that obtained from Eq. (4). It can be seen that d_N decreases with increase in saturation, with Eq.(4) predicting a similar trend to that described by image analysis. It is noted that the predictions from Eq.(4) show a larger deviation from the results obtained by box counting method (image analysis) with increase in saturation. This can attributed to the fact that a simple Sierpinski triangle model [11] was used to derive the relationship in Eq.(3) whereas in reality a different power law variation could exist. It is also noted that the predictions from Eq. (6), $d_N^{'} > d_N$, completely diverge from that obtained from Fig. 3(a) and is rejected as a prospective model for

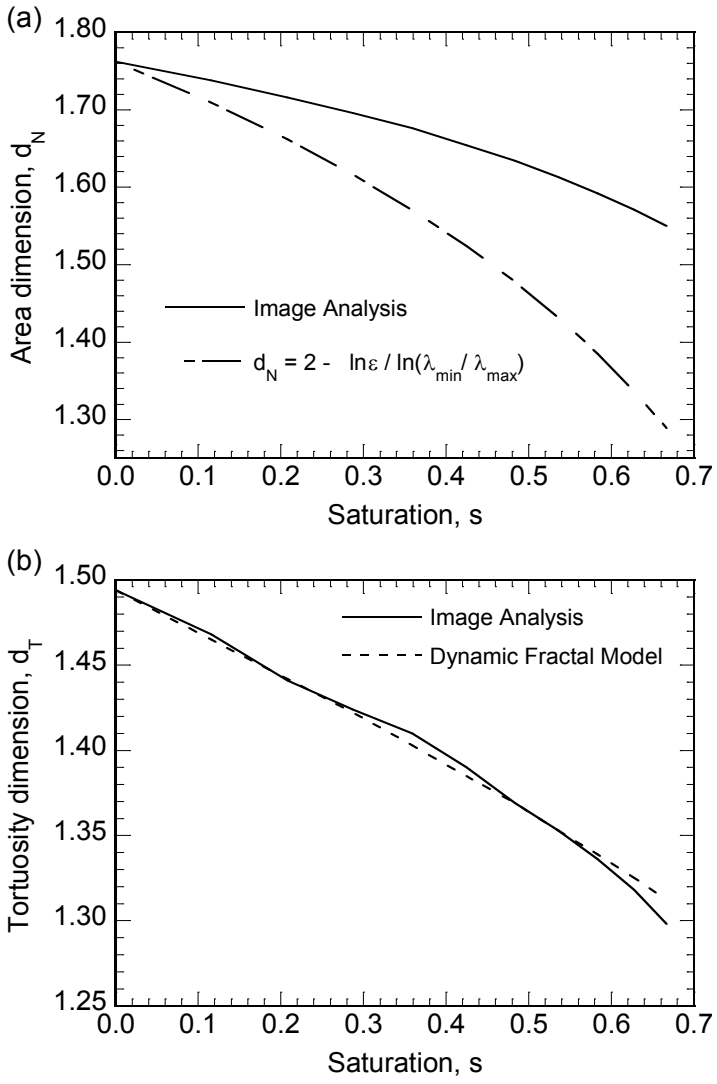

Figure 7.3: Variation in (a) area dimension, d_N and (b) tortuosity dimension, d_T, as a function of saturation.

further discussions. In the absence of better comprehensive theoretical model to accurately describe the changes in $d_N^{'}$ as seen in Fig. 3(a), Eq. (4) is assumed to represent the evolution of area fractal dimension for accurately for smaller values of saturation.

Evaluating changes in d_T

For small values of deposition it can be envisioned that there is no change in the effective length of the pores, thus from Eq. (1):

$$\frac{L_c(\lambda)}{L_0} = \left(\frac{L_0}{\lambda_0\sqrt{(1-s)}}\right)^{d_T^{'}-1} = \left(\frac{L_0}{\lambda_0}\right)^{d_T-1} \tag{7}$$

where $d_T^{'}$ and $\lambda_0\sqrt{(1-s)}$ are the area dimension and pore size at saturation, s. Hence $d_T^{'}$ can be written as:

$$d_T^{'} = d_T^{'}(s,\lambda) = 1 + (d_T - 1)\frac{\ln\left(\frac{L_0}{\lambda_0}\right)}{\ln\left(\frac{L_0}{\lambda_0\sqrt{(1-s)}}\right)} \tag{8}$$

The cumulative length of the pores, L^{eff}, is given by:

$$L^{eff} = \int_{\lambda_{min}}^{\lambda_{max}} L_c(\lambda)dN(\lambda) = \left(\frac{1}{\beta}\right)^{d_T} \lambda_{max} d_N \frac{(1-\alpha^{1-d_T-d_N})}{(1-d_T-d_N)} \tag{9}$$

where $\alpha = {\lambda_{min}}/{\lambda_{max}}$. For very small α

$$L^{eff} = \left(\frac{1}{\beta}\right)^{d_T} \lambda_{max} \frac{d_N}{(1-d_T-d_N)} \tag{10}$$

Similarly the effective length at any given saturation, s, can be given by:

$$L^{eff}(s) = \left(\frac{1}{\beta(s)}\right)^{d_T^{'}} \lambda_{max} \frac{d_N^{'}}{(1-d_T^{'}-d_N^{'})} \tag{11}$$

For small values of saturation it can be safely assumed that $L^{eff} = L^{eff}(s)$. From Eqs. (10) and (11) it can be deduced that:

$$\left(\frac{1}{\beta}\right)^{d_T - d_T^{'}} = \left(\sqrt{(1-s)}\right)^{1-d_T^{'}} \frac{(1-d_T-d_N)}{(1-d_T^{'}-d_N^{'})} \frac{d_N^{'}}{d_N} \tag{12}$$

Thus from Eq. (12) it can be inferred that $d_T^{'}(\beta, d_N, s) < d_T$ for $s > 0$.

Figure 3(b) shows the variation in tortuous fractal dimension d_T as a function of saturation. The results from image analysis (box counting method) are represented by solid line. It can be seen that d_T reduces with the increase in saturation, with the results from the dynamic model closely predicting the changes as observed by image analysis. The reduction in d_T can be seen as an averaging effect where the pores with smaller diameter become less relevant to describing the pore structure with increase in saturation, resulting in increase in average pore size and thus smaller values of d_T. It is to be noted here that above relationship is derived for smaller values of saturation and might not hold true for larger saturations where there is significant restructuring of transport path. A more accurate representation will be a distribution of d_T over different ranges of saturations.

7.4. Evaluating changes in effective diffusivity

Flow rate, Q, through the porous media for diffusion can be given by [9-12]:

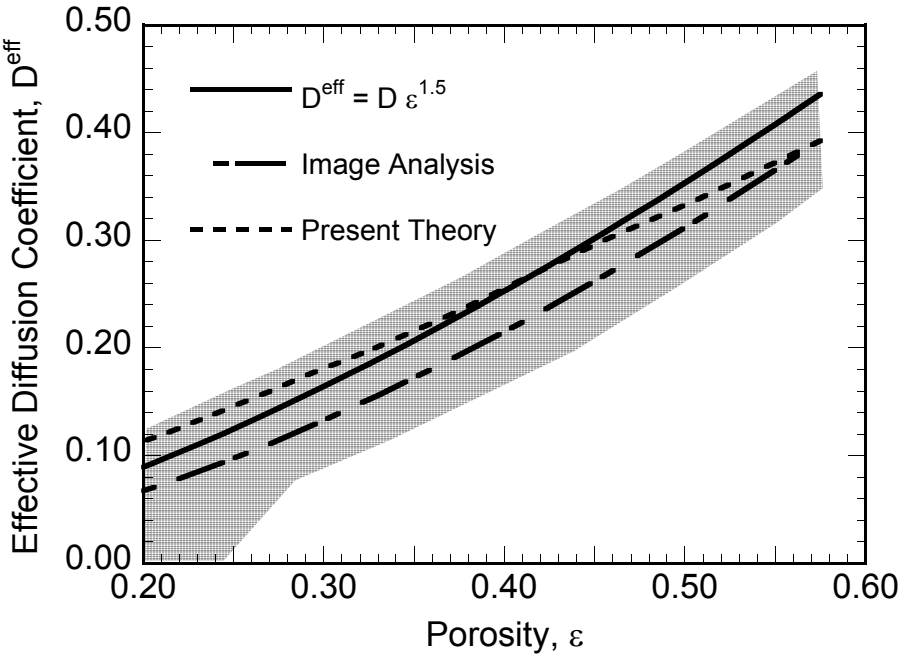

Figure 7.4: Variation of effective diffusivity, D^{eff}, with saturation.

$$Q = A_0 D^{eff} \frac{\Delta C}{L_0} = \int_{\lambda_{min}}^{\lambda_{max}} q(\lambda) dN(\lambda) = g_q \, D \, \Delta C \, \beta^{d_T} \, \lambda_{max} \, d_N \, \frac{(1-\alpha^{1+d_T-d_N})}{(1+d_T-d_N)} \tag{13}$$

where D^{eff} is the effective diffusion coefficient, A_0 is the representative area and $q(\lambda)$ is the flow rate through a single capillary of size λ [8-12]. Hence the effective diffusion coefficient as a function of fractal dimensions d_N and d_T is be given by:

$$D^{eff} = g_q \, D \, \beta^{d_T+1} \, d_N \, \frac{(1-\alpha^{1+d_T-d_N})}{(1+d_T-d_N)} \tag{14}$$

where $g_q = \pi/4$. There are numerous models that describe change in diffusivity as a function of porosity, $D^{eff} = D/N_M$, where N_M is the MacMullin number as given in Table 1 [15,16]. A more commonly used relationship to describe changes in D^{eff} as a function of porosity is $D^{eff} = \varepsilon^{1.5} D$. Thus change in D^{eff} with change in saturation can be described as:

$$D^{eff} = (\varepsilon(1-s))^{1.5} D. \tag{15}$$

The change in effective diffusivity as a function of saturation (change in porosity) is presented in Fig. 4. The shaded area represents region between upper and lower bounds formed by the values of D^{eff} as calculated using MacMullin number from Table 1. It is noted from Fig. 4 that the trends described by dynamic fractal model (Eq. (13)) and $D^{eff} = \varepsilon^{1.5}$ (Eq. (14)) are similar and show a decrease in D^{eff} with increase in saturation or decrease in porosity. It can also be seen that the predictions by the fractal model, using the values obtained through

image analysis and that by dynamic model, lie in the bounds suggesting that the pore structure can be described as combination of different geometries, arrangements and sizes of pores.

The present model although limited to uniform saturation works well for cases where there are no changes to flow path as hypothesized. Changes to above, for a more comprehensive model, can be accommodated by relating the deposition, pore size distribution and networking such that d_T has different variations for range of saturation values. A pore network model for random 3D geometry coupled with image analysis can provide better insight to the above problem and can be studied as a part of future work. Also, the effects of multiphase flow can be characterized using the above formulation.

References

[1] C. Manwart, U. Aaltosalmi, A. Koponen, R. Hilfer and J. Timonen. *Physical Review E* 66, no. 1 (2002): 016702.

[2] L. Chen, , L. Zhang, Q. Kang, H.S. Viswanathan, J. Yao and W. Tao. *Scientific reports* 5 (2015).

[3] T. Gebäck, M. Marucci, Catherine Boissier, Johan Arnehed and Alexei Heintz. *The Journal of Physical Chemistry B* 119, no. 16 (2015): 5220-5227.

[4] H Koku, R.S. Maier, K.J. Czymmek, M.R. Schure and A.M. Lenhoff. *Journal of Chromatography A* 1218, no. 22 (2011): 3466-3475.

[5] L. Chen, G. Wu, E.F. Holby, P. Zelenay, W.Q. Tao and Q. Kang. *Electrochimica Acta* 158 (2015): 175-186.

[6] C. Chen, A.I. Packman, and J.F. Gaillard. *Geophysical Research Letters* 35, no. 7 (2008).

[7] H. Okabe and Martin J. Blunt. *Physical Review E* 70, no. 6 (2004): 066135.

[8] D. A. Weitz and M. Oliveria. *Physical Review Letters* 52, no. 16 (1984): 1433.

[9] R. Pitchumani and B. Ramakrishnan. *International Journal of Heat and Mass Transfer* 42, no. 12 (1999): 2219-2232.

[10] B. Yu and J. Li. *Fractals* 9, no. 03 (2001): 365-372.

[11] B. Yu and P. Cheng. *International Journal of Heat and Mass Transfer* 45, no. 14 (2002): 2983-2993.

[12] B. Yu and W. Liu. *AIChE journal* 50, no. 1 (2004): 46-57.

[13] B.B. Mandelbrot. *The fractal geometry of nature*. Vol. 173. Macmillan, 1983.

[14] Image Processing Toolbox™, The Math Works Inc., 2015, http://www.mathworks.com/help/images/

[15] M.J. Martínez, S. Shimpalee and J.W. Van Zee. *Journal of The Electrochemical Society* 156, no. 1 (2009): B80-B85.

[16] Y. Wang, S.C. Cho, and Ken S. Chen. *PEM fuel cells*. Momentum Press, 2013.

Table 7.1: MacMullin number as a function of porosity for various geometries, arrangement and size [15,16].

Label	Expression
I	$N_M = \frac{(5-\varepsilon)(3+\varepsilon)}{8(1+\varepsilon)\varepsilon}$
II	$N_M = \frac{(3-\varepsilon)\left[\frac{4}{3}+0.409(1-\varepsilon)^{\frac{7}{3}}\right]-1.315(1-\varepsilon)^{\frac{10}{3}}}{2\varepsilon\left[\frac{4}{3}+0.409(1-\varepsilon)^{\frac{7}{3}}\right]-1.315(1-\varepsilon)^{\frac{10}{3}}}$
III	$N_M = \frac{2-\varepsilon-0.3058(1-\varepsilon)^4-1.334(1-\varepsilon)^8}{\varepsilon-0.3058(1-\varepsilon)^4-1.334(1-\varepsilon)^8}$
IV	$N_M = \frac{2-\varepsilon-0.3058(1-\varepsilon)^4-1.334(1-\varepsilon)^8}{\varepsilon-0.3058(1-\varepsilon)^4-1.334(1-\varepsilon)^8}$

Chapter 8: Conclusion and Future Work

The present studies analyzed the transients of a single channel fuel cell to describe the performance and mechanical behavior of fuel cells using numerical models.

In the first part, a comprehensive analysis of the effects of operating parameters on the variation of steady state time for step change in cell potential was presented, based on numerical simulations using two-dimensional physics-based model. It was shown that water transport dynamics is critical to the transient behavior of PEM fuel cells. The variation of steady state time (t_{SS}) was found to be monotonic, as a function of anode and cathode stoichiometric flow ratio, and cathode pressure, whereas it was non monotonic, as a function of anode pressure, anode and cathode relative humidity. Larger membrane water content difference increases steady state time, as it takes more time for the membrane to dehydrate or uptake water. Design windows for the operating parameters—pressure, stoichiometric flow ratio, and relative humidity at anode and cathode side—were constructed which limits t_{SS} to less than an illustrative value of 10 s. Optimum operating conditions as a function of cell voltage change were determined so as to minimize the time required to reach steady state. The above analysis provides an insight on way the fuel cell can be operated for rapid load changes.

Next, a comprehensive analysis of the effects of cyclic changes in operating parameters on the power response of a single-channel PEM fuel cell was presented, based on the numerical simulations. It was shown that operating parameters affect the power response differently over the cycles. The power response was shown to depend not only on the amplitude but also the time period of the variations and is strongly correlated to the time scale of species and water transport mechanisms. Optimization studies show limits and that the rate at which cell voltage needs to change to meet the desired power requirements and the corresponding maximum pressure and flow rates required. The results provide insight into controlling operating parameters and designing better control systems to improve fuel cell performance for transient applications with rapid load changes.

In the second part, a comprehensive analysis of the effects of membrane properties on the cell voltage response of a single-channel PEM fuel cell was presented, based on the numerical simulations for low humidity operations. It was shown that a sudden increase in current density can lead to anode dryout, causing voltage reversal and may lead to cell

degradation. The voltage response was shown to be a strongly correlated to the membrane properties and also the water diffusion in porous media. It was also shown that the voltage reversals can be averted by employing graded membrane approach. The results provide insight in designing and choosing membranes for particular applications.

Mechanical Behavior

A systematic numerical investigation of the effects of load cycling and inlet humidification values on the mechanical behavior of membrane in a single channel PEM fuel cell was carried out. The results presented in study illustrate the inlet relative humidity and the load change significantly affect the mechanical behavior of membrane along the length of the fuel cell. It was seen that the residual stresses generated as a result of unloading can further lead to plastic deformation, thus assisting in membrane degradation. The amount of plastic strain and the volume of the membrane that undergoes plastic deformation are minimized for dry inlet conditions, $RH_c^{in} = 0\%$. For the higher loads, the maximum strain occurs at the cathode side of the membrane, both at the inlet and the outlet regions, whereas for lower loads anode side of the membrane also undergoes plastic deformation at the near inlet regions. The results presented in this work offer insight into the effects of complex water distribution on the localization of stress and plastic strain in the membrane. The detailed numerical investigation suggests that plastic deformation in membrane is dependent on the load changes, inlet relative humidity and length of the section from inlet. During unloading, residual tensile stresses may develop and lead to tensile yielding of the membrane, thus contributing to the degradation of the membrane and in some cases even failure.

In the next part, the effects of operating conditions and load change on the mechanical response of membrane in a single-channel PEM fuel cell was presented, based on the numerical simulations over the range of operating conditions. It was shown that the magnitude of plastic strain and volume of membrane that deforms plastically are strongly correlated to the amount of load change and operating conditions and, in turn, affects membrane degradation. The deformation pattern varies along the length of the fuel cell, owing to the complex water distribution in the membrane. It was found that increase in cathode pressure and inlet humidity leads to significant increase in plastic strain whereas increase in cathode stoichiometry minimizes the strain. For certain cases the amount of plastic strain was governed by the strain induced at base loads and was found to be independent of load changes. Unloading of the

membrane can lead to residual stresses causing further plastic deformation. The work correlates operating conditions and mechanical response of the membrane, thus providing insight in to the design of membranes and optimization of operating conditions to minimize degradation for desired applications.

Finally, the dynamic fractal model correlating the fractal dimensions and saturation was presented. It was shown that the predictions from model are close to the values obtained through image analysis for small values of saturation. The dynamic fractal model was later used to predict the changes in diffusion coefficient as a function of saturation.

Future Work

1) Development of detailed Two phase model combined with Visco-Elastic mechanical description (high humidity operation): A 2-phase model combined with visco-elastic description of membrane can be explored in future to capture a more realistic behavior of fuel cells for optimization at high humidity operations. Also, FEM model to couple the performance and mechanical response will offer a deeper insight in to the transient behavior.

2) Development of detailed model for Li-Air batteries: The hybrid structure is seen to be promising technologies as power source for stationary and transport applications. Li-Air batteries presents itself as an viable option due high discharge rates compared to other batteries. A detailed modeling is needed so as to evaluate the degree of hybridization for hybrid purposes. Models to evaluate the best hybridization for fuel cell technologies for stationary and transport applications are needed. These models based on detailed physics will help determine the best operating parameters such as to achieve higher efficiency and better hybrid options.

3) Comprehensive Fractal Model: A comprehensive fractal model is needed to accurately capture the changes in porous structure for different regimes of deposition. At present a uniform deposition and no changes in the effective length are assumed. A more detailed description can be obtained by correlating the pore size, fractal dimensions and deposition using direct numerical simulations on different porous structure for different levels of saturation.